Effect of Seed Composition and Growth Pressure on Au-Assisted TiO_2 Nanowire Growth

by

Zhina Razaghi

A thesis submitted to the faculty of graduate and postdoctoral studies
in partial fulfillment of the requirements of the degree of

DOCTOR OF PHILOSOPHY

Department of Mechanical Engineering
University of Manitoba
Winnipeg, MB, Canada

Abstract

This thesis investigates the vapor–adsorbate–solid (VAdS) growth of TiO_2 nanowires and demonstrates how pressure and seed composition govern nanowire formation and morphology. Unlike previously reported open-flow systems, the closed, no-flow geometry used here enabled growth across a broad sealing pressure range, from near atmospheric pressure down to 0.4 Pa. The most favorable growth was observed between 10 and 1000 Pa, likely due to an optimal oxygen partial pressure that promotes TiO_2 substrate evaporation. Beyond pressure, seed composition emerged as a key parameter for tailoring nanowire morphology. In our previous work, pure Au seeds produced bead-like nanowires oriented along $[110]_{TiO_2}$, while incorporating Ag into the Au seed led to the formation of Ag-rich segregation domains, shifting the morphology toward prismatic $<111>_{TiO_2}$ nanowires and underscoring the influence of seed chemistry. Building on this finding, the present study further explores the effect of seed composition by examining the incorporation of Ni and Ag into Au seeds. In Au–Ni seeds, the addition of Ni promoted endotaxial embedding of Au nanoparticles, altering the Au–TiO_2 interface and producing new orientation relationships. These embedded nanoparticles exhibited irregular shapes in bead-like [110]-oriented nanowires, while well-faceted nanoparticles bounded by low-index planes formed in prismatic <111>-oriented nanowires, underscoring the role of crystallographic factors in addition to growth oscillations. In Au–Ag seeds, local compositional heterogeneity was shown to dictate nanowire morphology, as Ag-rich regions at the junction of $\{10\bar{1}\}$ and $\{1\bar{1}0\}_{TiO_2}$ facets promoted site-specific nucleation and enabled the transition from bead-like $<110>_{TiO_2}$ nanowires to prismatic $<111>_{TiO_2}$ nanowires. Spectroscopic analyses revealed evidence of Ag–O interactions, confirming

Ag’s stronger affinity for oxygen and its role in stabilizing prismatic growth fronts. Overall, this work establishes a framework for tailoring oxide nanowires through controlled VAdS growth and seed-induced interfacial engineering, offering pathways for the rational design of nanostructures with applications in electronics, photonics, and catalysis.

Acknowledgments

I would like to sincerely thank my supervisor, Dr. Guo-zhen Zhu, for her invaluable guidance, support, and encouragement throughout my Ph.D. journey. Her mentorship and insightful feedback have greatly shaped both my research and professional growth. I am grateful to my thesis advisory committee members, Dr. Olanrewaju Ojo and Dr. Carl Ho, for their constructive suggestions and continuous support, and to Dr. Ning Chen, senior scientist at the Canadian Light Source for his assistance with X-ray absorption spectroscopy. I would like to acknowledge the staff of the Manitoba Institute for Materials—Dr. Abdul Khan, Dr. Ravinder Sidhu, and Jolly Hipolito—for their technical assistance, and Ryan Sharp, lab manager of the Earth Materials and Archaeometry Centre, for his help with Au sputtering. I am also grateful to Paul Krueger and Mike Boskwick, Mechanical Engineering technologists, for their support in setting up the tube sealing machine. Special thanks go to Moein Imani Foumani for his support and contributions in building a positive lab environment, as well as his efforts in establishing the Microscopy Society of Canada Student Chapter in Manitoba. I am also thankful to my other current and former colleagues for their help with experiments, discussions, and collaboration. I extend my heartfelt gratitude to my family and friends—especially my parents and my brothers, Sina and Kia—for their unconditional love, patience, and encouragement. Their constant support has been the foundation of all my achievements. I am also thankful to my partner, Ali, whose support carried me through moments of doubt and motivated me to keep going.

Table of Contents

List of Publications

Peer-Reviewed Papers:

1. Z. Razaghi, M. Lin, N. Chen, K. Cui, and G. Zhu, "Spectroscopic Insights into Controlling Sidewall Faceting of TiO_2 Nanowires via Au-Ag Bimetallic Seeds," Langmuir, Oct. 2025, DOI: 10.1021/acs.langmuir.5c03334.
2. Z. Razaghi and G. Zhu, "Ni-Assisted Endotaxial Growth of Au Nanoparticles Within TiO_2 Nanowires," Adv. Mater. Interfaces, vol. n/a, no. n/a, p. e00490, 2025, DOI: 10.1002/admi.202500490.
3. Z. Razaghi and G. Zhu, "Microscopic Characteristics of Kinking Phenomenon in Vertically Free-Standing Nanowires," *Crystals*, vol. 13, no. 10, Art. no. 10, Oct. 2023, IF: 2.4. DOI: 10.3390/cryst13101459.
4. Z. Razaghi, D. Y. Xie, M. Lin, and G. Zhu, "Ion Beam-Induced Bending of TiO_2 Nanowires with Bead-Like and Prismatic Shapes," *RSC Adv.*, vol. 12, no. 9, pp. 5577–5586, 2022, IF: 4.08. DOI: 10.1039/D1RA09122K.

Conference Presentations and Posters:

1. Z. Razaghi, G.Z. Zhu, "In Growth Embedding of Au Nanoparticles in TiO_2 Nanowires via Ni-Modified Seeds," Microscopy Society of Canada Meeting (2025)- oral presentation.
2. Z. Razaghi, G.Z. Zhu, "Ni-Mediated Endotaxial Growth of Au Nanoparticles Within TiO_2 Nanowires," Canadian Materials Science Conference (2025)- oral presentation.

   Highlight: Keynote speaker and session chair in the Advanced Materials Characterization and Testing session.

3. Z. Razaghi, G.Z. Zhu, "Seed Composition Engineering for Morphology Control in TiO_2 Nanowires," Manitoba Materials Conference (2025)- poster.

   Highlight: Recipient of an Honorable Mention for Best Ph.D. Student Poster.

4. Z. Razaghi, G.Z. Zhu, "Ag-Rich Segregation Effects on TiO_2 Nanowire Morphology and Growth Direction," Microscopy Society of Canada (2024)- poster.

   Highlight: Recipient of the Canadian Foundation for the Development of Microscopy (CFDM) Award in recognition of my impactful research in the field.

   Highlight: Recipient of the Student Leadership Award as the president of the Microscopy Society of Canada Central Student Chapter.

   Highlight: First Place Winner in the Microscopy Image Competition.

5. Z. Razaghi, G.Z. Zhu, “Vapor–Adsorbate–Solid Growth of Rutile Nanowires and the Impact of Growth Parameters on the Nanowire Instability,” Manitoba Materials Conference (2024)- poster.

   Highlight: Second Place Winner in the Microscopy Image Competition.

6. Z. Razaghi, G.Z. Zhu, “Controlling the Morphology of TiO_2 Nanowires with Bimetallic Seeds: Insights into the Growth Mechanism,” Canadian Materials Science Conference (2023)- oral presentation.

   Highlight: Recipient of the Student Award for the presented research work.

   Highlight: First Place Winner in the Microscopy Image Competition.

7. Z. Razaghi, G.Z. Zhu, “Controlling the Unseen World: Manipulating TiO_2 Nanowires for Future Technologies,” Manitoba Materials Conference (2023)- poster.

8. Z. Razaghi, M.H. Lin, G.Z. Zhu, “Ion Beam Irradiation of TiO_2 Nanowires with Bead-Like and Prismatic Shapes,” Microscopy and Microanalysis (2022)- paper and oral presentation.

9. Z. Razaghi, G.Z. Zhu, “Vapor-Based Growth of Rutile Nanowires,” Microscopy Society of Canada Symposium (2021)- poster.

List of Tables

List of Figures

List of Acronyms

1D	One-Dimensional
2D	Two-Dimensional
CLS	Canadian Light Source
CN	Coordination Number
DFT	Density Functional Theory
DW	Debye-Waller factor
EDX	Energy-Dispersive X-Ray Spectroscopy
EXAFS	Extended X-Ray Absorption Fine Structure
FCC	Face-Centered Cubic
FFT	Fast Fourier Transform
HAADF	High-Angle Angular Dark Field
HRTEM	High-Resolution Transmission Electron Microscopy
LCF	Linear Combination Fitting
NP	Nanoparticle
NW	Nanowire
OR	Orientation Relationship
SAED	Select Area Electron Diffraction
SEM	Scanning Electron Microscopy

STEM	Scanning Electron Microscopy
TEM	Transmission Electron Microscopy
TPB	Triple Phase Boundary
VLS	Vapor-Liquid-Solid
VS	Vapor-Solid
VSS	Vapor-Solid-Solid
VAdS	Vapor-Adsorbate-Solid
XAFS	X-Ray Absorption Fine Structure
XANES	X-Ray Absorption Near-Edge Structure
XAS	X-Ray Absorption Spectroscopy
XRD	X-Ray Diffraction

List of Symbols

A	Cross-section of nanowire
A*	Area of the nucleus
D	Lattice spacing
δ	Inclined angle of the faceted nanowire
δh	Standard deviation of the nanowire length
ε_{ML}	Interaction energy between the compound metal and liquid seed
$\Delta\xi_s$	Chemical potential difference between the seed and vapor
$\Delta\xi_{sn}$	Chemical potential difference between the seed and nanowire
$\Delta\xi_n$	Chemical potential difference between the nanowire and vapor
Δ_d	Formation energy of defects
Δ_s	Free energy change of the seed surface
Δ_{sn}	Free energy change of the seed-nanowire interface
ΔG	Gibbs free energy change for nanowire formation
ΔG_s*	Gibbs free energy change for nucleation on seed surface
$\Delta G_{nn}*$	Gibbs free energy change for self nucleation
ΔG_n*	Gibbs free energy change for nucleation on nanowire surface
$\Delta G_{sn}*$	Gibbs free energy change for nucleation on seed-nanowire
$\Delta G^*{}_{TPB}$	Gibbs free energy change for nucleation on TPB

E	Energy of X-ray photons
E_0	Edge energy in XAS spectrum
f_i	Backscattering amplitude of X-rays
$\gamma_{interfacial}$	Interfacial energy
γ_{new}	New surface energy
$\gamma_{original}$	Original surface energy
γ_n	Lateral surface energy of nanowire
γ_{sn}	Seed-nanowire interfacial energy
γ_s	Surface energy of the seed
h	Length of the nanowire
h*	Length of the nucleus
$\bar{\mathrm{h}}$	Average nanowire length
I_1	Intensity of transmitted X-rays
I_f	Intensity of fluorescence X-rays
I_0	Intensity of incident X-rays
I_2	Intensity of X-rays after transmitting reference foil
χ	EXAFS function
k	Wave number

λ	Mean free path of photoelectrons
M_i	Model of Au-Ti alloys
N_i	Coordination number
n_w	Number of nanowires
μ	Absorption coefficient of X-ray
ξ_v	Chemical potential of the vapor phase
ξ_s	Chemical potential of the seed
ξ_n	Chemical potential of the nanowire
P	Nanowire perimeter
P*	Nucleus perimeter
R_i	Distance between absorbing center and scattering shell
S_0	Amplitude reduction factor
σ_i	Debye-Waller factor
θ	Seed-nanowire contact angle
ϑ	Adhesion energy
φ	Grazing angle in the XAS setup
Ψ	Backscattering phase shift of X-rays
x	Thickness of the sample
X, Y, Z	Coordination of samples in the space

Copyrighted Materials

Chapters 2 through 6 of this thesis include content that has been adapted, with modifications, from previously published, submitted, or in-preparation works. Specifically:

- Chapter 2, sections 2.1.1, 2.1.1.1, a part of 2.1.1.2, and 2.3.2 along with Figures 2-2 and 2-8, are adapted from:

  Z. Razaghi and G. Zhu, "Microscopic Characteristics of Kinking Phenomenon in Vertically Free-Standing Nanowires," *Crystals*, vol. 13, no. 10, Art. no. 10, Oct. 2023, IF: 2.4. DOI: 10.3390/cryst13101459.

- A part of Chapter 3 (section 3.4) and chapter 6 is drawn from:

  Z. Razaghi, G. Zhu, M. Lin, N. Chen, K. Cui, and G. Zhu "Spectroscopic Insights into Controlling Sidewall Faceting of TiO_2 Nanowires via Au-Ag Bimetallic Seeds," (Submitted).

- Chapter 4 is based on a work in preparation.

- Chapter 5 is based on:

  Z. Razaghi and G. Zhu, "Ni-Assisted Endotaxial Growth of Au Nanoparticles Within TiO_2 Nanowires," Adv. Mater. Interfaces, vol. n/a, no. n/a, p. e00490, 2025, DOI: 10.1002/admi.202500490.

- Chapter 6 is based on:

Z. Razaghi, G. Zhu, M. Lin, N. Chen, K. Cui, and G. Zhu "Spectroscopic Insights into Controlling Sidewall Faceting of TiO_2 Nanowires via Au-Ag Bimetallic Seeds," Langmuir, Oct. 2025, DOI: 10.1021/acs.langmuir.5c03334.

Additionally, several figures used in Chapter 2—namely Figures 2-1, 2-3, 2-6, 2-7, 2-9, and 2-10—have been reproduced from previously published sources for the literature review. Permissions to use these images were obtained from the respective publishers, including AIP Publishing, John Wiley and Sons, American Chemical Society, and Royal Society of Chemistry. Full citations for these sources are provided in the corresponding figure captions.

Chapter 1

Introduction

1.1. Research Background

Over the past few decades, advancements in nanotechnology have greatly enhanced our ability to study and manipulate the atomic structure and properties of materials. Metal oxides, prized for their remarkable stability, tunable electronic properties, cost-effectiveness, and abundance, have found extensive use in applications such as sensors, catalysis, energy conversion, and storage [1], [2], [3]. At the nanoscale, these materials exhibit unique and exciting properties, which arise from their large surface area and quantum size effects [4]. Among the various nanostructures, one-dimensional (1D) forms are particularly attractive because their confined geometry and high surface-to-volume ratio enhance surface reactivity, adsorption, and transport phenomena. These characteristics make oxide nanowires promising for applications such as photocatalysis, gas sensing, and transparent electronics [5], [6], [7]. Consequently, researchers have focused extensively on developing reliable methods to synthesize high-quality oxide nanowires and improve the precision of fabrication techniques.

A critical step in producing 1D nanostructures is the control of directional growth. One common approach is the use of a seed material, which directs the growth by providing a nucleation interface. This concept underpins the metal-mediated growth process, first demonstrated by Wagner and Ellis in 1964, who studied silicon whisker growth in the presence of gold impurities [8]. This process, known as the vapor-liquid-solid (VLS) mechanism, has since been widely adapted for fabricating 1D nanostructures such as nanowires from semiconductors in groups IV, III-V, and II-VI. However, despite progress in the synthesis of oxide nanowires, achieving uniform and precisely defined structures remains a significant challenge. The growth process is highly sensitive to various factors, including material supply, temperature, and the properties of the seed material [9], [10]. Furthermore, mechanisms governing the morphology of oxide nanostructures are still debated, highlighting the need for more in-depth studies to resolve these uncertainties.

This research emphasizes TiO_2, a versatile semiconductor widely used in catalysis and energy applications. Notably, vertically aligned TiO_2 nanowire arrays have been integrated into dye-sensitized solar cells [11]. Advancing these technologies requires the fabrication of high-quality TiO_2 nanowires by optimizing oxygen partial pressure and controlling nanowire morphology through seed engineering.

1.2. Research Motivation and Importance

Among the challenges in synthesizing uniform and well-defined TiO_2 nanowires [12], [13], [14], a recently developed method, known as the vapor-adsorbate-solid (VAdS), has enabled their growth, though several fundamental questions remain unresolved [15]. This technique places TiO_2 substrates inside a quartz tube filled with argon gas, removing the need for external material flux or temperature gradients. It has successfully produced uniform nanowires up to tens of microns in length. While previous studies in open systems (with temperature and material flux gradients) highlight oxygen and material flux as critical factors—with only narrow windows producing nanowires [16]—these effects have yet to be explored in this enclosed system. In this context, oxygen partial pressure—originating from impurities in the argon gas and air—can play a key role in determining growth rate, and identifying its optimal range is essential for consistent synthesis.

On the other hand, the seed composition as another key parameter strongly influences the growth mechanism and resulting morphology, leading to a range of structures including vertical, kinked, bead-like, prismatic nanowires, or hybrid nanosystems with embedded nanoparticles. Our earlier results demonstrated that the growth direction of TiO_2 nanowires shifts from $\langle 110 \rangle_{\mathrm{TiO_2}}$ with a bead-like shape to $\langle 111 \rangle_{\mathrm{TiO_2}}$ with a prismatic shape when using Au–Ag seeds [12]. Unexpectedly, these seeds exhibit distinct Au-rich and Ag-rich domains at the growth front. Further investigation into the exact location of Ag-rich domain and bonding characteristics of the involved elements, the resulting miscibility gap opening in the isomorphous Au-Ag system, and the role of compositional heterogeneity at the growth front, will deepen our understanding of seed engineering for vapor-phase growth and the potential to tailor nanostructures for enhanced functionalities.

In addition to variations in growth direction and shape, our study revealed hybrid TiO_2 nanostructures with embedded nanoparticles, resembling nanopeapods. These formed when trace Ni was unintentionally introduced, modifying the TiO_2–Au interface during growth. The results indicate that, beyond seed composition and morphological changes, the crystallographic nature of the Au–TiO_2 interface plays a decisive role in governing the embedding process. Understanding such interfacial effects is essential for achieving controlled growth and for leveraging seed engineering to design functional oxide nanostructures.

Altogether, the controlled fabrication of TiO_2 nanowires remains challenging due to the limited mechanistic understanding of their growth. A comprehensive investigation of the key synthesis parameters, combined with deliberate seed composition engineering, is crucial for advancing both the fundamental understanding of nanowire formation and their integration into future technologies.

1.3. Organization of the Thesis

The thesis is organized as follows. Chapter 2 reviews prior studies on nanowire fabrication, with emphasis on VLS-like mechanisms, thermodynamic aspects of growth, and the main factors influencing the morphology of oxide nanowires. It also introduces the TiO_2 system synthesized through various vapor- and liquid-phase routes, including the recently developed VAdS method, and discusses recent advances in tailoring nanowire morphology via seed composition engineering. Chapter 3 details the experimental design, highlighting the customized setup introduced to both the nanowire synthesis system and the characterization procedures. Chapter 4 presents the results of nanowire growth controlled by oxygen partial pressure, while Chapter 5 examines the influence of Au–Ni seeds on the formation of hybrid nanostructures with embedded nanoparticles, with a particular focus on the Au–TiO_2 interface. Chapter 6 explores how Au–Ag seeds modify nanowire morphology and growth direction, emphasizing spectroscopic analysis and local chemical bonding. Chapter 7 summarizes the main conclusions and outlines directions for future work. Finally, Appendix A provides additional details on the synthesis process, and Appendix B offers further information on the spectroscopic data analysis.

Chapter 2

Literature Review

This chapter begins with Section 2.1, introducing the VLS-like growth mechanism, including key thermodynamic and mass transport aspects. Section 2.2 explores parameters influencing oxide nanowire growth, such as material flux and seed composition. Section 2.3 discusses morphological engineering—covering features like kinking and nanopeapods. Section 2.4 introduces the TiO_2 system, outlining its synthesis through various methods, including the recently developed vapor–adsorbate–solid (VAdS) approach. Finally, Section 2.5 summarizes critical insights and outlines the research objectives.

2.1. Vapor-Liquid-Solid (VLS)- Like Growth

Particles composed of elements or compounds have been widely used to facilitate nanowire growth via the vapor-liquid-solid (VLS) mechanism originally introduced by Wagner and Ellis in 1964 [8]. In this method (illustrated in Figure 2-1), nanoscale seeds—commonly gold—absorb vapor-phase precursors, forming a liquid-phase alloy. When the concentration of the growth species in the alloy surpasses its solubility limit, solid material begins to deposit at the interface between the liquid seed and the solid substrate, promoting anisotropic nanowire growth. In certain material systems, these liquid seeds may also assist in breaking down the vapor-phase precursors, which has led some researchers to describe them as catalysts [17], [18]. However, because this reactive role is not universally observed across all systems, the term "seed" will be used throughout this thesis to describe these nanoparticles.

VLS growth offers several advantages over other synthesis techniques. Compared to top-down lithographic approaches, which often involve complex and expensive processes, VLS allows spontaneous growth of nanowires with diameters as small as the seed size, without the need for patterning [19]. It also provides better control than vapor–solid (VS) growth, which lacks a liquid-phase seed and is typically slower and less directional. Additionally, compared to solution-based methods like hydrothermal synthesis, VLS-grown nanowires tend to have higher purity, superior crystallinity, and better alignment—qualities essential for electronic and photonic applications [20].

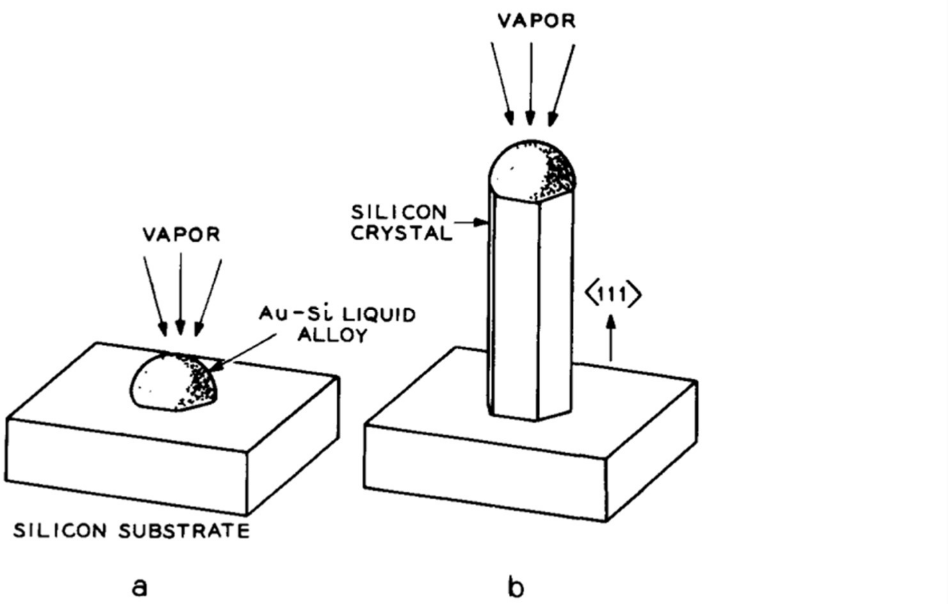

Figure 2-1. Growth of silicon nanowires via the VLS mechanism using gold seeds on a silicon substrate. Adapted with permission from [8].

2.1.1. Thermodynamic Considerations

To gain insight into the VLS growth mechanism, numerous studies have been conducted. In a conventional VLS process, the transport of growth species typically involves the following stages: (i) mass transport of growth species to the seed surface; (ii) absorption of growth species at the seed; (iii) diffusion of growth species inside the seed; and (iv) incorporation of growth species into nanowires, i.e., the nucleation and lateral expansion of the growth species at the seed/nanowire interface. The absorption and precipitation processes (steps (i) to (iii)) are driven by differences in chemical potential between the vapor phase (ξ_v), the seed (ξ_s), and the nanowire (ξ_n). For nanowire growth to occur, the condition $\xi_v > \xi_s \geq \xi_n$ must be satisfied, ensuring a positive supersaturation ($\Delta\xi_s$, $\Delta\xi_{sn}$, $\Delta\xi_n$) that promotes material incorporation and precipitation [21]. Such differences in chemical potential—and the resulting driving forces—can be enhanced by introducing an external material flux, establishing a temperature gradient between the source and the substrate, and employing a carrier gas to deliver vapor-phase species from the source to the seed.

2.1.1.1. Gibbs Free Energy in a Three Phase System

The rate-determining step is typically recognized as step (iv) [20]. By assessing the chemical potential of all species involved in this step, the change in free energy ($\Delta\boldsymbol{G}$) can be evaluated using the following equation [22].

$$\Delta\boldsymbol{G} = \boldsymbol{A}\cdot\boldsymbol{h}\cdot\Delta\boldsymbol{\xi} + \boldsymbol{P}\cdot\boldsymbol{h}\cdot\boldsymbol{\gamma_n} + \Delta_{\boldsymbol{s}} + \Delta_{\boldsymbol{sn}} + \Delta_{\boldsymbol{d}} \tag{2-1}$$

In which, $\boldsymbol{h}$ is the length of nanowires. The first term describes the driving force, where $\Delta\boldsymbol{\xi}$ is the difference of chemical potential between the growth species within the seed and those as the nanowires; $\boldsymbol{A}$ is the cross-section of the nanowire.

The second term defines the contribution of the surface energy of the nanowire sidewall. $\boldsymbol{P}$ is the nanowire perimeter. $\boldsymbol{\gamma_n}$ is the effective lateral surface energy of the nanowire. When a columnar nanowire is enclosed by different facets, $\boldsymbol{\gamma_n} = \sum_{\boldsymbol{i}}\boldsymbol{x_i}\cdot\boldsymbol{\gamma_{ni}}$ refers to the contribution of individual facets, in which, $\boldsymbol{x_i}$ and $\boldsymbol{\gamma_{ni}}$ are the fraction and surface energy of facet $\boldsymbol{i}$. This simple model is employed to predict the switching of growth directions in different nanowires such Si [23], Ge [24], [25], GaAs [26], and GeSn [27]. Figure 2-2 presents a diagram illustrating the configurations at the interfaces between the seed and nanowires, encompassing the parameters discussed earlier.

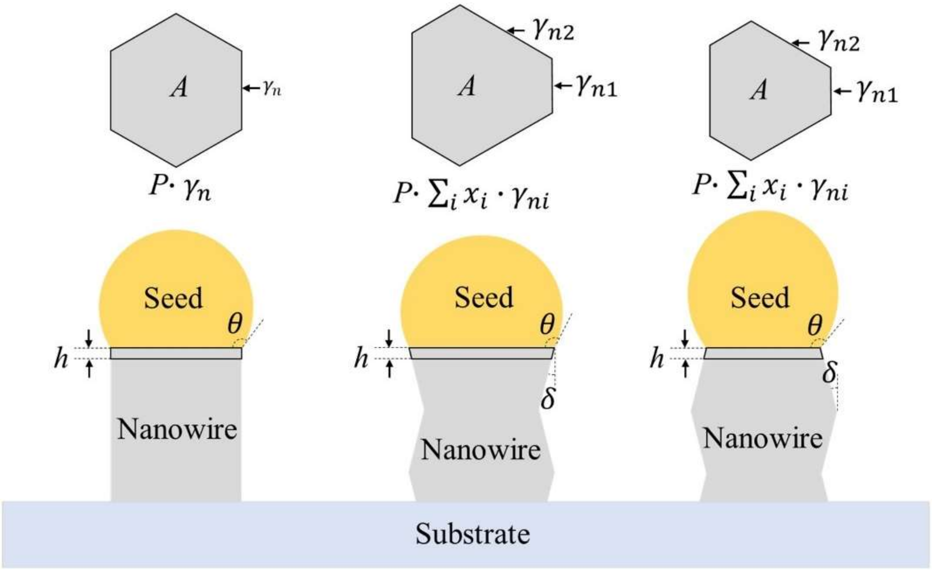

Figure 2-2. Geometries at the seed-nanowires interface. A and P are the area and perimeter of grown nanowires with height h, respectively. θ is the contact angle. From left to right are cylindrical nanowires, nanowires with widening facets, and nanowires with narrowing facets. δ is the inclined angle for either widening facets or narrowing facets. γ_n and γ_{ni} are the surface energy of facets. Adapted from [22] under CC BY license

If facet $\boldsymbol{i}$ has an incline angle $\boldsymbol{\delta}$ with the nanowire growth direction (as shown in Figure 2-2 middle and right configurations), $\boldsymbol{\gamma_n = \sum_i x_i \cdot \frac{\gamma_{ni}}{cos\delta}}$ includes a correction factor considering the actual area of facet *i* per unit length [28]. The formation of inclined facets usually involves changes in the shape of seeds and the area of the seed-nanowire interface, the free energy change of which is defined as $\Delta_{\boldsymbol{s}}$ and $\Delta_{\boldsymbol{sn}}$, respectively. Although the precise formulations of $\Delta_{\boldsymbol{s}}$ and $\Delta_{\boldsymbol{sn}}$ can become intricate, they are associated with the contact angle $\boldsymbol{\theta}$, incline angle $\boldsymbol{\delta}$, seed surface energy $\boldsymbol{\gamma_s}$, and seed-nanowire interface energy $\boldsymbol{\gamma_{sn}}$. These relationships are usually derived with the assumptions that the seed retains a consistent volume during growth and the elementary volumes of the growth species are the same inside the seed and the nanowire [20]. If $\boldsymbol{h}$ is much smaller than the radius of the seed, $\Delta_{\boldsymbol{s}}$ and $\Delta_{\boldsymbol{sn}}$ can be simplified as the product of surface/interface energies and trigonometric functions of relevant angles, and successfully predicts the sawtooth growth and its diameter-dependent spacing of Si [28], Ge [29], GaP [29], TiO_2 [30] nanowires. Furthermore, crystal defects, such as twin and stacking faults, are likely involved during the growth of the nanowire [31], [32], [33]. Correspondingly, the formation energy of these twins or stacking faults referred to as $\Delta_{\boldsymbol{d}}$, also contributes to the nanowire growth ($\Delta \boldsymbol{G}$). Incorporating the $\Delta_{\boldsymbol{d}}$ term, sawtooth in GaAs [34] and InP [35] nanowires as well as kinking in Ge nanowires [36] are well predicted.

2.1.1.2. Selection of Nucleation Site

In cases where the rate-limiting process is nucleation, Equation 2-1 can be slightly modified to describe the nucleus at the seed-nanowire interface, i.e., the growth front. Variables $\boldsymbol{A}^*$, $\boldsymbol{P}^*$, $\boldsymbol{h}^*$, and $\boldsymbol{\gamma_n}^*$ correspond to the area, perimeter, and effective surface/interface energy of the nucleus, respectively. Depending on the nucleation sites, the detailed formulation of these variables may differ. To determine the most favorable nucleation site, various possible nucleation scenarios within a three-phase VLS system are illustrated in Figure 2-3. These include: (i) heterogeneous nucleation at the seed surface, (ii) homogeneous self-nucleation, (iii) nucleation on the nanowire surface, (iv) nucleation at the seed–nanowire interface, and (v) nucleation at the triple-phase boundary (TPB), where the growth species, seed, and nanowire meet.

As an example, nucleation at the seed-nanowire interface, $\Delta G_{sn}*$, is simplified and expanded to incorporate various surface and interface energy contributions, excluding the influence of crystallographic defects, as expressed in Equation 2-2 [21].

$$\Delta G^*{}_{sn} = -A^*h^*\Delta\xi_n + P^*h^*\gamma_n + A^*(\gamma_{sn} + \gamma_n - \gamma_s) \tag{2-2}$$

In contrast to Equation 2-1, which uses a general term for the difference in chemical potential ($\Delta\xi$) without considering the specific nucleation site, this equation introduces $\Delta\xi_n$ to indicate the location where nucleation occurs. The difference in chemical potential between the vapor and the nanowire ($\Delta\xi_n$) is used here, rather than that between the seed and the nanowire ($\Delta\xi_{sn}$), because the driving force for nucleation originates from the material flow between the vapor and the seed, not from the seed to the nanowire interface. Additionally, $\Delta\xi_n$ is greater than $\Delta\xi_{sn}$, providing a stronger driving force for nucleation at the vapor-facing interface. The formation of new seed-nanowire interface and nanowire surface adds their surface energies ($A^*\gamma_{sn}$ and $A^*\gamma_n$, respectively) to Equation 2-2, while the replaced seed surface subtracts $A^*\gamma_s$. The interfacial energy γ_{sn} is related to γ_s, γ_n, and the adhesion energy (ϑ) according to the Dupre equation [37], as shown in Equation 2-3.

$$\gamma_{interfacial} = \gamma_{original} + \gamma_{new} - \vartheta \tag{2-3}$$

In this equation, γ_i refers to the interfacial energy (γ_{sn}), $\gamma_{original}$ is the original surface energy (γ_s), γ_{new} is the new surface energy (γ_n), and ϑ is the adhesion energy representing the bonding at the interface. The corresponding Gibbs free energy changes for the interfaces in Figure 2-3 are summarized in Table 2-1.

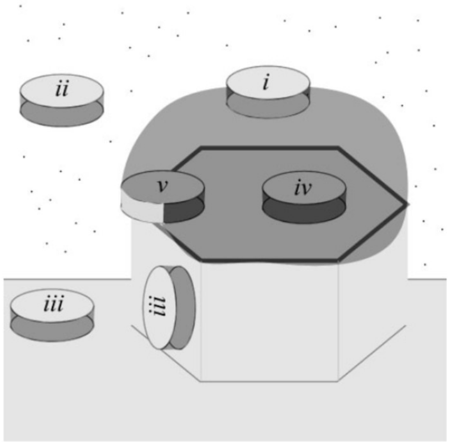

Figure 2-3. Nucleation at different interfaces in VLS system: (i) heterogeneous nucleation at the seed surface; (ii) homogeneous nucleation (self-nucleation); (iii) nucleation on the nanowire surface; (iv) nucleation at the seed–nanowire interface; and (v) nucleation at the triple-phase boundary (TPB). Adapted with permission from [21].

Table 2-1. Gibbs free energy changes for different nucleation locations, i.e., i, ii, iii, iv, and v [21].

Interface	ΔG	Note
i	$\Delta G^*{}_s = -A^*h^*\Delta\xi_s + P^*h^*\gamma_n + A^*(\gamma_{sn} + \gamma_n - \gamma_s)$ $\Delta G^*{}_s = -A^*h^*\Delta\xi_s + P^*h^*\gamma_n + A^*(2\gamma_n - \vartheta)$	Nucleation on a heterogeneous surface $\gamma_{interfacial} = \gamma_{sn}, \gamma_{original} = \gamma_s,$ $\gamma_{new} = \gamma_n$
ii	$\Delta G^*{}_{nn} = -A^*h^*\Delta\xi_n + P^*h^*\gamma_n + 2A^*\gamma_n$	Self-nucleation: No interaction between the seed and nanowire $\gamma_{interfacial} = \gamma_n, \gamma_{original} = 0,$ $\gamma_{new} = \gamma_n$ $\vartheta = 0$
iii	$\Delta G^*{}_n = -A^*h^*\Delta\xi_n + P^*h^*\gamma_n$	Nucleation on a homogeneous nanowire surface: Nucleus–surface interactions are ideal (the specific adhesion energy is high). $\vartheta_{max} = 2\gamma_n$
iv	$\Delta G^*{}_{sn} = -A^*h^*\Delta\xi_n + P^*h^*\gamma_{sn}$	Nucleation on a homogeneous nanowire at the seed-nanowire interface $\gamma_{interfacial} = 0, \gamma_{original} = \gamma_{sn},$ $\gamma_{new} = \gamma_{sn}$ $\vartheta_{max} = 2\gamma_{sn}$

v	$\Delta G^*{}_{TPB} = -A^* h^* \Delta\xi_n + P_{sn}{}^* h^* \gamma_{sn} + P_n{}^* h^* \gamma_n$	TPB line: The edge energy is split in two parts $\gamma_{interfacial} = 0, \gamma_{original} = \gamma_{sn},$ $\gamma_{new} = \gamma_{sn}$ $\vartheta_{max} = 2\gamma_{sn}$

Comparing cases (i) and (ii), nucleation at the vapor–seed interface (with $\vartheta > 0$) is more favorable than self-nucleation. Similarly, high adhesion energy (ϑ) lowers ΔG, making homogeneous sites (iii, iv, v) generally preferred over heterogeneous ones. Among homogeneous sites, comparing nucleation on the nanowire surface with that at the seed–nanowire interface is more complex because the two regions exhibit different chemical potentials. Since the chemical potential difference is typically greater at the nanowire surface, nucleation is more likely to occur there. However, nucleation also depends on edge energy, which is influenced by interfacial interactions and can be inferred from the wetting angle (θ) using Young's relation (Figure 2-4) [37]:

$$\gamma_n = \gamma_s + \gamma_{sn} \cos(\theta) \tag{2-4}$$

A small wetting angle ($\theta_1 < 90°$) indicates strong seed–nanowire interaction, favoring nucleation at the seed-nanowire interface, while a large angle ($\theta_2 > 90°$) indicates weaker interaction, shifting preference to the nanowire surface. Thus, material combinations with strong seed–nanowire interaction support seed-nanowire nucleation, while weakly interacting systems favor the nanowire side, as described by Nebol'sin and Shchetinin [38]. The triple-phase boundary (TPB), in direct contact with the vapor, experiences the highest chemical potential difference and provides geometric flexibility. The nucleus can adjust its shape across both interfaces, minimizing total ΔG. This makes the TPB a highly favorable nucleation site in certain systems, as supported by experimental studies reporting nucleation rates orders of magnitude higher than at other interfaces.

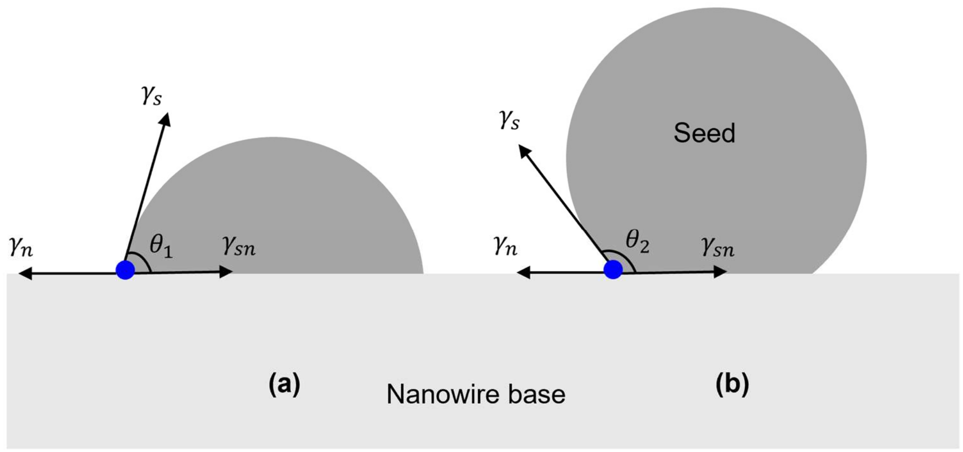

Figure 2-4. Liquid droplet on solid surface with equilibrium contact angle $\theta_1 < \pi/2$ (a) and $\theta_2 > \pi/2$ (b). The blue dot denotes the triple-phase boundary (TPB).

In summary, VLS nanowire growth depends on a sufficient chemical potential difference ($\xi_v > \xi_s \geq \xi_n$) to drive material transport and a reduction in Gibbs free energy (ΔG) at the growth front. External flux, temperature gradients, and carrier gases enhance this driving force. At the same time, surface and interface energies—including facet-dependent lateral energies and interfacial adhesion—govern growth stability and direction. The triple-phase boundary (TPB) is often the most favorable nucleation site because it exhibits a higher chemical potential difference relative to the growth species ($\Delta\xi_n$), along with geometric flexibility in minimizing ΔG. Thus, both chemical potential and surface energy must be optimized to enable controlled nanowire growth, particularly via TPB nucleation.

2.1.2. Mass Transport Path at the Growth Front

Understanding how growth species are transported to the nanowire growth front is key to revealing the growth mechanism and tailoring nanowire morphology. Although elemental (e.g., Si, Ge, Sn) and compound nanowires—including III-V semiconductors (e.g., GaAs, InP, InAs, GaP), II-VI compounds (e.g., CdSe, ZnS), and oxides (e.g., ZnO, MgO, SnO_2, TiO_2, Al_2O_3)—often exhibit similar growth geometries, their mass transport pathways, especially near the triple-phase boundary (TPB), differ significantly due to differences in chemical reactivity, volatility, and solubility within the seed material. Figure 2-5 shows various possible mass transport routes to the seed.

In elemental nanowires such as Si, atomistic simulations and in situ studies have revealed that growth species predominantly diffuse through the bulk of the liquid alloy droplet (path 1,2 in Figure 2-5). The precipitation of Si typically occurs near the center of the liquid–solid interface. However, the TPB plays an important role in initiating nucleation. Faceting at the TPB facilitates two-dimensional nucleation and step-flow growth along the main nanowire axis. While mass transport in this system is mostly through the droplet interior, the TPB still serves as a critical site for lowering the nucleation barrier and anchoring the interface morphology [39].

In contrast, compound nanowires, especially oxides, involve significantly more complexity. Many binary compounds do not form stable ternary alloys with metal seeds, unlike GaAs, which forms a pseudo-binary phase with Au [40]. Typically, only one component (e.g., Ga in GaAs or Zn in ZnO) is detected in the seed particle, while oxygen is rarely incorporated due to its low solubility in metals like Au—estimated to be 10^{-13} at 400 K and 10^{-5} at 1000 K [41]. This raises fundamental questions about how oxygen reaches the growth front in oxide nanowire systems. Moreover, the presence of a liquid alloy does not guarantee a VLS-like growth pathway. The precipitation behavior of compound materials depends on multiple factors, including vapor-phase composition, phase diagrams, and interfacial reactions, which remain poorly understood due to the lack of thermodynamic data for multi-component systems.

For example, Oh et al. [42] studied Al_2O_3 nanowire growth using Al seeds under high vacuum, relying on trace oxygen from residual gases. They observed oscillatory dissolution and regrowth at edge facets, suggesting that aluminum diffused through the droplet (path 1,2 in Figure 2-5) while oxygen arrived at the TPB and reacted at the interface (path 4 in Figure 2-5). Similarly, Hejazi et al. [43] detected Zn within Au droplets during ZnO nanowire growth, consistent with Zn bulk diffusion through the seed (path 1,2 in Figure 2-5) and interfacial oxidation near the TPB via CO/CO_2 equilibrium (path 4 in Figure 2-5). In contrast, Simon et al. [44] reported surface diffusion of Zn toward the droplet edge (path 1,3,4 in Figure 2-5), where ZnO nucleation occurred directly at the TPB (path 4 in Figure 2-5) under a continuous O_2 flow. These varied mechanisms underscore the pivotal role of the TPB in oxide nanowire growth. In such systems, the TPB may not only facilitate nucleation but also can act as a reaction zone where metal and oxygen species converge to form the compound phase when oxygen solubility in the seed is limited.

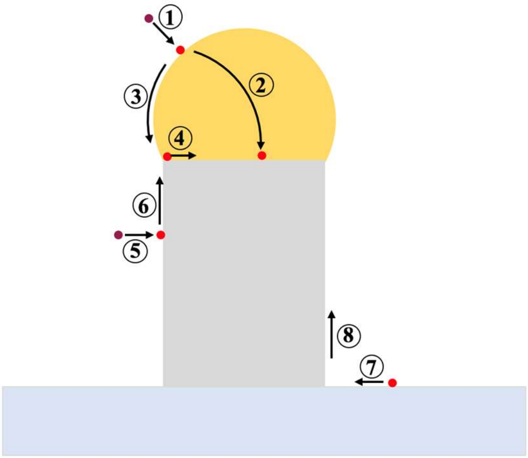

Figure 2-5. Schematic of various reported mass transport pathways of growth species to the nanowire growth front.

2.2. Factors Controlling the Growth of Oxide Nanowires

The growth of oxide nanowires through vapor-phase methods is governed by a range of thermodynamic and kinetic parameters. Among the key factors influencing nanowire formation and morphology are the growth temperature, substrate, material flux, and seed properties. Each of these elements affects the difference in chemical potential, nucleation barrier, and directional solidification processes at the nanowire tip.

An optimal temperature is crucial to generate sufficient precursor vapor and activate diffusion processes while maintaining conditions for directional growth. For instance, ZnO nanowires typically grow between 500–700 °C, where adequate Zn vapor pressure and surface diffusion promote axial elongation [45]. At lower temperatures (<400 °C), vapor pressure is insufficient for sustained growth, while at higher temperatures (>750 °C), enhanced lateral diffusion may lead to polycrystalline films or isotropic structures [46], [47]. Similarly, TiO_2 nanowires often require 900–1000 °C to sublimate Ti-based sources and mobilize oxygen for oxide formation [48].

Substrate selection also shapes nanowire orientation, crystallinity, and interfacial behavior. In some systems, lattice-matched substrates—such as rutile TiO_2 for rutile nanowires [15] or ZnO-buffered sapphire for ZnO [49], [50]—support epitaxial alignment. However, many oxide nanowires are grown on mismatched or elemental substrates like Si, Ti, glass, or sapphire, depending on the growth strategy. For example, Ti substrates can act as both substrate and metal source in TiO_2 growth, where chemical compatibility outweighs lattice matching [14]. In device-related applications, substrates like Si/SiO_2 [12], [51] and Al [52] are chosen for their compatibility, with seed layers or surface treatments (e.g., Au, ZnO) aiding nucleation and directional growth.

In addition to the temperature and substrate, material flux and seed composition further influence nucleation, growth rate, and morphology. These factors are discussed in the following sections.

2.2.1. Material Flux Window

Material flux plays a pivotal role in determining whether oxide nanowires can grow directionally via a VLS-like mechanism, and its influence has been extensively studied across various oxide systems, including SnO_2, In_2O_3, ZnO, MgO, CaO, NiO, MnO, Eu_2O_3, Sm_2O_3, and TiO_2 [16], [48], [53]. In these systems, an optimal material flux window—determined by the balance between the metal growth species and the oxygen partial pressure—is essential for sustaining efficient nanowire growth. Within this window, nanowires can grow unidirectionally without interference from vapor–solid (VS) growth (dominant at high material flux) or suppressed VLS growth rates (at low flux), as illustrated in Figure 2-6.

This behavior stems from the difference in nucleation energy barriers: the seed-nanowire interface, stabilized by the seed, exhibits lower interfacial energy (γ_{ns}) than the nanowire surface energy (γ_n). As a result, nucleation is energetically favored at the nanowire-seed interface within a narrow supersaturation range [20]. However, when the material flux exceeds this range, nucleation may also occur on the nanowire or substrate surface, leading to VS growth and disrupting directional nanowire elongation [54]. Importantly, the width of the material flux window depends on the bonding strength between the metal and oxygen atoms, which is often correlated with the material's melting point. For instance, MgO, which exhibits strong metal–oxygen bonding and a high melting point, supports a relatively wide growth window. In this case, the metal flux can range from 5×10^{17} to 3×10^{18} $\text{cm}^{-2}\cdot\text{s}^{-1}$, and the oxygen flux spans a broad range from 10^{-7} to 10 $\text{cm}^{-2}\cdot\text{s}^{-1}$, enabling robust nanowire growth under a variety of conditions [16], [53]. In contrast, SnO_2 and TiO_2—which have comparatively weaker metal–oxygen bonding—exhibit much narrower flux windows. In particular, TiO_2 nanowires have one of the narrowest known material flux ranges, with the optimal metal flux lying between 0.5×10^{17} and 1.5×10^{17} $\text{cm}^{-2}\cdot\text{s}^{-1}$, and its oxygen partial pressure must be maintained between 10^{-2} and 10^{-1} Pa [16], making it more challenging to achieve long and uniform nanowire growth.

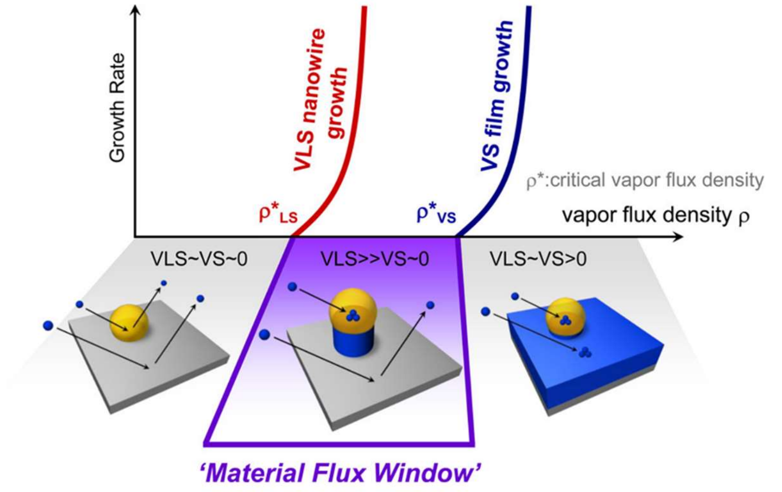

Figure 2-6. Diagram illustrating how the "material-flux window" concept guides VLS growth of metal-oxide nanowires. Adapted with permission from [53].

Therefore, oxide nanowire growth via VLS-like mechanisms critically depends on maintaining vapor flux within a well-defined material flux window. Outside this window, either the flux is too low to initiate nucleation (VLS $\approx$ VS $\approx$ 0), or too high, promoting competing VS film growth that overwhelms VLS (VLS $\ll$ VS). As a result, nanowire formation is not observed unless the flux conditions fall squarely within this narrow range. This sensitivity makes precise control of vapor flux especially important for materials like TiO_2, where the optimal growth window is particularly narrow.

2.2.2. Nanowire Seed

While Au is the most common seed material due to its high surface energy, chemical inertness, and thermal stability—properties that satisfy the stability models of Young [55] and Nebol'sin-Shchetinin's [38] as discussed in section 2.1.1—altering the seed composition can further tune interfacial properties such metal–oxygen bonding strength, wetting angle, and liquid–solid interfacial energy. These modifications can significantly impact nanowire growth kinetics, morphology, and the stability of the VLS-like process. Molecular dynamics (MD) simulations have shown that stronger bonding at the nanowire-seed interface enhances the adsorption and incorporation of vapor species, increasing nanowire growth rates and widening the material flux window. This is illustrated in Figure 2-7, where the metal–liquid (seed) interaction energy (ε_{ML}) controls the width of the VLS region. As ε_{ML} decreases, nucleation becomes less favorable at the nanowire-seed interface, allowing VS nucleation to dominate and disrupt unidirectional growth.

These theoretical insights are supported by experimental results. Zhu et al. [48] demonstrated that alloying Au with Sn lowered the VLS growth temperature of SnO_2, In_2O_3, and ZnO nanowires by over 150 °C, while broadening the oxygen partial pressure window for stable growth nearly tenfold. The addition of Sn increases the interaction energy between the seed and the incoming growth species, which reduces the activation barrier for incorporation at the nanowire–seed interface and stabilizes tip-led growth over a wider flux range. Klamchuen et al. [53] similarly showed that incorporating Ni or Cu into Au enabled stable growth of MgO, CaO, and MnO nanowires across a broader range of metal and oxygen fluxes. In both studies, modifying seed composition by introducing elements with stronger seed–metal bonding improved vapor species incorporation and enhanced tolerance to fluctuations in flux and temperature.

In addition to chemical composition, the physical properties of the seed, such as size and curvature, also influence growth behavior. Smaller seed particles exhibit higher curvature and Laplace pressure, which raises the chemical potential inside the droplet and shifts the supersaturation threshold required for nucleation [20]. As a result, very small nanoparticles (typically <10–20 nm) may delay or suppress nanowire nucleation, especially during early growth stages, and are also more prone to Ostwald ripening, which can destabilize them before growth initiates [56], [57]. In contrast, very large seed particles (typically >100–150 nm) can accumulate growth species more readily but may lead to excessively wide contact areas with the substrate, promoting film-like or polycrystalline growth instead of axial nanowire elongation [58].

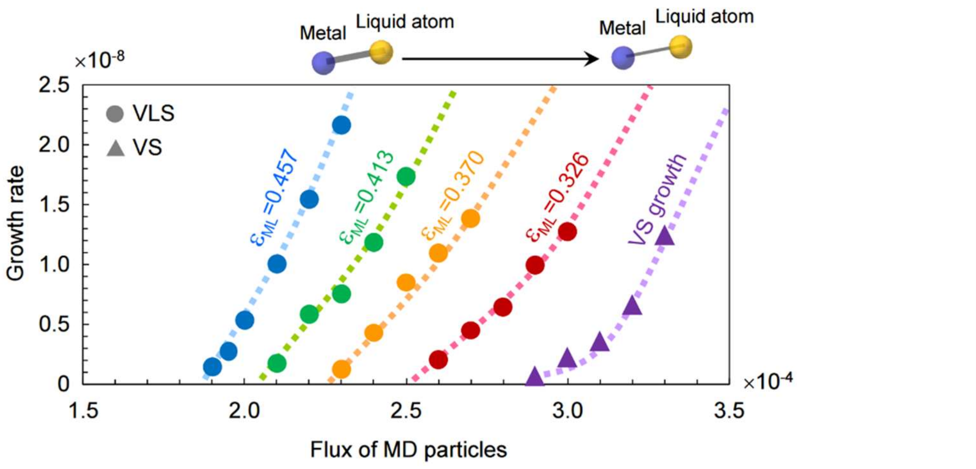

Figure 2-7. MD simulation results illustrating how variations in seed composition—reflected by changes in the bonding strength between the liquid seed and metal atoms—affect the width of the material flux window for VLS nanowire growth. Adapted with permission from [53].

2.3. Engineering the Morphology of Oxide Nanowires

The morphology of oxide nanowires can vary widely, influenced by both thermodynamic and kinetic factors during growth, as well as by post-growth treatments. While post-growth approaches such as ion-beam-induced bending [59] can tailor geometry after synthesis, in-growth modification offers the advantage of directly controlling nucleation and growth pathways, producing uniform structures while reducing the likelihood of defect formation. According to the thermodynamic framework discussed earlier (Equation 2-1), the total free energy change (ΔG) depends on the chemical potential difference ($\Delta\xi$), surface and interfacial energies, and the energy associated with defect formation (Δd). When competing growth pathways have similar ΔG values, even slight changes in growth conditions can lead to significant morphological shifts—such as facet reconstruction, growth redirection, or internal structural modulation. A wide range of morphologies, including straight [60], zig-zag [61], kinked [62], branched [61], helical [63], or even hybrid structures with embedded nanoparticles [52], [64], [65] have been reported in oxide nanowires.

Due to the low solubility of oxygen in common seed materials, oxide nanowire growth is highly sensitive to local variations in supersaturation in seeds (including oxygen content, precursor flux), wetting angle at vapor–seed–nanowire interfaces, nanowire size, and surface/interface energies. These fluctuations can alter the supersaturation and surface energy balance at the TPB, promoting directional changes or facet transitions. Additionally, crystallographic defects like stacking faults and twins can further drive morphological changes by modifying local strain, growth fronts, or interface stability. The influence of such defects has been used to successfully predict the emergence of features like sawtooth edges [34], [35] and kinks [36]. Additionally. Tuning growth conditions during vapor-phase synthesis can induce morphological instabilities in oxide nanowires, leading to the in-situ formation of embedded Au nanoparticles, known as nanopeapods. This process is often driven by variations in supersaturation, gas-phase chemistry, or thermal fluctuations.

The following sections will examine two key in-growth morphology transformations—kinking and nanopeapod formation—in greater detail.

2.3.1. Kinking

Kinking in nanowires refers to a sharp change in growth direction, often resulting in zigzag or angled morphologies as shown in Figure 2-8. Kinked nanowires offer unique advantages for nanoelectronics and sensing. Their geometry enables flexible mechanical behavior [66], [66], [67], precise junction formation for transistors and diodes [68], [69], [70], and enhanced 3D interfacing for biosensing and intracellular recording [71], [72], [73], making them valuable for advanced device applications. Kinking is typically associated with changes in growth conditions, heterostructure interfaces, or the presence of planar defects such as stacking faults and twins. These local disruptions alter the growth front's energetics or symmetry, triggering a redirection of nanowire elongation. While kinking has been extensively studied in III–V and group IV systems, several oxide nanowire systems have also shown kinked morphologies under specific conditions.

One prominent example is found in Sb-doped ZnO nanowires, where Zhang et al. observed kinking angles of approximately 57°, 70°, and 117°, which were attributed to the formation of $\{0\bar{1}11\}$ and $\{0\bar{1}13\}$ twin planes and stacking faults. Sb segregation at these defect sites modified the local stress distribution and growth energetics, promoting redirection at the triple-phase boundary (TPB) [74]. In Zn_2SnO_4 nanowires, periodic sawtooth-like kinks formed due to structural transitions triggered by changes in cross-sectional shape at elevated temperatures. This morphological evolution distorted the seed droplet geometry, repeatedly shifting the TPB and causing directional changes during growth [75].

Other reports include kinked In_2O_3 nanowires synthesized via a tube-in-tube laser ablation CVD method, where changes in the inner tube geometry modulated vapor concentration and supersaturation. These conditions led to periodic directional changes and the formation of multikinked morphologies without externally pulsing the precursor flow [69]. In a separate study, Shen et al. [76] showed that growth direction in In_2O_3 nanowires could also switch spontaneously from $\langle 111\rangle$ to $\langle 110\rangle$ or $\langle 112\rangle$ once the Au seed diameter decreased below ~100 nm, driven by a size-dependent transition in interfacial free energy under constant growth conditions. In β-Ga_2O_3 nanorods, periodic kinks were attributed to twin-plane formation at the Au-assisted growth front under low oxygen partial pressure, which repeatedly altered the elongation direction [77]. Similarly, in SnO_2 microwires and nanobelts, sequential $\{101\}/\{\bar{1}01\}$ twin boundaries repeatedly rotate the growth axis by $\approx 68^{\circ}$, yielding periodic double- and triple-kink zig-zag geometries [78], [79].

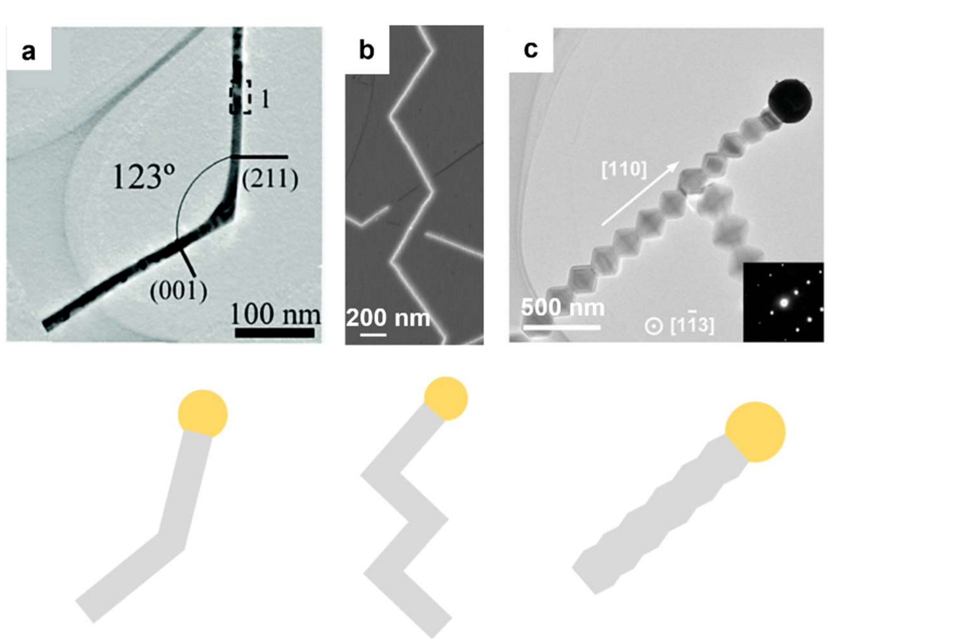

Figure 2-8. TEM micrographs and schemes of various nanowire morphologies with single (a) or multiple kinks, including zigzag (b) and sawtooth (c) shapes. (a) Single kinked SnO_2 nanowire (adapted with permission from [79]). (b) Zigzag In_2O_3 nanowire (adapted with permission from [69]). (c) Sawtooth TiO_2 nanowire (adapted with permission from [15]).

2.3.2. Nanopeapods

The 1D hybrid nanosystems, composed of nanoparticle chains embedded within nanowires or nanotubes, shown in Figure 2-9—referred to as nanopeapods—have attracted considerable attention due to their unique physical and chemical properties, including nonlinear fast optical responses [80], [81], [82] and high stability during lithium insertion/extraction in the lithium-ion batteries [83]. However, only a limited number of nanopeapod systems have been successfully fabricated, each with system-specific assembly methods. Most fabrication methods involve a two-step process: initially synthesizing core-shell nanowires or layered nanostructures, followed by the transformation of internal nanowires into nanoparticles through Rayleigh instability triggered by thermal annealing [84], [85], [86], [87] or plasma processing [82]. Notably, incorporating nanoparticles directly during nanowire growth simplifies synthesis routes and can be seamlessly integrated into established nanowire synthesis methods, providing further insights into these widely utilized techniques.

An intriguing aspect of Au nanopeapods growth is that This phenomenon has been observed in Au-assisted growth of various oxide systems, including SiO_2 [88], [89], [90], Ga_2O_3 [64], MgO [65], Al_2O_3 [91], and $CoAl_2O_4$ [92], or in scenarios where oxygen is incorporated during growth—like the synthesis of silicon nanowires using silicon monoxide (SiO) via the VLS mechanism [88], [93]. Previous studies generally attributed the emergence of Au nanoparticles within nanowires to growth instabilities involving oxygen. Low solubility in Au results in varying growth rates at the nanowire-seed interfaces, with the central region growing more slowly than the perimeter, leading to the sinking of Au nanoparticles within oxide nanowires. However, the vapor-phase growth of oxide nanowires, such as MgO, ZnO, SnO_2, TiO_2 [48], [94], appears to be favored within optimized flux ranges of growth species, with no Au nanopeapod observed within all tested flux ranges.

The presence of Au nanopeapods, particularly within SiO_2 nanowires [89], [90] often coincides with an oscillating morphology characterized by periodic structures. The link between these periodic structures and nanopeapods formation has been attributed to factors such as the roughening transition at the LS interface [95], the area of the liquid–solid interface [96], and the surface curvature oscillations of the liquid seed [97]. Conversely, similar periodic structures, resulting from the interplay of the geometry and surface energies of the nanowire and seeds, have also been observed in TiO_2 [15], [30], Ga_2O_3 [98], Zn_2SnO_4 [75], yet without nanopeapods formation. While factors such as oxygen-induced instabilities and periodic morphological fluctuations have been proposed to explain nanopeapod formation during vapor-phase nanowire growth, a lack of essential details—such as localized growth rates and precise formation conditions—hinders a comprehensive understanding of the process. Notably, the epitaxial interface, between solid nanoparticles (e.g., $NiSi_2$) within a liquid Au seed and the Si nanowire, can play a critical role in incorporating solid particles into nanowires [99].

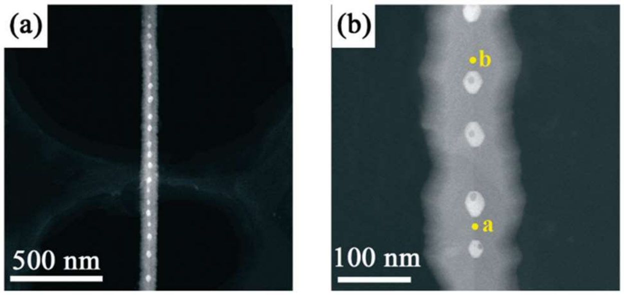

Figure 2-9. (a) Low-magnification HAADF-TEM image of an Au-in-Ga_2O_3 peapod nanowire with Au particles along the twin boundary; (b) magnified view. Adapted with permission from [64].

2.4. Target System: TiO_2 Nanowires

2.4.1. The Importance of TiO_2 Rutile Nanowires

Titanium dioxide (TiO_2) exists primarily in three polymorphs: anatase, rutile, and brookite. Among these, rutile is the most thermodynamically stable and belongs to the tetragonal crystal system with space group $P4_2/mnm$. The lattice parameters used here are a = 4.594 Å and c = 2.959 Å [100]. In rutile, each Ti atom is coordinated by six oxygen atoms in an octahedral configuration. The surface energies of low-index rutile planes decrease in the order (001) > (101) > (100) > (110), with the (110) surface being the most stable. Experimental values for the (110) surface energy range from 0.28 to 0.38 J/m^2, while theoretical estimates may be higher due to the influence of lattice relaxation effects [101], [102], [103].

Rutile TiO_2 nanowires are of great interest due to their unique combination of a wide bandgap semiconductor ($\approx$3.0 eV) and a high surface-area one-dimensional structure. This makes them ideal for several advanced applications. In gas sensing, individual rutile TiO_2 nanowires have demonstrated high sensitivity to gases like CO, H_2, and O_2 at low concentrations, with enhanced performance under visible light due to surface photoactivation effects [104] . For photocatalysis and solar energy conversion, vertically aligned rutile nanowires arrays act as efficient photoanodes, enabling high photocurrents ($\sim$7 mA cm^{-2}) during water splitting while maintaining structural stability [105]. In optoelectronics, TiO_2 nanowire/Si heterojunctions have been used to fabricate broadband photodetectors with high responsivity ($>10^4$ A/W) and fast response times, benefiting from the nanowires' fast charge collection pathways [106]. Additionally, rutile nanowires serve as robust anodes for lithium-ion batteries, showing high-rate capability ($\sim$130 mAh g^{-1} at 50 °C) and excellent cycling stability due to their direct electron pathways and ability to accommodate fast lithium-ion transport without cracking [107]. These diverse applications highlight the importance of rutile TiO_2 nanowires in high-performance sensors, energy devices, and electronics.

2.4.2. TiO_2 Nanowires Grown by Conventional Methods

Various methods have been developed to synthesize TiO_2 nanowires, each with different levels of control over morphology, phase, and alignment. Vapor-phase approaches, including thermal evaporation and chemical vapor deposition (CVD), have been widely applied but often face limitations in achieving long, uniform, and well-aligned rutile TiO_2 nanowires. For instance, Shi et al. [12] used a pulsed CVD process alternating $TiCl_4$ and H_2O to grow TiO_2 nanowires on Au-coated substrates at 600–650 °C. However, the resulting nanowires were short and exhibited irregular orientations, heavily influenced by purging time and surface conditions. Ramezani Sani et al. [13] synthesized nanowires via two-step thermal evaporation on Au-coated Ti/Si substrates. Their results showed that reducing Ar flow raised the oxygen partial pressure, favoring the VS growth and suppressing the formation of eutectic Au–Ti alloys, while higher Ar flow introduced oxygen vacancies that disrupted nanowire morphology. Similarly, Shang et al. [14] observed that Ti substrate oxidation and phase transitions near 900 °C significantly affected atomic diffusion and growth direction, often resulting in short, tapered structures. Despite these efforts, none of these methods consistently produced long, vertically aligned TiO_2 nanowires.

Beyond vapor-phase techniques, various liquid-phase approaches—particularly hydrothermal synthesis—have also been explored for growing TiO_2 nanowires. For example, Liu and Aydil [108] demonstrated the growth of rutile TiO_2 nanorods (~2 μm) on fluorine-doped tin oxide (FTO) substrates by reacting $TiCl_4$ in hydrochloric acid at 150–180 °C, achieving vertical alignment and high aspect ratios. Jiu et al. [109] synthesized anatase TiO_2 nanorods (~300 nm) by hydrothermal treatment of titanium butoxide in ethanol–water mixtures, enabling transparent films for solar cell applications. Miao et al. [110] used a template-assisted sol-gel route, electrochemically depositing Ti precursors into anodic aluminum oxide (AAO) membranes, followed by heat treatment to yield single-crystal anatase nanowires.

Solution-based methods offer low-cost and low-temperature processing but typically yield anatase TiO_2 with poor alignment control. Vapor-phase techniques better support rutile formation and integration but struggle with uniformity. Thus, improved strategies are needed to combine the precision of vapor growth with the tunability of solution methods for high-quality rutile TiO_2 nanowires in advanced applications.

2.4.3. TiO_2 Nanowires Grown by VAdS Method

A recently developed vapor–adsorbate–solid (VAdS) growth mechanism offers a new approach to synthesizing high-quality TiO_2 nanowires. This method eliminates the need for conventional vapor–liquid–solid (VLS) components such as external precursor flux, carrier gas, and imposed temperature gradients. Instead, it relies on a sealed configuration where a single-crystal TiO_2 substrate serves both as the vapor source and the growth platform. The system is heated uniformly to 1000 °C under an argon atmosphere, creating stable, isothermal conditions within a quartz tube. These simplified parameters provide excellent control over the growth process, enabling the formation of uniform, single-crystalline nanowires with well-defined shapes and lengths extending up to tens of microns [15].

Although no external precursor is introduced in the VAdS method, a small amount of TiO_x vapor is generated from the substrate itself through equilibrium decomposition at high temperature. Unlike conventional VLS or VS growth, which rely on carefully tuned external fluxes within a narrow material flux window, the VAdS method operates under extremely low, self-regulated vapor conditions in a sealed and isothermal environment. This places it outside the traditional VLS–VS regime, both in terms of flux control and growth mechanism. Nanowire formation is believed to proceed through surface-mediated processes: a thin TiO_x layer forms around the catalytic seed, reducing surface energy and enhancing the adsorption and surface diffusion of vapor species toward the growth front. This distinct, adsorption-driven pathway may account for the robust and uniform nanowire growth observed under conditions where conventional vapor-phase methods often fail.

Importantly, the chemical composition of the seed plays a critical role in determining the resulting nanowire morphology. Two distinct morphologies have been observed: bead-like nanowires typically form when pure Au seeds are used, while prismatic nanowires emerge when Au–Ag bimetallic seeds are employed. The introduction of Ag appears to modify the growth direction, promoting a transition from $\langle 110\rangle_{TiO_2}$ to $\langle 111\rangle_{TiO_2}$ as shown in Figure Figure 2-10. This effect is attributed to the formation of Ag-rich segregations at the seed-nanowire interface, which may interact differently with the TiO_2 lattice during nucleation. Although the underlying mechanism remains under investigation, this observation highlights the potential of seed engineering as a means to tailor nanowire geometry and crystallographic orientation.

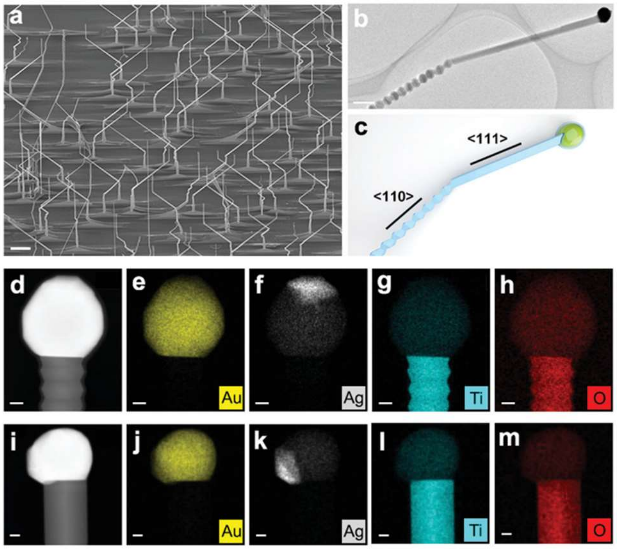

Figure 2-10. Morphological and compositional analysis of twisted TiO_2 nanowires synthesized using the VAdS method with Au–Ag bimetallic seeds. (a) Tilted-view SEM image. (b) TEM image of a twisted nanowire. (c) 3D model corresponding to image (b). (d) HAADF image of a bead-like nanowire with corresponding EDX elemental maps for (e–h) Au, Ag, Ti, and O. (i–m) HAADF image and EDX elemental maps showing Au, Ag, Ti, and O distributions in a prismatic nanowire. Scale bars: 1 µm (a), 500 nm (b), 50 nm (d–m). Adapted with permission from [15].

2.5. Research Objectives

1. Refine the recently developed “vapor-adsorbate-solid” synthesis method to produce uniform, well-defined TiO_2 nanowires by optimizing oxygen partial pressure.
2. Enable morphology control of nanowires by tuning the seed composition, focusing on Au–Ag and Au–Ni bimetallic seeds.
3. Perform crystallographic and spectroscopic analysis of Au- TiO_2 interfaces to clarify the mechanism behind morphology changes.

2.6. Critical Comments

The VAdS growth method has demonstrated strong potential in producing long, uniform, single-crystalline TiO_2 nanowires by eliminating key variables such as external material flux, temperature gradients, and carrier gas flow. However, several aspects of this mechanism remain insufficiently understood and present important directions for future research. Unlike VLS-like systems, where nanowire formation occurs within a narrow and well-defined material flux window balancing VLS and VS modes, the VAdS approach operates outside—or at the extreme low end—of this window. As a result, the traditional flux-based criteria for nanowire growth are no longer applicable under VAdS conditions.

Although external fluxes are absent in this closed system, residual oxygen can still vary in the growth environment. These subtle changes in oxygen partial pressure may influence the growth process and introduce reproducibility challenges, effectively acting as an internal material flux. Given that the VAdS mechanism fundamentally deviates from classical VLS theory, identifying the role and optimal range of oxygen partial pressure is essential for achieving consistent and controlled nanowire synthesis.

In terms of morphology control, introducing Au–Ag bimetallic seeds instead of pure Au has led to a clear shift in both growth direction—from $\langle 110 \rangle_{TiO_2}$ to $\langle 111 \rangle_{TiO_2}$—and nanowire shape, changing from bead-like to prismatic structures. This transition is accompanied by Ag segregation, suggesting a strong link between seed composition and nanowire geometry. However, the exact mechanism driving this transformation remains unclear. Further studies are needed to understand how variations in seed composition, including other potential alloying elements, influence nucleation behavior, interfacial interactions, and nanowire morphology.

2.7. Potential Applications and Importance of Morphology Control

Controlling the morphology of TiO_2 nanowires—specifically transitioning between bead-like, prismatic, kinked, and nanopeapod architectures—provides a powerful route to engineer their optical, electronic, and catalytic behaviour. These morphologies differ not only in geometry but also in symmetry, periodicity, and local curvature, all of which strongly influence anisotropic responses to light, electric fields, and surface reactions [111]. The ability to deliberately tune morphology, therefore has direct implications for advanced device applications.

Bead-like nanowires possess low-symmetry, quasi-periodic modulations along their length. Such periodic diameter variations create refractive-index contrast, enabling axial optical scattering and confinement similar to one-dimensional photonic crystals, where periodicity governs light propagation and bandgap formation [112]. In contrast, prismatic nanowires maintain a high-symmetry faceted cross-section, promoting directionally consistent charge transport and predictable optical absorption—properties valuable for photodetectors, photocatalysis, and electronic scaffolds [113].

Kinked nanowires introduce abrupt directional changes that function as built-in junctions or scattering nodes, enabling wavelength- or position-selective photodetection [114]. Nanopeapods, with periodic nanoparticles encapsulated inside a single NW, enable ultrafast all-optical switching and hybrid plasmonic–photonic coupling [115]. By demonstrating controlled transitions between bead-like and prismatic morphologies, and by revealing how seed composition drives these symmetries, this work links morphological control directly to anisotropy engineering, providing a materials-level pathway for designing nanowires with tailored optical and electronic behaviour.

Chapter 3

Experiment Design and Techniques

This chapter presents the experimental framework and characterization techniques employed in this study. Section 3.1 explains the nanowire synthesis procedure, including substrate preparation, cleaning, and nanoparticle deposition for Au, Au–Ag, and Au–Ni systems. Section 3.2 introduces our customized experimental setup and improvements for nanowire growth. Section 3.3 discusses the nanowire characterization, highlighting the tips for Scanning Electron Microscopy (SEM) and Transmission Electron Microscopy (TEM). Section 3.4 covers the X-ray Absorption Spectroscopy (XAS) experiments, highlighting our tailored setup and outlining the data analysis approach.

3.1. Nanowire Synthesis Overview

The TiO_2 nanowire synthesis strategy involved three different types of seed particles—Au–Ni (via sputtering), colloidal Au, and colloidal Au–Ag—all tested under varying growth conditions. The seed preparation methods, pressure control during sealing, and tube design were progressively optimized throughout this study to achieve more consistent and controlled nanowire growth. A detailed discussion of the experimental design, challenges encountered, and improvements implemented is provided in the following section (section 3.2).

All nanowire syntheses were carried out on single-crystal rutile TiO_2 substrates with (110) surface termination, which were cut and ultrasonically cleaned before seed deposition. Additional information on substrate preparation and cleaning can be found in Appendix A (sections A.1 and A.2).

The first seed type, Au–Ni, was unintentionally induced during Au sputtering followed by a pre-heating at 400 °C for 1 hour, where subsequent analysis revealed the presence of Ni. This alloying led to random bead-like and prismatic nanowires with embedded nanoparticles and was later studied systematically as a bimetallic seed. Details of the sputtering process and nanoparticle formation are provided in Appendix A (section A.3).

To eliminate contamination and better control seed purity, colloidal Au nanoparticles (20 nm, PBS-stabilized) were introduced. These were cleaned through centrifugation and plasma-treated before nanowire synthesis. Although some morphological irregularities remained—likely due to stabilizer residues—this method provided purer Au seeds than sputtering. To further tailor the seed composition, Au–Ag bimetallic nanoparticles were prepared by mixing separately purified Au and Ag colloidal suspensions in a 60:40 volume ratio. After cleaning, the mixture was deposited onto the substrates and plasma-treated under the same conditions as for pure Au. Refer to Appendix A (sections A.4 and A.5) for additional details on colloidal nanoparticle formation.

After seed deposition, each sample was sealed in a quartz tube under a controlled Ar environment. The Ar pressure during sealing was varied in a series of trials, ranging from near-atmospheric pressure (∼93 kPa) down to ∼0.4 Pa. The sealed tubes were then subjected to thermal treatment at 1000 °C for 1 hour to enable nanowire growth. Details on the tube sealing process and heat treatment are provided in Appendix A (section A.6). The resulting morphologies were analyzed and are discussed in Chapter 4. A schematic summarizing the growth process using different seed types is shown in Figure 3-1.

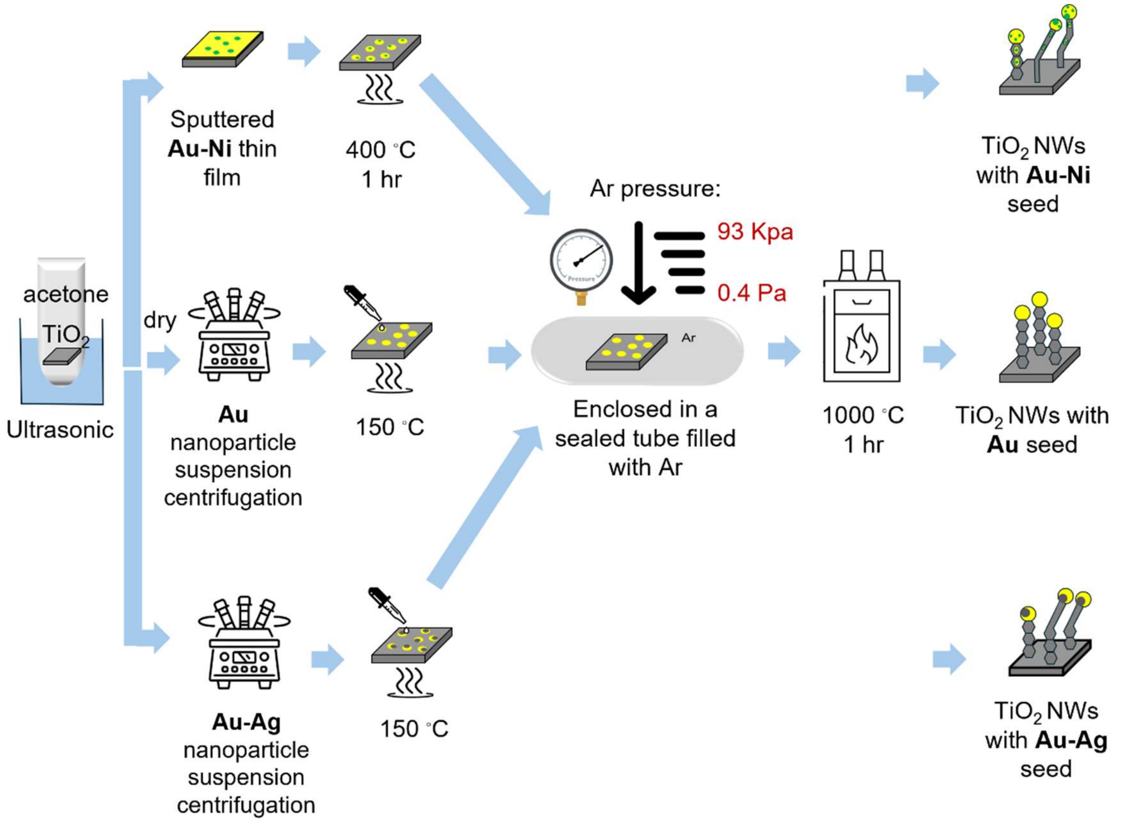

Figure 3-1. Nanowire synthesis setup for growing nanowires with various morphologies using Au, Au–Ag, and Au–Ni seeds by regulating Ar pressure from 93 kPa to 0.4 Pa.

3.2. Experimental Design and Improvements

The development of the TiO_2 nanowire synthesis protocol required significant design adjustments to the experimental setup, especially in response to early-stage issues with sealing, pressure control, and seed material purity. This section outlines the key challenges encountered and the corresponding improvements implemented throughout the study. Full procedural details and additional data are provided in Appendix A.

3.2.1. Sealing Plug Geometry and Pressure Regulation

The initial design of the sealing plug presented significant issues. It had a cylindrical shape with a circular cross-section, which allowed it to fit tightly against the inner wall of the quartz tube. This contact often caused the plug to stick and block the gas flow, thereby preventing proper pressure regulation above and below the plug—both critical regions for Ar refilling and sample stability. Additionally, during flame sealing, the elevated internal pressure expanded under high temperature and pushed the plug outward, frequently leading to sealing failure.

To fix this issue, a small cut was made on the edge of the sealing plug as shown in Figure 3-2(b). This helped the gas move more easily and stopped the plug from blocking the flow during air evacuation and Ar refilling. We also tapped the tube near the plug and waited a few minutes before sealing to let the pressure inside the tube stabilize. Additionally, we purchased new quartz tubes with increased wall thickness and a pre-manufactured notch at the mid-length to securely hold the sealing plug as shown in Figure 3-2(a). These new tubes eliminated the need for manual notching using flame melting, provided a more precise fit for the plug, and, due to their thicker walls, were more resistant to thermal stress during flame sealing—significantly reducing the risk of sealing failure.

Figure 3-3(a) presents nanowires grown using the original plug design, while Figure 3-3(b) shows the results with the notched, custom plug. The latter clearly improved nanowire base formation, suggesting that the customized plug geometry—by facilitating better airflow and enabling more effective vacuum conditions during Ar refilling and sealing—contributes positively to the nanowire growth.

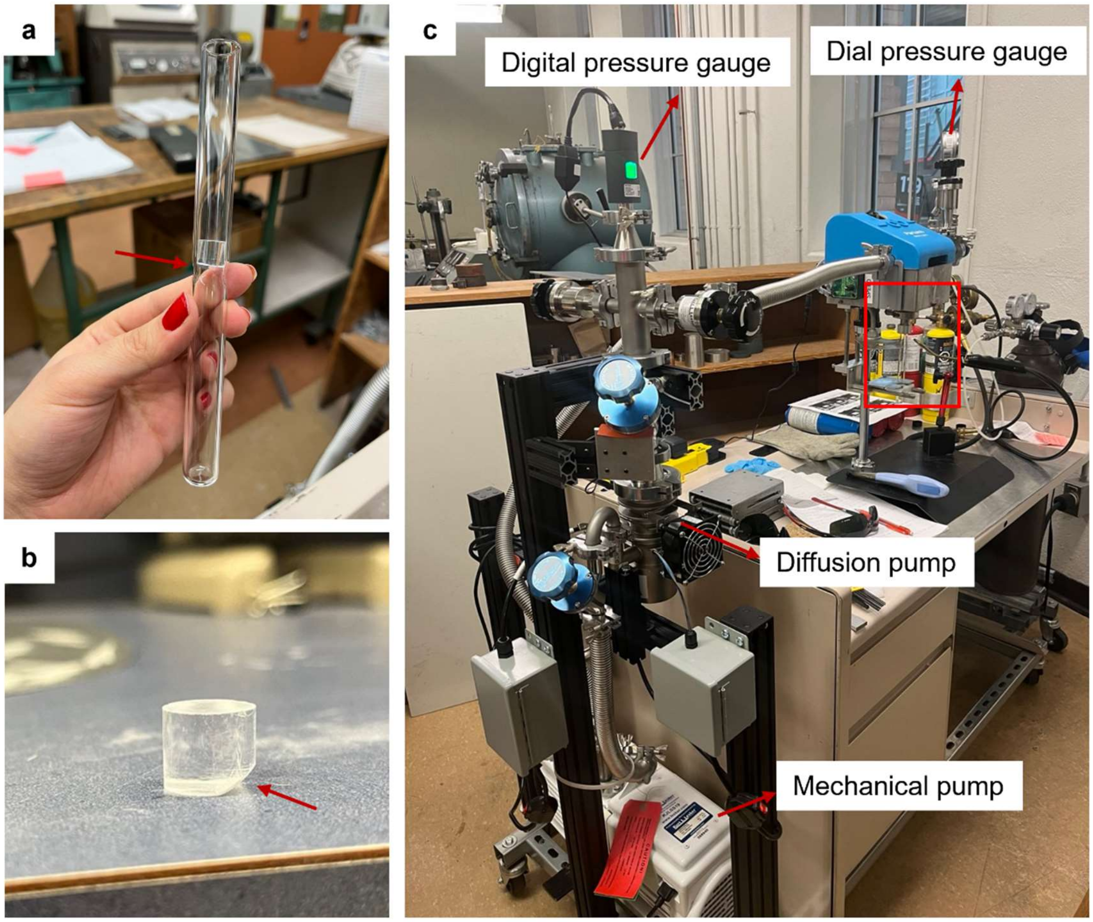

Figure 3-2. Tube sealing setup: (a) Custom-designed quartz tube featuring a narrowed section at the midpoint (indicated by a red arrow). (b) Sealing plug with a corner notch to prevent sticking and ensure proper gas flow during argon filling. (c) Sealing and argon-filling system, showing the quartz tube (highlighted with a red rectangle), mechanical and diffusion pumps, and both dial and digital pressure gauges.

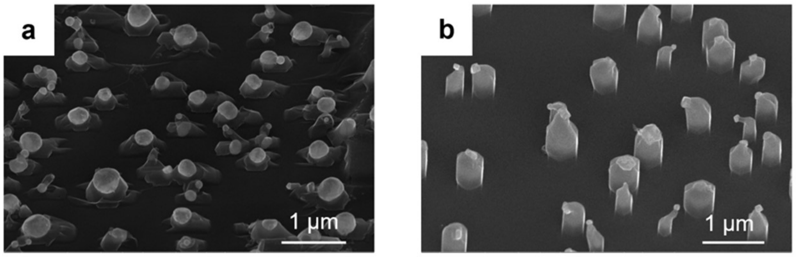

Figure 3-3. SEM images of TiO_2 nanowires grown using (a) the original cylindrical plug and (b) the custom notched plug, which facilitated more efficient gas flow and improved vacuum conditions during sealing.

3.2.2. Pressure Monitoring

Initially, system pressure was monitored solely using a dial pressure gauge as shown in Figure 3-2(c), but it lacked the precision necessary to accurately track low oxygen and Ar pressures. This issue was addressed by installing a Pirani-capacitance diaphragm digital gauge, with a measurement range of 0.005 Pa to 150,000 Pa and an accuracy of 2.5% to 10% depending on the pressure, illustrated in Figure 3-2(c). This upgrade, implemented with the help of Mr. Paul Krueger, greatly improved the reliability of pressure readings during growth.

3.2.3. Residual Oxygen and Pressure Optimization

In early efforts to minimize oxygen content, the system was subjected to repeated Ar refilling cycles (up to 60 times) at 93 kPa to dilute residual air. However, nanowire growth did not improve significantly (Figure 3-4), and further analysis confirmed that most of the residual oxygen originated not from trapped air but from the 0.003% impurity in the high-purity (99.997%) Ar gas, which included about 10 ppm O_2. For example, four Ar refilling cycles left only $\sim 4 \times 10^{-17}$ Pa of residual air oxygen, while Ar gas impurity contributed ~1 Pa of oxygen. Table 3-1 shows the estimated O_2 partial pressure after each refilling times.

Table 3-1. Estimated oxygen partial pressure after each Ar refilling cycle, accounting for contributions from both residual air (assumed 20% O_2) and Ar gas impurity (0.01%).

Refilling times	Vacuumized		Refilled			
	P_{Air} / Pa	P_{O_2}	P_{Ar}/ Pa	Ar impurity (0.003%)/ Pa	O_2 as Ar impurity (around 10 ppm)/ Pa	O_2 partial pressure/ Pa
Cycle 1	0.453	0.09078	101324.55	3.040	1.013	1.104
Cycle 4	4.08E-17	8.16E-18	101325	3.040	1.013	1.013

Cycle 10	3.29E-49	6.59E-50	101325	3.040	1.013	1.013
Cycle 20	1.07E-102	2.14E-103	101325	3.040	1.013	1.013
Cycle 30	3.49E-156	6.98E-157	101325	3.040	1.013	1.013
Cycle 50	3.69E-263	7.39E-264	101325	3.040	1.013	1.013
Cycle 60	0	0	101325	3.040	1.013	1.013

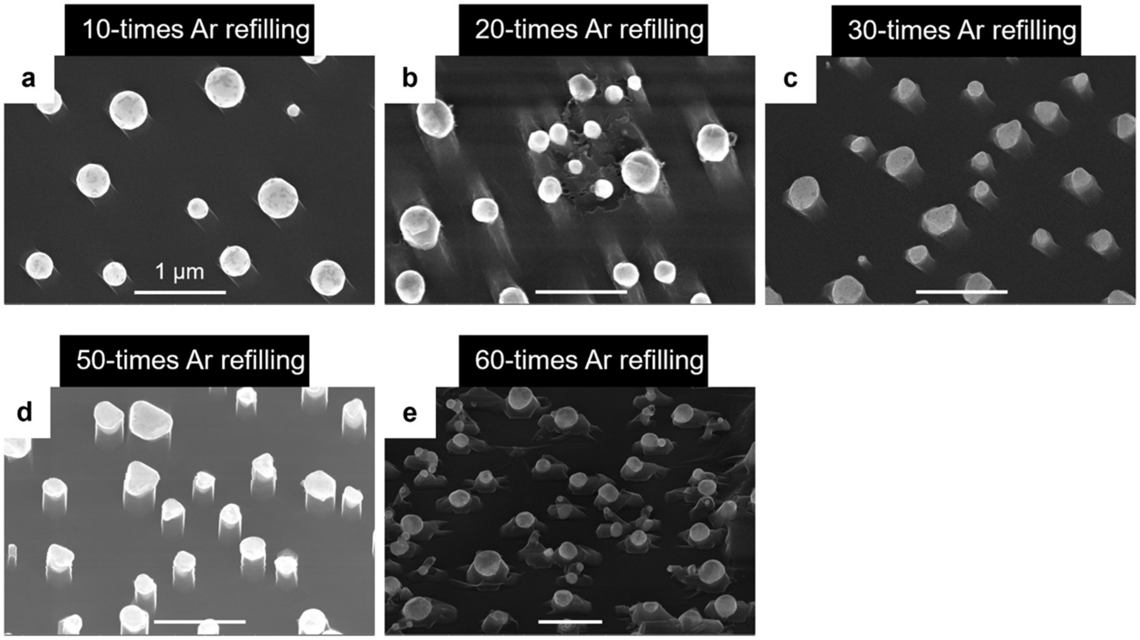

Figure 3-4. SEM images taken at a 20° tilt showing Au nanoparticles formed by sputtering on TiO_2 nanowires and after varying Ar refilling repetitions, all sealed at 93 kPa: (a) 10 refills, (b) 20 refills, (c) 30 refills, (d) 50 refills, and (e) 60 refills.

To better address this, the sealing pressure itself was reduced in a stepwise fashion—from atmospheric pressure (933 kPa) down to 0.453 Pa—using a mechanical pump (with a base vacuum of approximately 2×10^{-3} Torr). Later, a diffusion pump capable of reaching $\sim 10^{-7}$ Torr was installed (shown in Figure 3-2(c)) to access a higher vacuum during the refilling process and reach a lower pressure. It is important to note that the digital gauge had a lower detection limit of 7×10^{-5} Torr, meaning it could not display values below this threshold during diffusion pumping. Gradual pressure reduction helped ensure safe sealing without tube failure, while improving the nanowire growth environment. A summary of the sealing pressures and oxygen estimations is provided in Table 3-2.

Table 3-2. Summary of sealing pressures and the corresponding estimated oxygen partial pressures after four cycles of Ar refilling.

P_{Ar}/ Pa	Ar impurity/ Pa	O_2 as Ar impurity (around 10 ppm)/ Pa	O_2 partial pressure/ Pa
93325	2.800	0.933	0.933
79193	2.376	0.792	0.792
66394	1.992	0.664	0.664
51862	1.556	0.519	0.519
32664	0.980	0.327	0.327
17199	0.516	0.172	0.172
8026	0.241	0.080	0.080
2000	0.060	0.020	0.020
933	0.028	0.009	0.009
159	0.005	0.002	0.002
23	0.001	2.27E-04	2.27E-04
11	0.000	1.13E-04	1.13E-04
0.4	0.000	4.00E-06	4.00E-06

Figure 3-5 shows how reducing the sealing pressure influenced nanowire formation. As the pressure decreased from 93 kPa to 18 kPa, nanowire growth improved—likely due to a reduction in oxygen partial pressure. However, the overall density of nanowires remained low, possibly because some of the nanoparticles exceeded 100 nm in size and were unable to initiate growth.

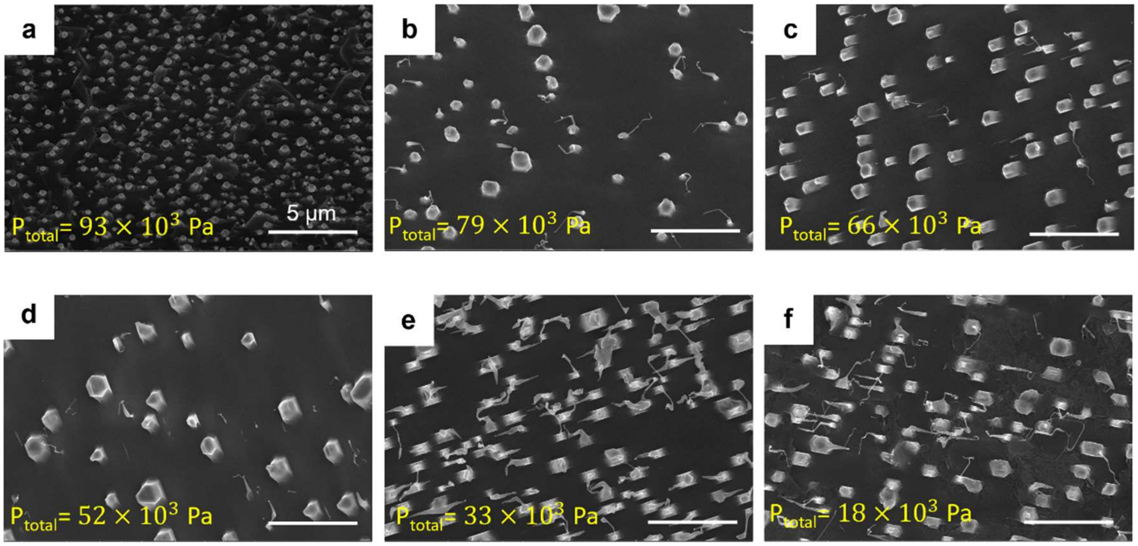

Figure 3-5. Nanoparticle formation and initial nanowire growth after four Ar refilling cycles, followed by synthesis under varying Ar sealing pressures: (a) 93 kPa, (b) 79 kPa, (c) 66 kPa, (d) 52 kPa, (e) 33 kPa, (f) 18 kPa.

3.2.4. Optimization of Nanoparticle Size

To reduce nanoparticle size, the sputtering time was progressively decreased from 30 seconds (Figure 3-4) to 5 seconds (Figure 3-6(a)), and finally to 2 seconds (Figure 3-6(b))—the minimum duration permitted by the system. The 2-second sputtering produced a film thickness of approximately 12 nm and yielded nanoparticles with an average size of ~35 nm. This condition led to a higher yield of nanowires and reduced the number of particles too large to initiate growth as shown in Figure 3-6(a) and (b). Therefore, it was selected as the optimal sputtering setting for nanowire synthesis. Additional details on the sputtering parameters and Au target specifications are provided in Appendix A, section A.3.

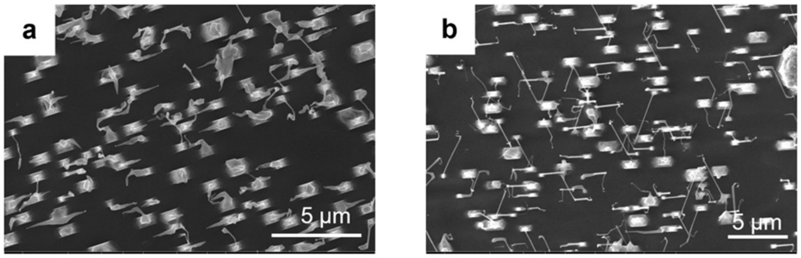

Figure 3-6. SEM images of TiO_2 nanowires synthesized at 33 kPa Ar pressure after four cycles of Ar refilling, using nanoparticles formed by sputtering for (a) 5 seconds and (b) 2 seconds.

3.2.5. Nanoparticle Purity and Morphology Control

Initial experiments with sputtered Au films consistently resulted in randomly kinked nanowires. It was turned out that Ni was accidently induced during Au deposition (See details in Chapter 4 and 5). Several potential sources of Ni were considered, including the substrate, quartz tube, sealing plug, sputtering system, pre-heating step, and heat-treatment process.

After confirming that the substrates, tubes, and plugs were thoroughly cleaned, we tested the influence of the pre-heating step by conducting nanowire synthesis both with and without this step. In both cases, kinked nanowires with embedded particles were still observed (see **Error! Reference source not found.**), indicating that pre-heating was not the source of contamination. Additionally, the sealing and heat-treatment processes were ruled out as potential sources, since nanowires synthesized using colloidal Au nanoparticles—under identical sealing and annealing conditions—exhibited vertically aligned, well-formed morphologies (as discussed in the following paragraph). This led us to suspect the sputtering system as the likely source of Ni contamination. Since the machine was shared with other users and had previously been used for Ni deposition, cross-contamination from earlier work appears to be the most plausible explanation.

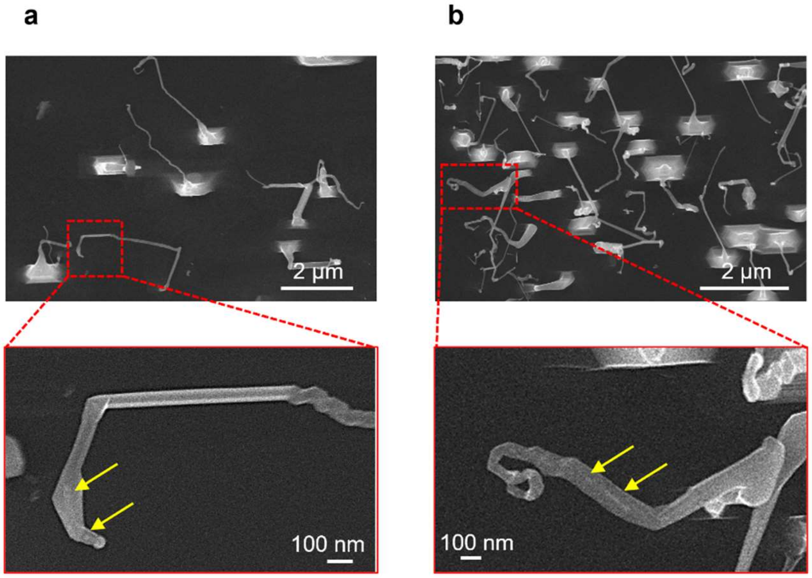

Figure 3-7. SEM images showing the effect of a 1-hour pre-heating step at 400 °C on nanowire growth under 600 Pa Ar pressure: (a) sample without pre-heating, where the sputtered Au film was directly subjected to heat-treatment for synthesis, and (b) sample with pre-heating applied to the sputtered Au film. Insets highlight magnified views of nanowires, with arrows indicating embedded nanoparticles.

To eliminate the issue of Ni contamination, colloidal Au nanoparticle suspensions were introduced as an alternative. However, these particles were stabilized in phosphate-buffered saline (PBS), which contains salts such as sodium chloride and potassium phosphate—potential contaminants that can lead to non-uniform and kinked nanowire growth, as shown in Figure 3-8(a). To reduce the effects of stabilizers, multiple rounds of centrifugation were performed to separate the salt-based additives, followed by plasma cleaning to remove hydrocarbon residues (detailed in Appendix A, sections A.4 and A.5). As shown in Figure 3-8b, the cleaning process led to somewhat improved nanowire morphology, though vertical alignment.

However, complete elimination of stabilizing agents was not achievable, and trace amounts likely remained in some cases. These residuals may have contributed to variations in growth, including slight kinking, reduced nanowire lengths, or inconsistent bead formation in part of the samples. These observations indicate that further refinement of the nanoparticle purification process is warranted to consistently obtain optimal nanowire morphology.

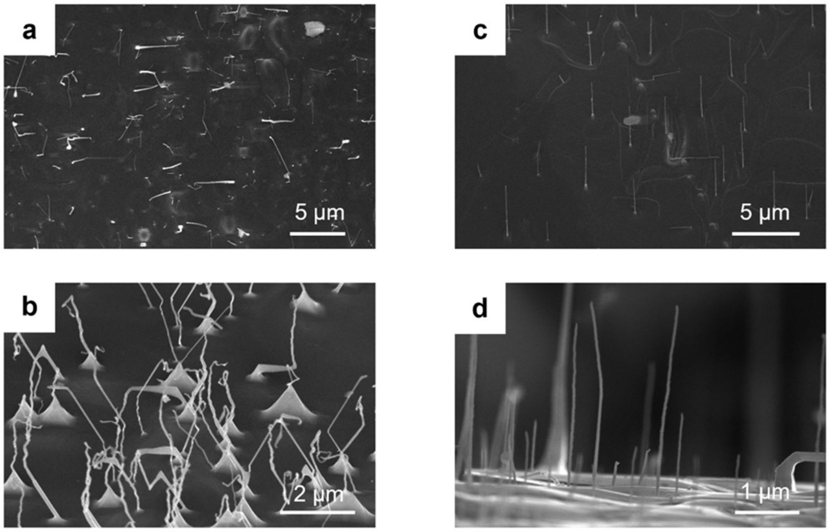

Figure 3-8. SEM images of TiO_2 nanowires synthesized using the Au nanoparticle suspension. (a) Inclined and (b) cross-sectional views of nanowires grown from Au nanoparticles stabilized with PBS. (c) Inclined and (d) cross-sectional views of nanowires formed after centrifugation and plasma cleaning to remove the stabilizing agent.

3.2.6. Systematic Introduction of Ni into the Growth System

To address the concern regarding the unintentional introduction of Ni, the role of Au nanoparticle stabilizing agents, and the reproducibility of the synthesis, we conducted the following experiments. We ordered and used 1.4 mg of stabilizer-free Au nanopowder (99.99%, 20 nm, SkySpring Nanomaterials Inc.), which was ultrasonic in 10 mL of distilled water and drop-cast onto a cleaned rutile substrate at ~150 °C. Since Ni nanopowder is highly flammable and incompatible with our current lab safety conditions, we instead used a $5 \times 7 \times 0.2$ mm Ni foil piece, sealed together with Au-deposited substrate during synthesis. As shown in Figure 3-9, the nanowires exhibited clear evidence of nanoparticle embedding, confirming the introduction of Ni and its role in the embedding process.

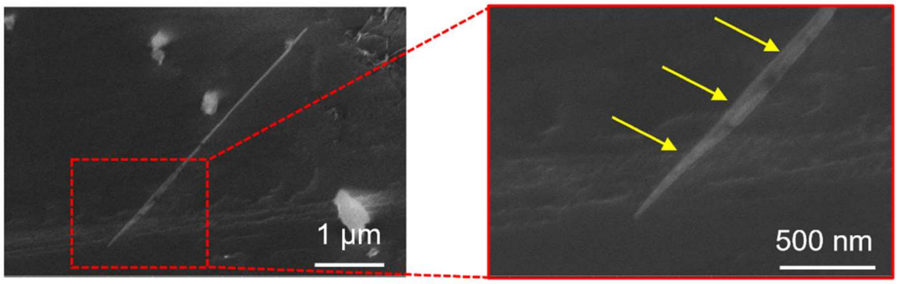

Figure 3-9. TiO_2 nanowires synthesized using stabilizer-free Au nanoparticles, with a Ni foil inside the sealed tube alongside the substrate. The magnified image on the right highlights signs of nanoparticle embedding, indicated by yellow arrows.

3.3. Microscopic Analysis (SEM & TEM)

The morphology and structure of TiO_2 nanowires were characterized using scanning electron microscopy (SEM) and transmission electron microscopy (TEM). SEM imaging was conducted using a field emission FEI Nova NanoSEM 450 at 10 keV to minimize charging and surface damage. Samples were imaged from multiple angles (top, inclined, and cross-sectional views) using a combination of Everhart-Thornley and through-lens detectors. For high-resolution structural and compositional analysis, TEM and high-resolution TEM (HRTEM) were performed using an FEI Talos F200X operating at 200 kV. This included elemental mapping via EDX, crystallographic characterization via SAED, and atomic-scale imaging of the Au–TiO_2 interface. For precise diffraction analysis, Kikuchi patterns were utilized to align nanowires with low-index zone axes. In practice, the nanowires were first adjusted close to an edge-on orientation (either along the side facets or at the nanowire–seed interface), ensuring that the facet normals were nearly perpendicular to the electron beam. The specimen was then tilted to a zone axis, verified in diffraction mode, and with a 10 µm SAED aperture, the diffraction pattern from the smallest possible area around the nanowire–seed region was recorded.

The resulting D-spacings and inter-spot angles were compared with rutile TiO_2 reference values to index the diffraction patterns. Since rutile TiO_2 has a tetragonal structure (a = b = 4.594 Å, c = 2.959 Å), Table 3-3 summarizes three common low-index facets along with their D-spacings and interplanar angles, provided as representative examples to avoid an overly long list. The diffraction spots represent facets perpendicular to the indexed family of planes. Figure 3-10 demonstrates how these spots were correlated with the identified facets for one prismatic nanowire as an example. Following the same system as in our previous work [59], [116], the top facet and side facets were identified as $\{110\}$ and $\{10\bar{1}\}$, respectively, highlighted in bold in the table, and confirmed in this analysis.

To identify additional facets, Kikuchi bands corresponding to side or top surfaces (depending on which were visible) were used as reference planes for moving between adjacent zone axes (see Kikuchi patterns in Figure 3-10 (1, 2, 3) and the common $\{110\}$

band). The Kikuchi band perpendicular to a diffraction spot (in this case {110}) corresponds to the family of planes being indexed.

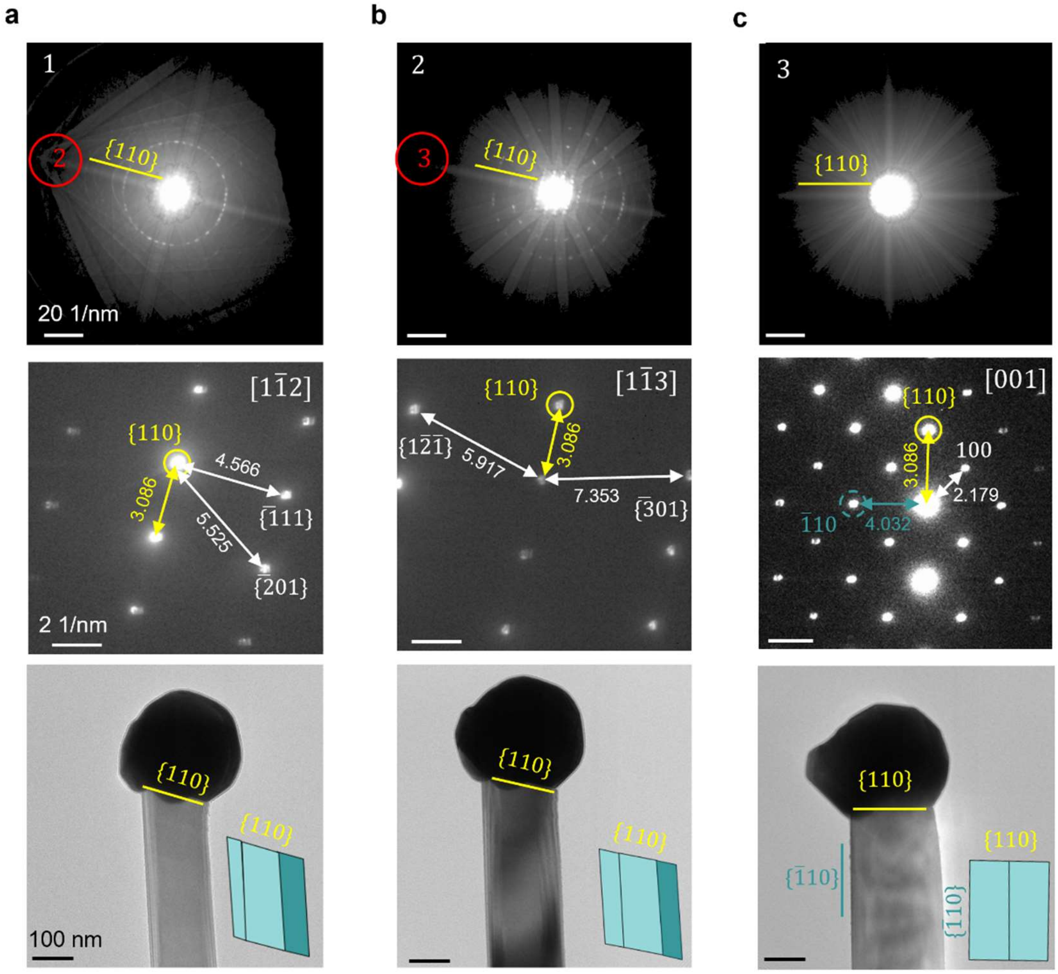

Figure 3-10. Illustration of the procedure for indexing diffraction patterns and facets, as well as tilting a prismatic nanowire as a representative example. Panels (1), (2), and (3) display three different Kikuchi patterns, each overlaid with its corresponding diffraction pattern. The common {110} plane in the diffraction pattern, which corresponds to the perpendicular band in the Kikuchi pattern, was used as a reference for tilting the sample toward adjacent low-index zone axes. In imaging mode (third row), the top facet {110} is indexed as being perpendicular to the diffraction spot associated with this family of planes. The nanowire was then tilted until a set of side facets, $\{1\bar{1}0\}$, were brought edge-on (beam perpendicular), as shown in the [001] zone axis. Insets are the three-dimensional (3D) schematics illustrating the side facets of nanowires, where $\{10\bar{1}\}_{TiO_2}$ and $\{1\bar{1}0\}_{TiO_2}$ side facets are labelled by light and dark blue, respectively. Yellow and cyan indices in the diffraction patterns indicate the top and side facets, respectively.

Table 3-3. D-spacings and interplanar angles of selected rutile TiO_2 low-index facets, used as reference values for indexing TEM diffraction patterns and identifying the corresponding zone axis.

Plane family	1/D (Å^{-1})	D (Å)	∠ {110} (°)	∠ {101} (°)	∠ {111} (°)
$\{\mathbf{110}\}$	0.308	3.249	0	67.489	47.674
$\{\mathbf{10\bar{1}}\}$	0.402	2.488	67.489	0	28.433
{111}	0.457	2.188	47.674	28.433	0

3.4. Spectroscopic Analysis (XAS)

3.4.1. Experimental Design

We used X-ray absorption spectroscopy (XAS) to probe the local atomic structure at the TiO_x–seed interface and assess how Au–Ag seed composition influences growth direction and morphology. The analysis included Extended X-ray Absorption Fine Structure (EXAFS) and X-ray Absorption Near Edge Structure (XANES) measurements, performed at the Ti K-edge, Au L_3-edge, and Ag K-edge using the Hard X-ray Micro-Analysis (HXMA) beamline at the Canadian Light Source (CLS). The fluorescence mode with a grazing angle was employed to detect Au and Ag in the seeds atop the nanowire grown on TiO_2 substrates. The rationale for selecting these specific elements and absorption edges, as well as the choice between fluorescence and transmission modes in XAS measurements, is discussed in detail in Appendix B, Section B1. The CLS storage ring operated at a current of 220 mA at top-up mode. Au and Ag foils were used for collecting referenced spectra to calibrate the monochromator energy.

The sample was fixed into a plastic holder using adhesive tape and mounted onto the experimental stage. Its height and position were manually adjusted to align with the incoming X-ray path. The angular alignment was calibrated to ensure the X-ray beam aligning with the seed region of the nanowire, approximately 10 µm above the substrate. Figure 3-11 shows (a) the schematic and (b) the actual setup, including the arrangement of the incident beam detector (I_0), fluorescence detector (I_f), transmission detector (I_1), the sample, Au foil used as a reference, and the transmitted beam detector for collecting the reference spectra (I_2). The grazing angle φ, representing the angles between the incident beam and the sample, is calibrated between 1° and 5°. At each angle, a two-dimensional (2D) mapping (as the inset) was carried out, and the sample was repositioned to maximize the detected signal. During the 2D mapping, the sample was moved horizontally (X-direction) and vertically (Z-direction), both perpendicular to the direction of the X-ray beam. The φ was optimized through 2D mapping measurements for five times to ensure the signals were collected specifically from the seed regions.

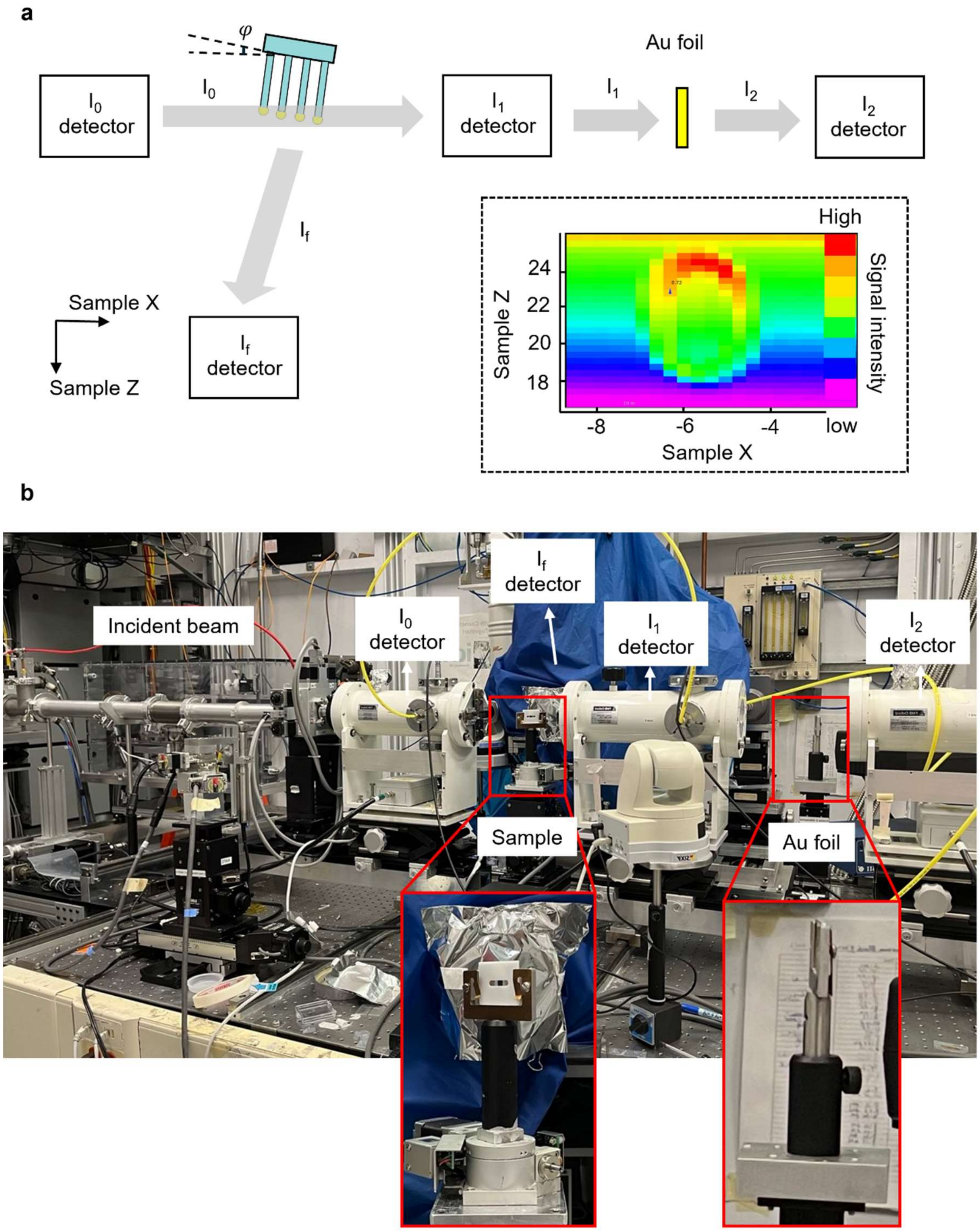

Figure 3-11. (a) Schematic and (b) the actual setup of the XAS experimental setup showing the arrangement of the incident beam detector (I_0), fluorescence detector (If), transmission detector (I_1), TiO_2 sample, Au foil reference, the transmitted beam detector after the Au foil (I_2), and the grazing angle φ as the angle between the incident beam and the sample surface. The inset color-gradient map illustrates 2D scanning, where the sample was moved horizontally (X-direction) and vertically

(Z-direction), both perpendicular to the X-ray beam. At each grazing angle φ (ranging from 1° to 5°), mapping was conducted, and the sample was then repositioned to align its center with the beam for maximized signal detection.

3.4.2. Data Analysis of XANES

The XANES data was analyzed using Athena [12] and Larch [13] platforms. To facilitate direct comparison with theoretical calculations and other experimental spectra, regardless of specific acquisition conditions, including sample thickness, sample concentration, monochromator responses, and detectors effect, the spectrum was normalized through low-order polynomial fits to the pre-edge and post-edge regions as shown in Figure 3-12(a)-(c). However, this normalization approach carries the risk of incorrect pre-edge fitting and choosing an inappropriate normalization range, particularly for theoretical spectra with a limited energy coverage. This can lead to interference with the desired structure information.

To mitigate this issue, we explored a second normalization method called MBACK, using the Larch algorithm [14]. In this method, normalization is achieved by comparing the spectrum with a tabulated spectrum rather than fitting a polynomial curve to the pre-edge region, making the normalization more objective. We compared the results obtained from both normalization methods to ensure the accuracy of the normalization. The edge jump (Δμ) was measured, and the entire spectrum was divided by this value, ensuring that all absorption-energy spectra were normalized within a range of 0 to 1 (Figure 3-12(a)-(c)). The oscillatory behavior of the XANES spectra within a similar range after the edge jump indicates that the normalization process was performed correctly [31], [32].

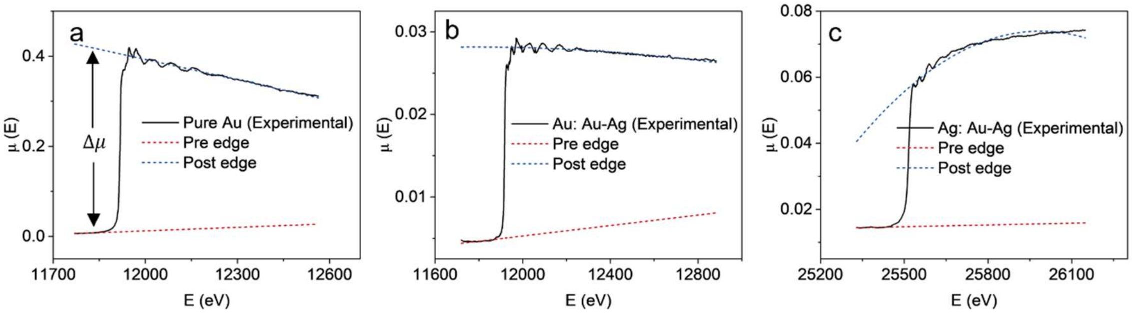

Figure 3-12. Au L_3-edge XAS data for TiO_2 nanowire samples with (a) a pure Au seed and (b) an Au-Ag seed, along with (c) Ag K-edge XAS data for nanowires with an Au-Ag seed. Two low-order polynomial curves were fitted to the pre-edge and post-edge regions for normalization, with the edge jump ($\Delta\mu$) indicated.

Atomic models incorporating Au, Ag, Ti, and O were selected to represent various plausible atomic configurations based on entries from the Crystallographic Open Database (COD) [33] and the Inorganic Crystal Structure Database (ICSD) [34]. The complete list of atomic models was presented in Table 3-4 and Table 3-5. To avoid redundancy, models were grouped according to the atomic arrangement around the absorber, ensuring structurally similar configurations were not repeated. Additionally, models that only existed under extreme conditions such as high pressures and temperature were excluded.

Two Au-Ag solution models were developed according to the compositions of Au-rich and Ag-rich domains. According to the EDS results in Table 6-1, an Au-rich solution (~94 at.% Au) and an Ag-rich solution (~30 at.% Au), comprised of 3,430 atoms, was built in aligning the EDS compositional analysis. Lattice parameters of 4.077 Å for the Au-rich model and 4.079 Å for the Ag-rich model were used to account for the lattice expansion of Au when alloyed with Ag [117]. Each model consisted of a 9×9×9-unit cell of Au, with 108 Au and Ag atoms randomly distributed as absorbers contributing to the simulated spectra. Another model with the same unit cell size but a different random distribution of

Au and Ag absorbers was also used, producing similar spectra. The consistency of XAS spectra across different configurations confirmed that the chosen model size was sufficient.

Theoretical Au L_3 and Ag K-edge XANES spectra were simulated using Finite Difference Method for Near Edge Structure (FDMNS) [35] code and processed using the same normalization methods to ensure consistency. Figure 3-13(a, b, c) shows the simulated XANES spectra for all proposed models after background subtraction and normalization.

Table 3-4. A comprehensive list of possible atomic models, including Au-Ti and Au-O structures, derived from COD and the ICSD database.

Bond	Configuration	Code	Model #	Formula	Crystal	Nearest neighbor	d (A)
Au-Au	Au with 12 Au	ICSD-53763	M1	Au	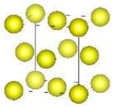	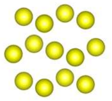	2.892
Au-Ag	Au with one Ag and 11 Au*	---	M1-1	$Au_{0.94}Ag_{0.06}$	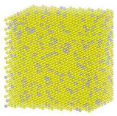	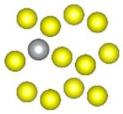	2.882
	Au with 9 Ag and 3 Au*	---	M1-2	$Au_{0.3}Ag_{0.7}$	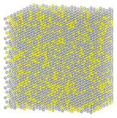	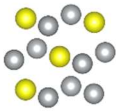	2.882
Au-Ti	Au with 8 Ti	COD-1510312	M2	Au Ti_3	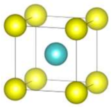	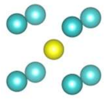	2.818
	Au Ti with partial CN	COD-1510313	M3	Au Ti_3	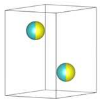		3.238
	Au with 12 Ti	COD-1510314	M4	Au Ti_3	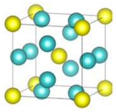	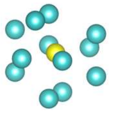	2.849

	Au with 12 Ti	COD- 23100 78	M5	Au Ti_3	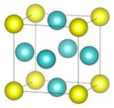	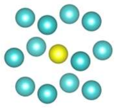	2.932
Au-O	Au with 4 O	COD- 8014	M6	Au_2O_3	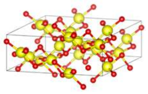	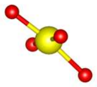	1.930

*Such configuration in Au-Ag models averaged over 108 absorber atoms with randomly distributed neighboring atoms.

Table 3-5. A comprehensive list of possible atomic models, including Au-Ti and Au-O structures, derived from crystallographic data and the ICSD database.

Bond	Configuration	Code	Model #	Formula	Crystal	Nearest neighbors	d (A)
Ag-Ag	Ag with 12 Ag	ICSD-53759	M0	Ag	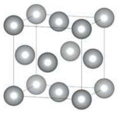	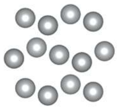	2.877
Ag-Au	Ag with 12 Au*	---	M1-1	$Au_{0.94}Ag_{0.06}$	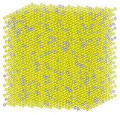	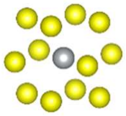	2.884
	Ag with 4 Au and 8 Ag*	---	M1-2	$Au_{0.3}Ag_{0.7}$	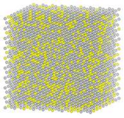	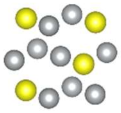	2.884
Ag-Ti	**Ag with 8Ti**	ICSD-58369	M7	AgTi	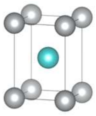	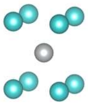	2.893
	Ag with 8 Ti	ICSD-58370	M8	$Ag\ Ti_3$	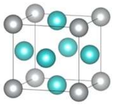	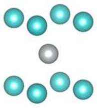	2.878
Ag-O	**Ag with 4 O (tetrahedron)**	ICSD-35662	M9	AgO	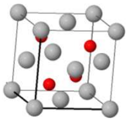	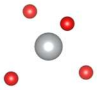	2.085
	Ag with 5 O (distorted octahedron)	ICSD-59193	M10	Ag_2O_3	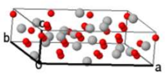	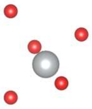	1.961
	Ag with 6 O (distorted octahedron)	ICSD-59225	M11	Ag_3O_4	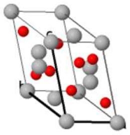	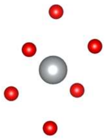	2.899
	Ag with 2 O (linear O-Ag-O)	ICSD-31058	M12	Ag_2O	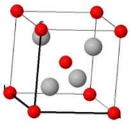	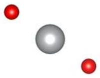	2.048

*Such configuration in Au-Ag models averaged over 108 absorber atoms with randomly distributed neighboring atoms.

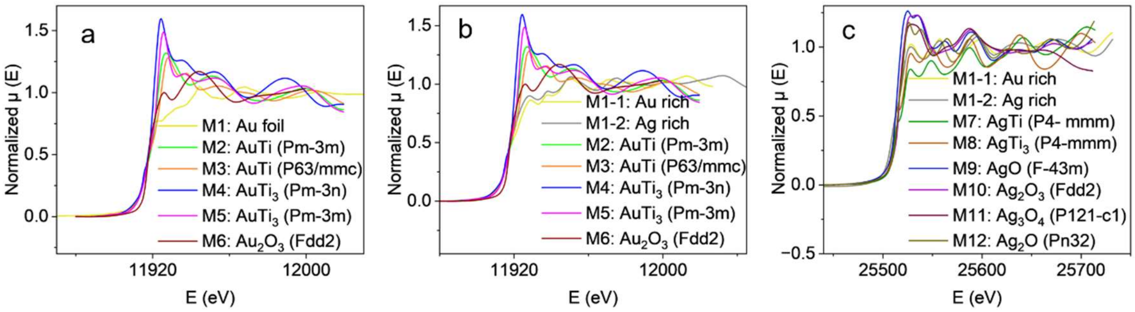

Figure 3-13. Simulated XANES spectra for the proposed theoretical models for Auafter applying the normalization process. Au L_3-edge XAS data for TiO_2 nanowire samples with (a) a pure Au seed and (b) an Au-Ag seed, along with (c) Ag K-edge XAS data for nanowires with an Au-Ag seed.

Linear Combination Fitting (LCF) was conducted to identify the optimal combination of theoretical models capable of reconstructing the experimental spectrum using Larch. The energy range analyzed was ±50 eV around the edge energy (E_0). To maintain a well-constrained and interpretable fit while minimizing the risk of overfitting, the number of maximum components was restricted to five, following standard practices suggested in the XAS community [29], [30], [36]. The best-fitting model was determined based on the R-factor and reduced χ^2 values.

3.4.3. Data Analysis of EXAFS

The EXAFS analysis was conducted using WinXAS [118] and Larch software [119]. Experimental spectra were Fourier transformed over the k-range of 3-11 Å^{-1} using a Hanning window function with a window parameter of 1, after background removal. The same window function and parameter were uniformly used for all samples across both Larch and WinXAS. This window is reported to minimize spectral leakage and improving resolution [120], [121]. Feff7 [122] was used to calculate all scattering paths for the 1st (2 Å < R < 3 Å, R is the bonding length), 2nd (3 Å to 4.5 Å) and 3rd (4.5 Å to 5 Å) shells. The experimental data were fitted following standard EXAFS modeling practices [123], [124]. The interatomic distances (R_i), coordination numbers (N_i), disorder factors (σ_i^2) for the theoretical scattering path (i), along with the amplitude reduction factor (S_0^2) and energy shift (E_0), were refined to obtain the best fit to the experimental data. For the 1st shell fitting, three main scattering paths were used with a common E_0 constrained between -8 and 8 eV. Coordination numbers were allowed to vary around theoretical values. The same E_0 shift was used for all samples as suggested in the literature while comparing similar systems without observable spectral shift [124], [125]. σ^2 was constrained between 0.002 and 0.01 Å^2, and S_0^2 was fixed at 0.73. Additional paths were incrementally added to fit higher shells, and coordination numbers were fixed after the first shell fitting to limit variable parameters and maintain fit reliability. Multiple-shell scattering contributions were not considered for simplification.

Chapter 4

Nanowire Synthesis via Argon Pressure Control

This chapter presents the synthesis outcomes of TiO_2 nanowires using different seed compositions, namely Au, Au-Ag, and Au-Ni. The initial nanowire growth experiments were conducted with an Au-Ni seed, although the presence of Ni was unintentional and initially unknown. To investigate the influence of oxygen partial pressure on nanowire growth, syntheses were carried out across a wide range of argon pressures—from near atmospheric pressure (93 kPa) down to 0.4 Pa—particularly for the Au-Ni system and subsequently extended to the Au-seeded growth for comparison.

4.1. TiO_2 Nanowires Grown with Au-Sputtered Thin Film Containing Ni

As described in Chapter 3, our initial nanowire growth was carried out on Au-sputtered substrates that unintentionally included trace amounts of Ni from the sputtering chamber. The resulting nanowires exhibited irregular morphologies—often kinked or zigzagged—as seen in Figure 4-1(a-i). A comprehensive description of nanowire morphology from TEM and SEM imaging can be found in Chapter 5. To improve control over growth, we systematically adjusted the argon (Ar) pressure, which in turn influenced the oxygen partial pressure within the tube (see Section 3.2.3 for oxygen partial pressure calculations). The experiments were conducted under pressures ranging from atmospheric (93 kPa) down to 0.4 Pa—the lowest achievable using our mechanical pump. These pressures were selected to establish the range within which nanowires can grow, while also allowing for a stepwise reduction in pressure to ensure safe handling during both the tube sealing and heat-treatment processes. Representative nanowire morphologies for various pressures are shown in Figure 4-1(a–h).

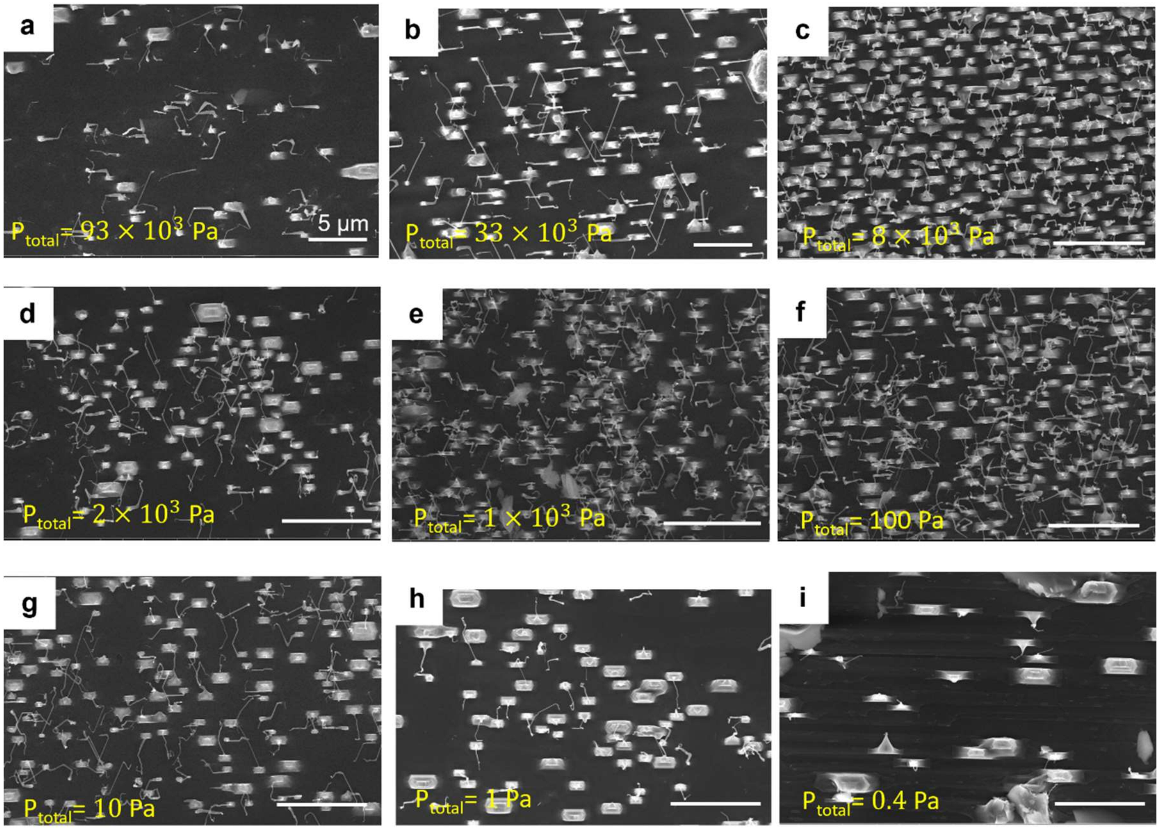

Figure 4-1. SEM images of TiO_2 nanowires grown on Au-sputtered substrates containing trace amounts of Ni under various Ar pressures, corresponding to different oxygen partial pressures. Images (a) to (i) show top-view SEM micrographs at Ar pressures of (a) 93 kPa, (b) 33 kPa, (c) 8 kPa, (d) 2 kPa, (e) 1 kPa, (f) 100 Pa, (g) 10 Pa, (h) 1 Pa, and (i) 0.4 Pa.

To evaluate the effect of pressure on nanowire growth, the lengths of more than 100 nanowires were measured for each condition. As described in Chapter 5 (Figure 5-1 to Figure 5-3), the nanowires predominantly grow along $<111>_{TiO_2}$, with a smaller fraction oriented along $<110>_{TiO_2}$. It should be noted that beneath individual nanowires, rectangular pyramid bases form, which are rutile bases elongated along $<001>_{TiO_2}$ [126], [127]. Similar faceted bases have been reported in Au–$MgAl_2O_4$ [128] and Au–$SrTiO_3$ [129] systems, where strong metal–oxide interfacial bonding and surface-energy anisotropy that reshapes the underlying oxide into low-energy faceted geometries, after which growth transitions to a wire-like morphology because subsequent TiO_x incorporation proceeds directionally along the preferred rutile growth axis rather than through further substrate reshaping. This feature provides a reliable reference for determining the crystallographic orientation of nanowires in SEM. Further confirmation of growth directions, based on observations in SEM and HRTEM, is provided in chapter 5 (Figure 5-1 to Figure 5-3). For length measurements, top-view SEM imaging was carried out along the $<110>_{TiO_2}$ zone axis, so only nanowires oriented in the dominant $<111>_{TiO_2}$ growth direction were measured. Because top-view imaging provides only the projected length, a correction was applied to obtain the actual values, using the $<111>_{TiO_2}$ growth direction which forms a 24.49° angle with the vertical axis. Table 4-1 summarizes the projection equivalents for $<111>_{TiO_2}$ nanowires and the corrected length measurements for each case. For simplicity, the pressure values have been rounded to 1 Pa, 10 Pa, 100 Pa, and 1000 Pa.

The average nanowire lengths across four Ar pressures are presented in Figure 4-2. Growth at 33 kPa produced nanowires with an average length of ∼5.25 μm, which increased to ∼6.37 μm at 100 Pa. However, growth significantly decreased at 1 Pa, with lengths averaging ∼2.93 μm. At the extremes—93 kPa and 0.4 Pa—very few nanowires were observed on the substrate, preventing reliable statistical analysis. The standard deviation of nanowire lengths (h) for each Ar pressure was calculated using Equation 4-1.

$$\delta h = \sqrt{\frac{1}{n_w - 1}\sum_{1}^{n_w}(h_i - \bar{h})^2} \tag{4-1}$$

Where h_i is each nanowire measured length, $\bar{h}$ is the average length, and n_w is the number of nanowires measured. Overall, nanowire growth shows some dependence on oxygen partial pressure, but the changes in average length within the tested range are relatively modest (differences of only a few micrometers).

Table 4-1. Schematic showing the different orientations of $<111>_{TiO_2}$ nanowires in cross-sectional views ($<\bar{1}10>_{TiO_2}$ and $<001>_{TiO_2}$) and in the top view ($<110>_{TiO_2}$), along with the corresponding length correction for each case. Nanowires requiring length correction are illustrated as red rods, while those where the projected and actual lengths are equal are shown as blue rods. The pyramid-shaped nanowire bases are indicated in gray.

Cross-sectional view <1$\bar{1}$0>	**Cross-sectional view <001>**	**Top view <110>**	**Corrected length**
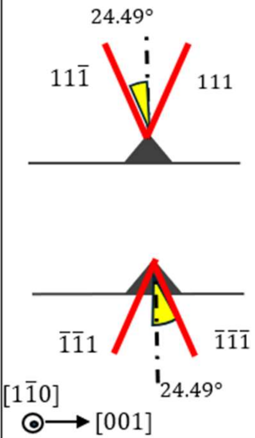	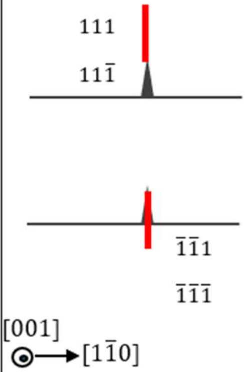	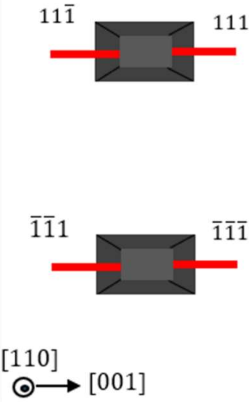	$\frac{Projected\ length}{Sin\ (24.49°)}$
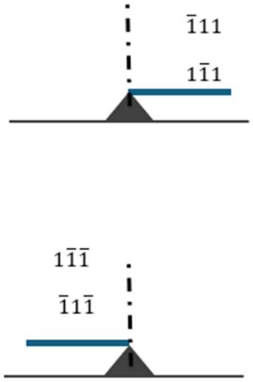	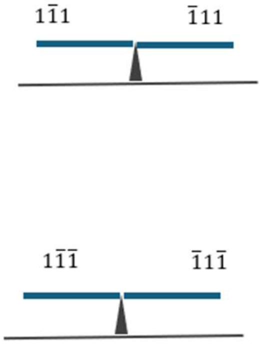	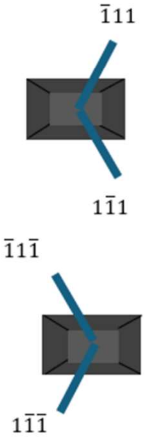	Projected length
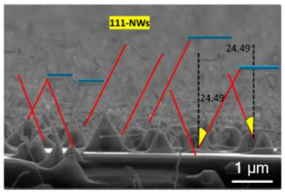	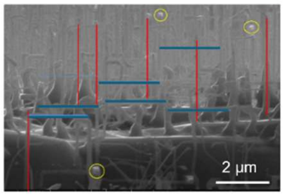	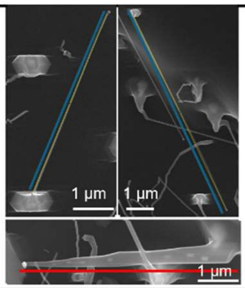	

When oxygen partial pressure is too high (near 1 Pa), the thermal decomposition of the TiO_2 substrate (Equation 4-2 [130], [131])—which serves as the source of growth species—is suppressed, limiting the supply of reactive species for nanowire formation. Conversely, when the oxygen partial pressure is too low (around 1 μPa), the re-condensation of TiO_2 becomes unfavorable, reducing the nanowire growth rate. Therefore, an optimal range of oxygen partial pressure—achieved by tuning the Ar background pressure—is required for promoting efficient nanowire growth in this system.

$$TiO_2\,(s) \leftrightarrow TiO_x\,(g) + \frac{(2-x)}{2} O_2\,(g) \tag{4-2}$$

In contrast to Zhuge et al. [16] (PLD with external Ti flux and flowing Ar/O_2 at fixed total pressure, yielding ~0.01–0.1 Pa), our closed, no-flow geometry produced TiO_2 nanowires over a broader, lower window of $\sim 1\times10^{-4}$–0.5 Pa. This wider range is likely because the local oxygen activity at the nanowire–seed tip is buffered: without convective sweep, O_2 may be neither rapidly depleted nor oversupplied; reversible Ti/TiO_x redox and seed-mediated uptake could maintain a workable O chemical potential even at very low ambient P_{O_2}; and the absence of a strong external flux may reduce sidewall VS deposition at higher P_{O_2}.

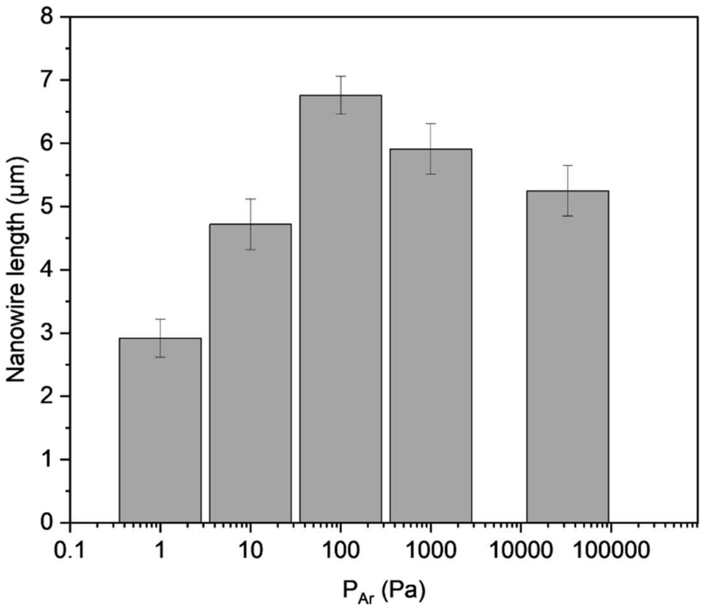

Figure 4-2. Bar chart showing the average lengths of more than 100 TiO_2 nanowires grown on Au-sputtered substrates containing Ni at four different Ar pressures: 1 Pa, 10 Pa, 100 Pa, 1000 Pa, and 33,000 Pa. Error bars indicate the standard deviation of the length measurements for each pressure condition.

4.2. TiO_2 Nanowires Grown with Au Nanoparticle Deposition

To eliminate the influence of Ni and other possible contaminants introduced during sputtering, nanowires were synthesized using deposited Au nanoparticles as seeds, as outlined in Chapter 3. Figure 4-3 displays typical SEM images of nanowires grown with this method. The resulting nanowires display a bead-like morphology along the <110> TiO_2 direction, consistent with earlier reports on pure Au-seeded growth via the VAdS method [116]. However, slight variations in bead formation are observed, likely due to the influence of residual PBS stabilizing agents. Pyramid-shaped bases growing along the <001> direction were used as markers to confirm the nanowire growth direction.

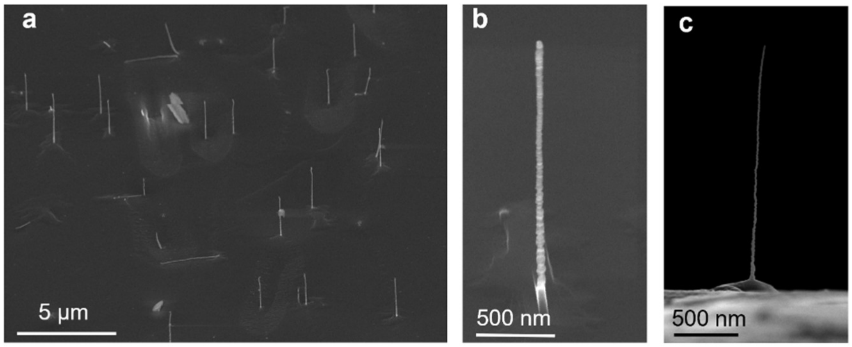

Figure 4-3. SEM images of TiO_2 nanowires synthesized with deposited Au nanoparticles at 100 Pa Ar pressure: (a) top-view image at a 45° tilt, and cross-sectional views along (b) the $[001]_{TiO_2}$ and (c) the $[1\bar{1}0]_{TiO_2}$ directions.

To study the effect of Ar pressure on this growth method, nanowires were synthesized under various conditions: 33 kPa, 1000 Pa, 100 Pa, 10 Pa, and 1 Pa, as shown in Figure 4-4(a–e). These pressure values were chosen based on the safe and effective range identified in the Au–Ni case. Similar to the Au–Ni seeded case, nanowire growth showed a slight dependence on pressure.

Quantitative length measurements for each pressure condition were obtained from cross-sectional images (either $< 1\bar{1}0 >_{TiO_2}$ or $< 001 >_{TiO_2}$), since top-view imaging $< 110 >_{\mathrm{TiO_2}}$ cannot capture nanowires that grow along the beam direction. The results are summarized in the bar graph in Figure 4-5. Maximum growth occurred at 100 Pa, yielding an average nanowire length of approximately 2.78 μm. In contrast, growth was significantly reduced at 1 Pa (0.89 μm) and at 33 kPa (1.69 μm). The standard deviation of nanowire length was calculated as described in Section 4.1. Overall, the nanowires grown with Au nanoparticle seeds were shorter than those synthesized with Au–Ni seeds. This reduction may be attributed to residual stabilizers from the nanoparticle solution, which could interfere with nanowire growth.

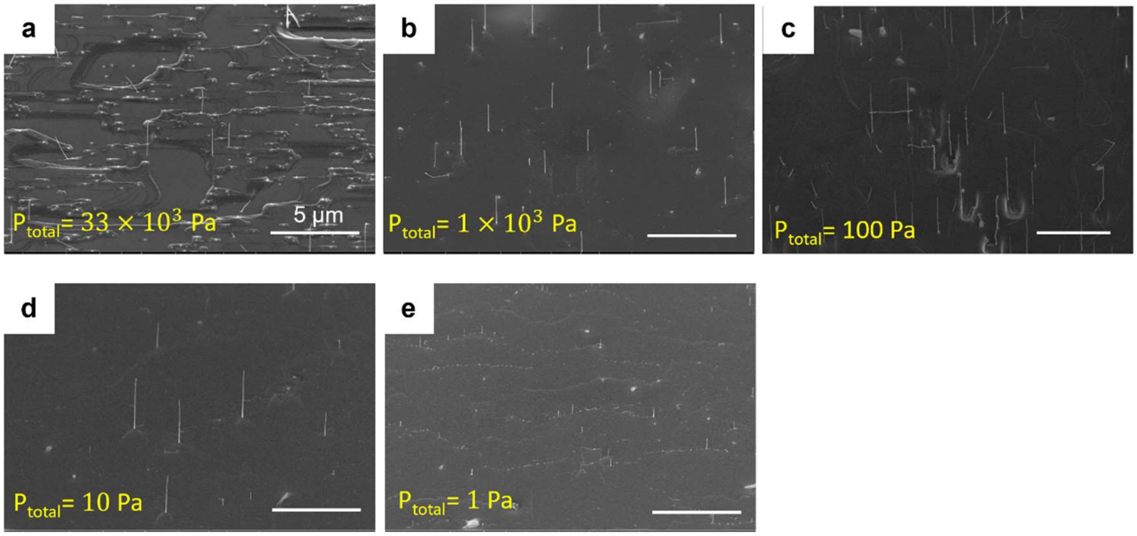

Figure 4-4. SEM images of TiO_2 nanowires grown on deposited Au nanoparticles under various Ar pressures, corresponding to different oxygen partial pressures. Images (a) to (e) show top-view SEM micrographs at Ar pressures of (a) 33 kPa, (b) 1 kPa, (c) 100 Pa, (d) 10 Pa, and (e) 1 Pa.

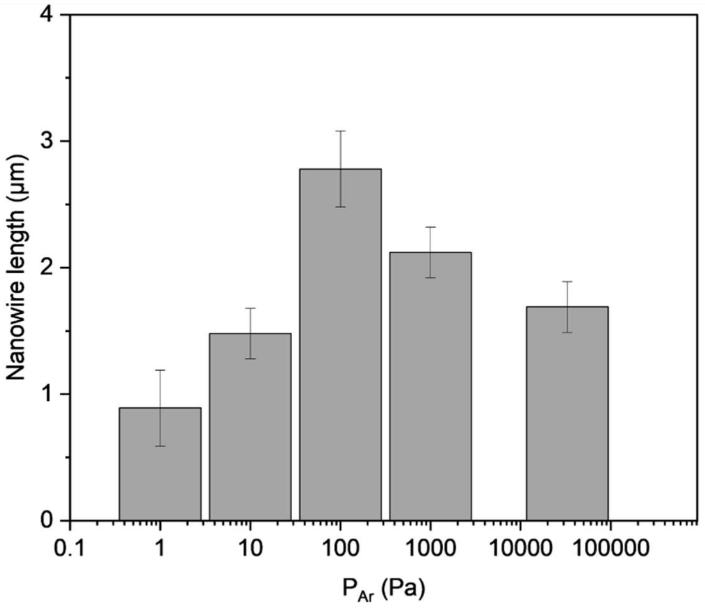

Figure 4-5. Bar chart showing the average lengths of TiO_2 nanowires grown on deposited Au nanoparticles at four different Ar pressures: 1 Pa, 10 Pa, 100 Pa, 1000 Pa, and 33,000 Pa. Error bars indicate the standard deviation of the length measurements for each pressure condition.

4.3. TiO_2 Nanowires Grown with Au-Ag Nanoparticle Deposition

To evaluate the reproducibility of the VAdS method with different bimetallic seeds, nanowires were synthesized using Au–Ag nanoparticles deposited on TiO_2 substrates. SEM images of the resulting nanowires are shown in Figure 4-6. Growth was carried out at 100 Pa Ar pressure, which was previously identified as the optimal condition for both pure Au and Au–Ni systems.

A kinking behavior was observed, where the nanowire morphology transitioned from a bead-like shape along $<110>_{TiO_2}$ (shown by red arrows in Figure 4-6) to a prismatic structure along $<111>_{TiO_2}$ (yellow arrows in Figure 4-6). This transition is visible in the top-view SEM images taken at a 45° tilt (Figure 4-6(a)) and in the cross-sectional view (Figure 4-6(b), (c)). This morphological change is consistent with previous reports involving Au–Ag seeds [59], [116], though slight variations are likely due to the presence of residual stabilizing agents. The prismatic kinked portions (red arrows) are notably shorter than the vertically aligned bead-like segments (yellow arrows), which may be related to the reduced Ag fraction in the Au–Ag solution after repeated centrifugation and dilution, as well as possible effects of stabilizers.

The average length of the synthesized nanowires was measured to be approximately 1.82 ± 0.3 µm, which is shorter than that observed for nanowires grown with pure Au seeds. This reduced length may be attributed to residual stabilizing agents from the nanoparticle solution. In the case of Ag-containing nanoparticles, it is more difficult to fully separate the stabilizing agents during centrifugation due to the similar color of the nanoparticle pellet and the surrounding solution—unlike Au nanoparticles, which form a clearly distinguishable red pellet. This likely results in a higher amount of residual stabilizers that interfere with nanowire growth.

It is important to note that for subsequent spectroscopic analysis of the bonding environment around Au and Ag (chapter 6), previously prepared samples containing pure Au and pure Ag nanoparticles were used. This ensured that stabilizing agents did not interfere with the spectroscopic measurements.

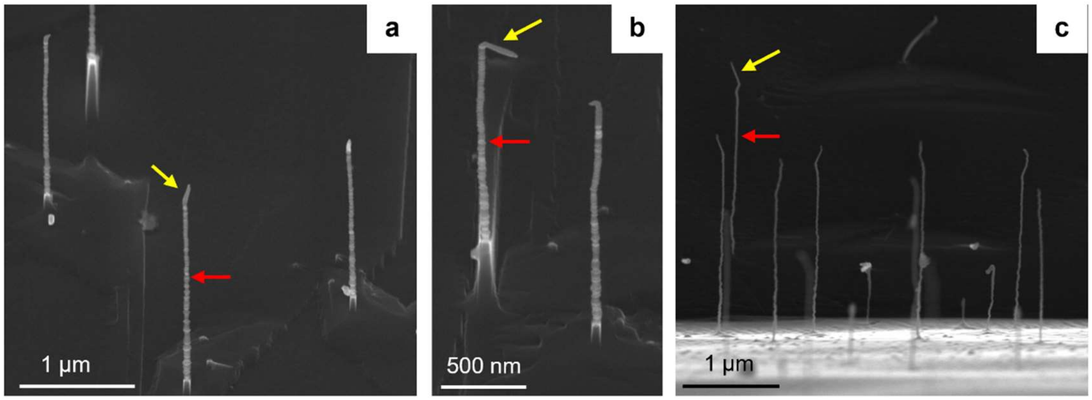

Figure 4-6. SEM images of TiO_2 nanowires synthesized with deposited Au-Ag nanoparticles at 100 Pa Ar pressure: (a) top-view image at a 45° tilt, and cross-sectional views along (b) the $[001]TiO_2$ and (c) the $[1\bar{1}0]TiO_2$ directions. Red arrows indicate the bead-like sections of the nanowires, while yellow arrows highlight the prismatic regions.

4.4. Summary

This chapter presented the results of applying the VAdS method to three different seed systems: Au–Ni (from sputtered thin films), and Au and Au–Ag (from nanoparticle deposition), where residual PBS stabilizing agents may be present. All three approaches produced TiO_2 nanowires with micrometer-scale lengths. Nanowires grown from sputtered films containing Ni exhibited less uniformity and pronounced zigzag morphologies, likely due to contamination. In contrast, nanowires grown from nanoparticle deposition displayed less zigzagging, with Au nanoparticles producing bead-like nanowires that grew predominantly vertical, while Au–Ag nanoparticles yielded nanowires with a slight kink transitioning toward prismatic shapes. Nanoparticle-deposited nanowires were generally shorter, and not all exhibited uniform shapes or consistent growth directions along their length, effects that may be associated with the presence of stabilizing agents. To further improve nanowire length and consistency, future work should focus on nanoparticle deposition methods that avoid stabilizing agents.

Nanowire growth was studied across a wide range of Ar pressures, from atmospheric pressure down to 0.4 Pa (the minimum pressure achievable with our mechanical pump). The results indicate that the optimal pressure range for growth lies between 10 and 1000 Pa, where nanowires exhibit higher growth rates. This is attributed to an optimal oxygen partial pressure—low enough to promote thermal decomposition of the TiO_2 substrate and high enough to enable TiO_x condensation during nanowire formation. Compared with the narrower oxygen window reported by Zhuge et al. [16] (~0.01–0.1 Pa in a PLD system), our closed, no-flow geometry supports growth over a broader, lower range (~1×10^{-4}–0.5 Pa), likely because oxygen activity near the seed tip is buffered without convective sweep.

Chapter 5

Ni-Assisted Endotaxial Growth of Au Nanoparticles within TiO_2 Nanowires

In this chapter, we explore the impact of incorporating a small amount of Ni into the Au seed to form an Au-Ni bimetallic seed and examine its influence on the growth behavior of TiO_2 nanowires. This seed engineering approach is used to investigate the potential for modifying the Au–TiO_2 interface and enabling the formation of embedded Au nanopeapods. Through a comparative analysis of nanowire morphology and orientation relationships, we identify the frequent emergence of new orientation alignments between the nanowire and the embedded nanoparticles, indicating their critical role in nanopeapod formation. Furthermore, structural instabilities—such as periodic bead-like oscillations and step-like features on the prismatic nanowire surface—are examined as contributing factors, likely linked to thermal fluctuations during growth. Together, these results shed light on the combined effects of crystallography and growth dynamics in enabling nanoparticle embedding, providing insights into more controlled nanopeapod synthesis.

5.1. Nanowire Morphology

The single-crystal nanowires exhibit variations in their axial directions, resulting in kinked or zigzag patterns as illustrated in the top-view image along $[110]_{TiO_2}$ in Figure 5-1(a) and the cross-sectional image along $[1\overline{1}0]_{TiO_2}$ in Figure 5-1(b). They grow either at an inclination relative to the rutile $(110)_{TiO_2}$ substrate surface—as highlighted by the green arrows in Figure 5-1(a) and Figure 5-1(b)—or extend vertically, as indicated by the yellow arrow in Figure 5-1(b). This corresponds to the axial direction along $<111>_{TiO_2}$, which has an inclination angle of 65.51°, and along $[110]_{TiO_2}$, perpendicular to the substrate surface, respectively. In this chapter, we use the term axial direction instead of growth direction because the nanowire growth fronts are not flat (see Figures). While the growth direction refers to the motion of the interfaces as atoms are incorporated, the axial direction is simply the crystallographic orientation along the nanowire length—parallel to the side facets for prismatic wires or given by the intersection of two non-parallel facets in bead-like wires. The lengths of these nanowires range from several hundred nanometers to a few micrometers, with an average length of approximately 5 μm. Unlike the nanowire width, which spans several tens of nanometers, the diameter of the gold seed was measured at around 35 nm across more than a hundred nanowires. Beneath these nanowires are rectangular pyramid-shaped bases elongated along $[001]_{TiO_2}$. Similar bases have been observed in other gold-oxide systems [132], [133], [134] and form prior to nanowire growth.

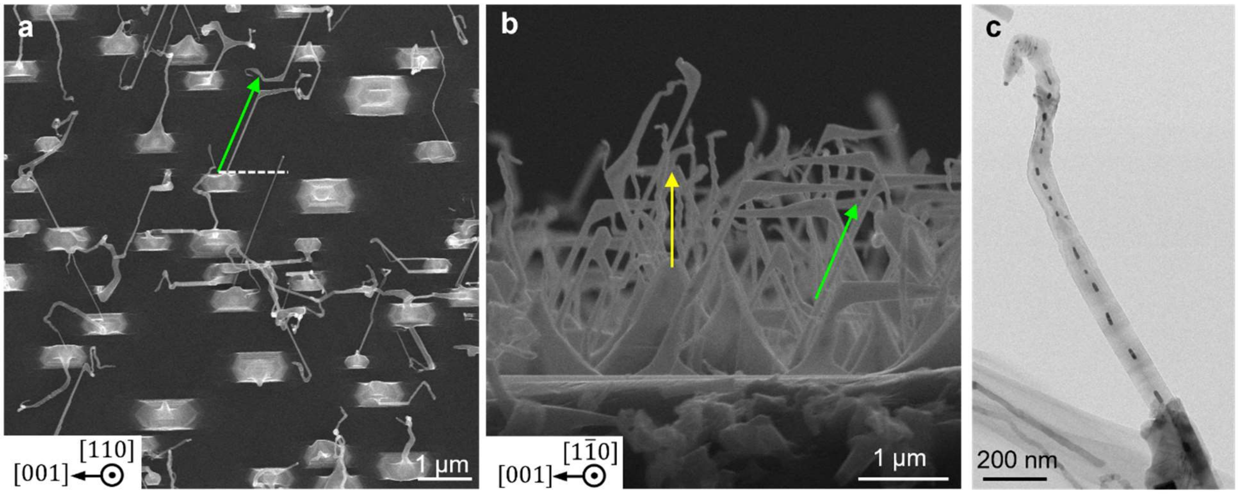

Figure 5-1. Morphology of TiO_2 nanowires. (a) An SEM image illustrating the top view along $[110]_{TiO_2}$. (b) An SEM image showing the cross-sectional view along $[1\bar{1}0]_{TiO_2}$. (c) A TEM bright-field (BF) image of a single nanowire, highlighting a chain of embedded gold nanoparticles.

The typical morphology of kinked nanowires is illustrated in TEM Bright-Field (BF) micrograph in Figure 5-1(c), Figure 5-2, and Figure 5-3. Most nanowires keep prismatic shape, with their axial direction along $<111>_{TiO_2}$, while nanowires growing along $[110]_{TiO_2}$, exhibit a bead-like morphology. No stacking fault or twinning is observed during changes in axial direction, suggesting that nanowires remain as single crystals throughout growth (Figure 5-2 and Figure 5-3). Within both types, chains of embedded nanoparticles, often with polygonal shape, are frequently observed. Tilting individual nanowires along various directions reveals that the nanoparticles remain stationary at the center, indicating that they are embedded inside the nanowires. (see Figure 5-2 to Figure 5-7). Furthermore, as illustrated in Figure 5-1(c), embedded nanoparticles are likely located at the kinked and zigzag sections of the nanowires or in areas where the nanowire width is reduced.

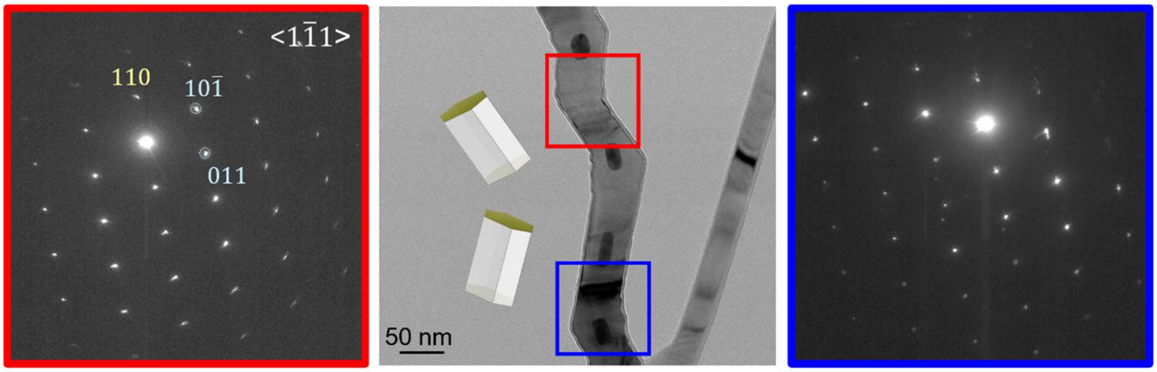

Figure 5-2. TEM bright-field (BF) image of a prismatic nanowire viewed along $<1\bar{1}1>_{TiO_2}$, accompanied by diffraction patterns taken from two translation regions of axial directions, marked by red and blue squares.

Figure 5-3 shows a ~20 nm-wide nanowire with short segments of ~10 nm in length, transitioning from prismatic (I) to bead-like (II) to prismatic segments (III) underneath a curved growth front. The lattice fringes in High-resolution TEM images and corresponding diffraction patterns, viewed from $[1\bar{1}1]_{TiO_2}$, confirm the presence of the $(10\bar{1})_{TiO_2}$ and $(\bar{1}01)_{TiO_2}$ sidewall facets for prismatic segments. This nanowire has curved growth front but contain no embedded nanoparticles, since all embedded nanoparticles are 20 nm or larger in size. In the bead-like segment, additional sidewall facets are observed, including $(011)_{TiO_2}$ and $(0\bar{1}\bar{1})_{TiO_2}$, along with the same $(10\bar{1})_{TiO_2}$ and $(\bar{1}01)_{TiO_2}$. The axial direction of bead-like segment, labelled by the yellow arrow, is $[110]_{TiO_2}$. The axial direction of prismatic segment, also labelled as yellow arrows, is identified as is $[111]_{TiO_2}$, which is parallel to the observed $(10\bar{1})_{TiO_2}$ and the reported sidewall facet $\{1\bar{1}0\}_{TiO_2}$.

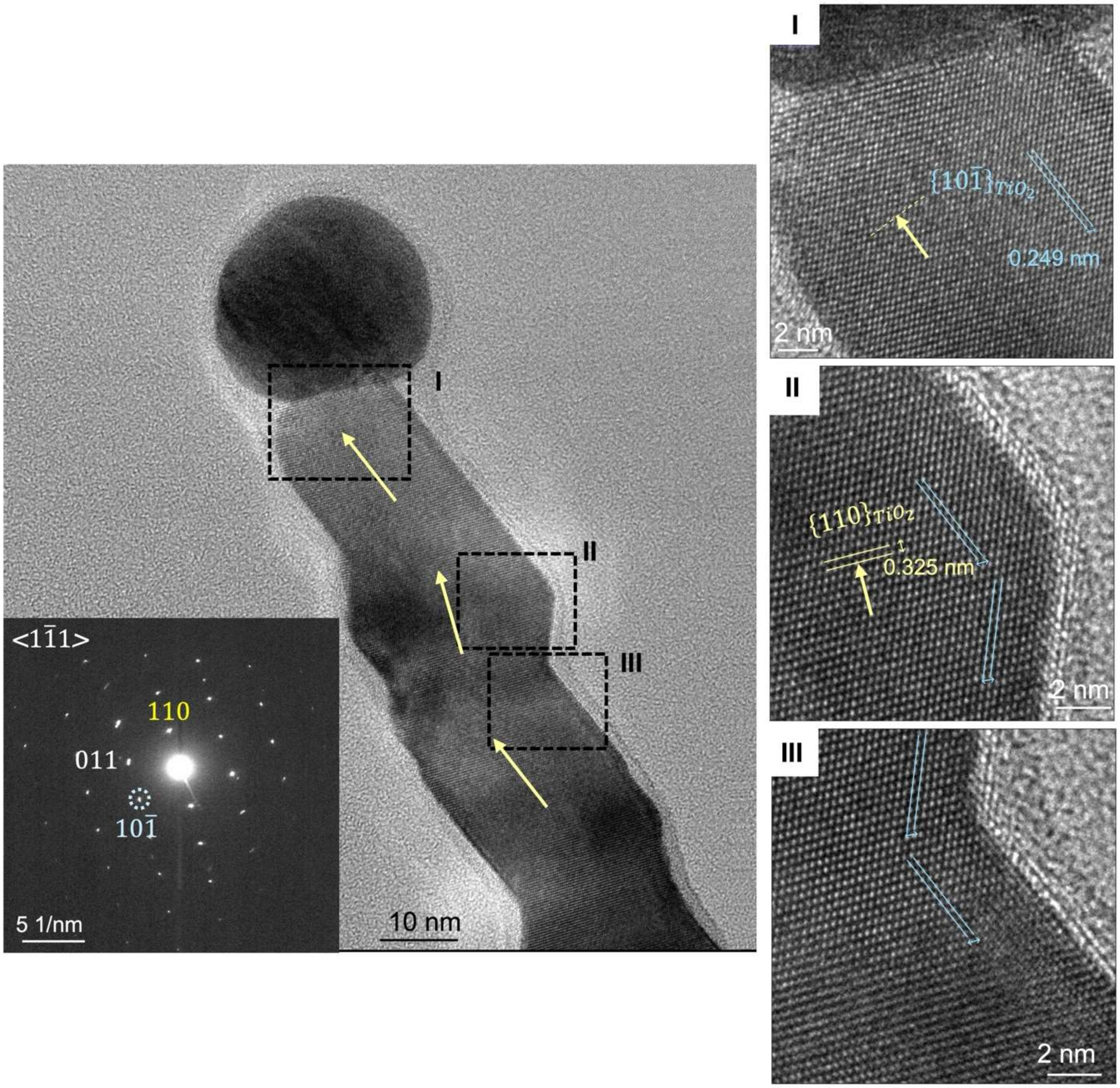

Figure 5-3. HRTEM images of ~20 nm-wide nanowire displaying multiple segments (I, II, and III) with the axial directions labelled by yellow arrows. The corresponding diffraction pattern is inserted. The measured d-spacing confirm the presence of the $(10\bar{1})_{TiO_2}$ and $(011)_{TiO_2}$ side facets and $\{110\}_{TiO_2}$, which is vertical to the axial direction of bead-like segment.

5.2. Nanowire and Nanoparticle Composition

The energy-dispersive X-ray (EDX) compositional mapping was conducted on one representative bead-like nanowire (Figure 5-4(a)) and one prismatic nanowire (Figure 5-4(c) to (f)), as well as one randomly shaped and zigzag-structured nanowire (Figure 5-5). These results reveal that the embedded nanoparticles are primarily composed of Au, with minor amounts of Ni detected. A representative EDX spectrum in Figure 5-4(b) clearly shows distinct Ni peaks. The EDX mappings of individual embedded nanoparticles, labelled as 1 to 3 and marked by yellow boxes, are shown in Figure 5-4(a) for one bead-like nanowire and in Figure 5-4(c) to f for one prismatic nanowire.

While Ni signals were detected almost uniformly across the embedded nanoparticles within the bead-like nanowires, Ni segregations were observed in the prismatic nanowires, as shown in Figure 5-4(c) to (f). In the prismatic nanowires, embedded Au particles are often elongated along the axial direction, with Ni segregations consistently observed at one end of the elongated particles, as supported by EDX maps taken from different zone axes. Au-rich regions contain less than 1 wt.% Ni, while the Ni-rich regions have an average Ni composition of 17 wt.%, based on analysis of >10 nanoparticles. It should be noted that the Ni concentration in the Ni-rich regions may be underestimated due to unavoidable overlap of Au-rich regions. Interestingly, nanoparticle 2 (Figure 5-4(c) to (f)), which has a well-defined shape, shows barely detectable Ni signals in Au-rich regions, compared to nanoparticles 1 and 3 locating at kinked regions. The presence of Ni segregations is consistent with the Au-Ni phase diagram [135], in which Au and Ni form solutions at high temperatures but become immiscible at room temperature. It is hypothesized that at the growth temperature (i.e., 1000°C), the seeds and embedded nanoparticles exist as Au-Ni solutions and can undergo phase separation upon cooling to room temperature. The degree of phase separation can potentially be tailored by the constraints of surrounding rutile lattice, which is related to the crystallographic orientation relationship (OR) between embedded gold nanoparticles and rutile nanowires, as discussed below.

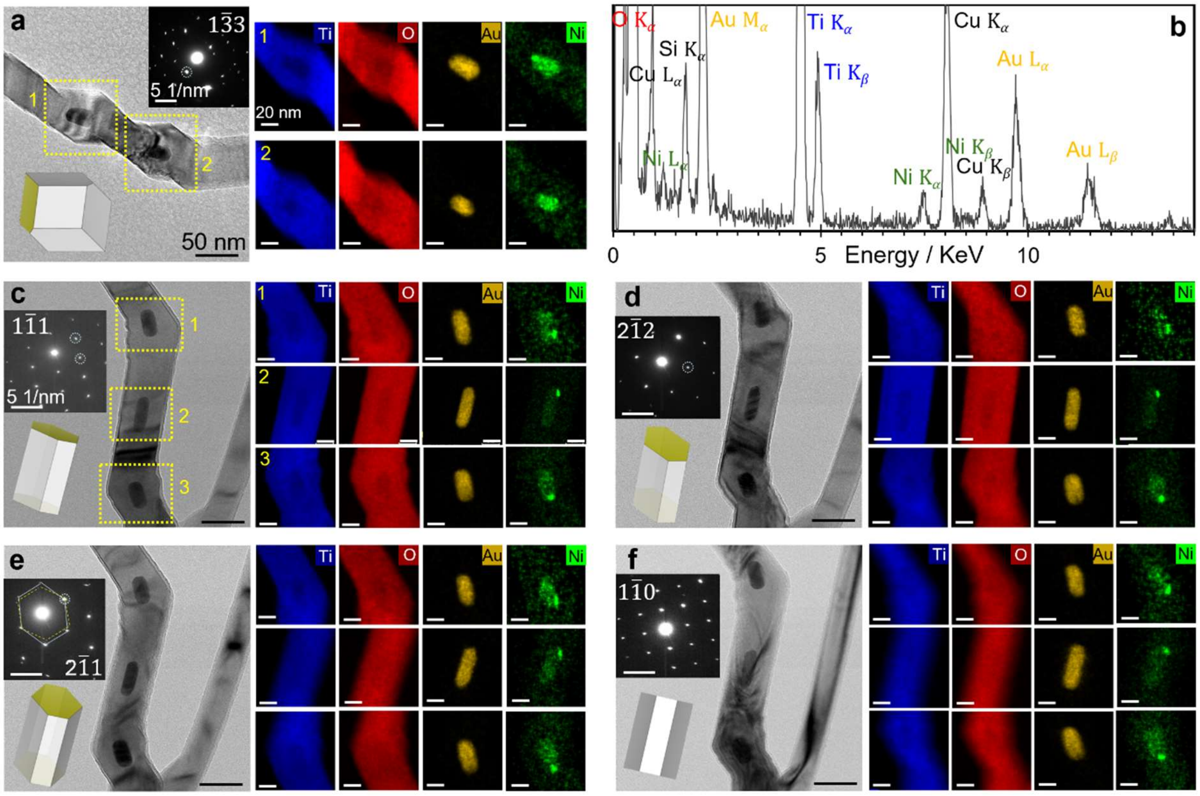

Figure 5-4. EDX elemental mapping of Ti, O, Au, and Ni in two types of nanowires: (a) bead-like and (c-f) prismatic. The EDX mapping regions, containing one embedded nanoparticle, were marked by yellow squares and numbered as 1,2 for the bead-like nanowire and 1,2,3 for the prismatic nanowire. One typical prismatic nanowire was tilted along different zone axes: (c) $< 1\bar{1}1 >$, (d) $< 2\bar{1}2 >$, (e) $< 2\bar{1}1 >$, and (f) $< 1\bar{1}0 >$, to identify the 3D shape and distribution of Ni segregation within the embedded nanoparticles. The insets depict 3D models of both nanowire morphologies, viewed along corresponding zone axes. The grey facets are side facets of nanowires while the yellow facets illustrate the hypothetical growth front assuming a flat front. In each diffraction pattern, the reflections corresponding to the $\{101\}$ side facets are labelled with dashed circles. (b) EDX spectrum of one embedded nanoparticle. All scale bars are 50 nm in BF images

and 20 nm for EDX maps. The indexing of the corresponding diffraction patterns is shown in detail in Figure C-1 (Appendix C).

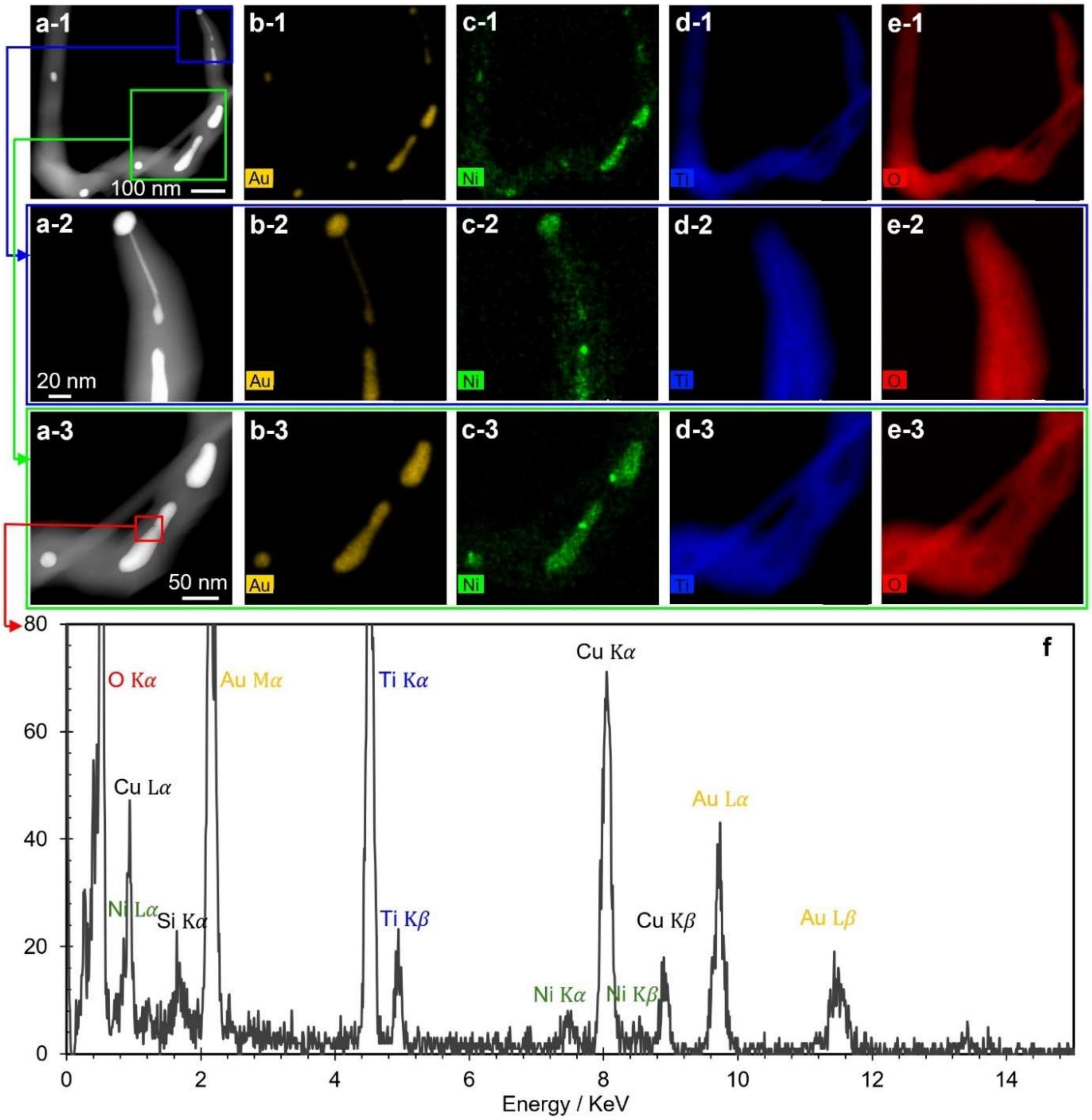

Figure 5-5. EDX elemental mapping of Ti, O, Au, and Ni in a nanowire. (a-1) to (e-1) The distribution of Ti, O, Au, and Ni within the nanowires. Enlarged views and elemental compositions are shown for the regions marked by blue squares in (a-2) to (e-2) and green squares in (a-3) to (e-3) to illustrate the Ni distribution. (f) EDX spectrum for the red-marked region of the embedded nanoparticle, where Ni segregation is observed.

5.3. Orientation Relationship (OR)

In bead-like nanowires, most embedded gold nanoparticles maintain the commonly reported ORs [34–36], which aligns Au low-index crystallographic planes with $\{110\}_{\mathrm{TiO_2}}$ planes, as shown in the BF images and corresponding diffractions in Figure 5-6(a) to (c) and Figure 5-2. All nanowires were examined along multiple zone axes, with at least one axis showing overlapping diffractions from both Au and TiO_2, which were used for OR analysis. In Figure 5-6c, the gold nanoparticle exhibits an OR approximately described as $<110>_{\mathrm{Au}}//<111>_{\mathrm{TiO_2}}$ & $\{1\bar{1}1\}_{\mathrm{Au}}//\{1\bar{1}0\}_{\mathrm{TiO_2}}$, based on the overlapping $<111>_{\mathrm{TiO_2}}$ diffraction labelled with blue dashed lines and $<110>_{\mathrm{Au}}$ diffraction outlined by the yellow dashed line.

Periodic changes in the nanowires' morphology are further analyzed along different zone axes to construct their three-dimensional morphology. Figure 5-6a to c displays a representative bead-like nanowire aligned along the $<0\bar{1}1>_{\mathrm{TiO_2}}$, $<1\bar{3}3>_{\mathrm{TiO_2}}$, and $<1\bar{1}1>_{\mathrm{TiO_2}}$ zone axes, respectively, accompanied by schematics and 3D model illustrating the facets. The nanowires consist of two beads, bounded by two $\{1\bar{1}0\}_{\mathrm{TiO_2}}$ facets and eight $\{101\}_{\mathrm{TiO_2}}$ facets, consistent with the reported facets of bead-like TiO_2 nanowires [15], [59].

The Au-TiO_2 interface at the growth front, if flat, is identified as $\{110\}_{\mathrm{TiO_2}}$, which is perpendicular to the axial direction of bead-like nanowires. This growth front periodically transitions from a rhombohedral-like shape to a hexagonal-like shape (expanding from stage I to II in Figure 5-7(c) and then back to a rhombohedral-like shape). Nanoparticles are embedded within the nanowire following the completion of the expansion (stage II in Figure 5-7(c)) and the onset of contraction. This bead-like shape of the nanowire is likely associated with the nanoparticles sinking into the nanowire, similar to the reported Au nanopeapods in SiO_2 nanowires [89], [90].

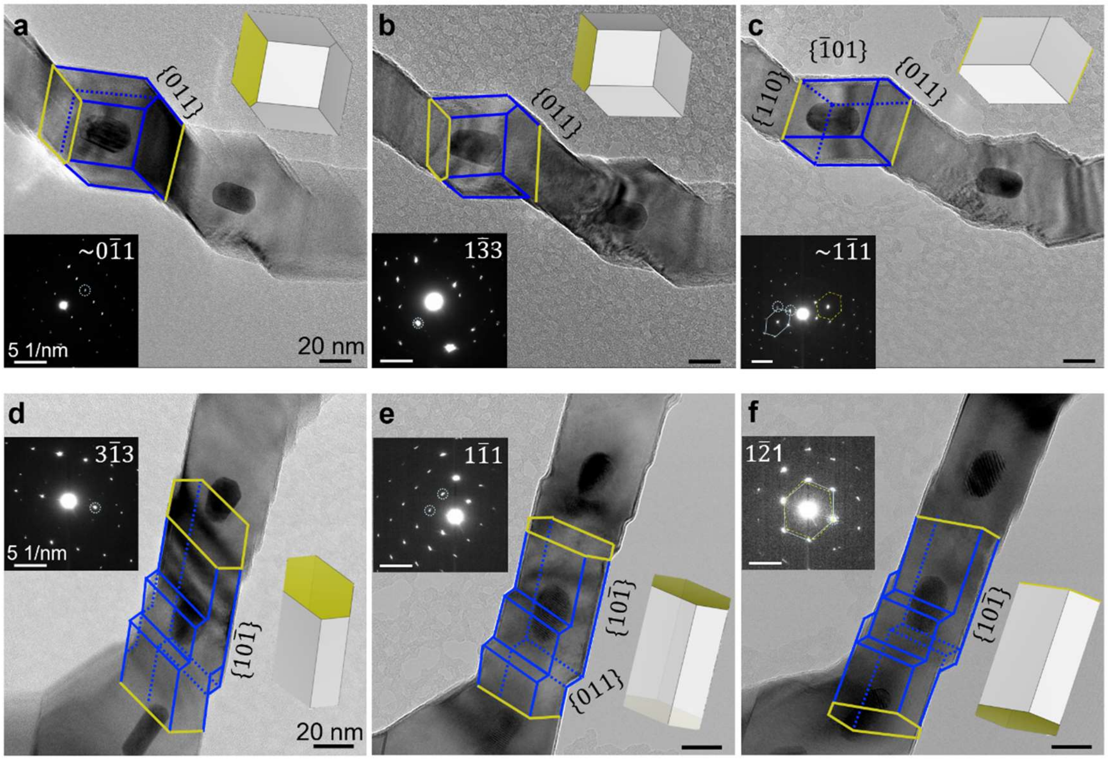

Figure 5-6. TEM bright-field (BF) images and corresponding electron diffraction patterns of bead-like (a-c) and prismatic (d-f) nanowires from different zone axes. In each diffraction pattern, the {101} reflections, corresponding to the edge-on side facets, are labelled with dashed circles. In (c), a solid yellow circle highlights the most possible growth front. The blue schematics outlines the shape and all side facets of the nanowires. Insets include 3D models of the nanowires, with yellow facets showing the imaginary growth front. The blue solid lines and yellow dashed lines indicate overlapping diffraction patterns of TiO_2 and Au, respectively. The indexing of the corresponding diffraction patterns is shown in detail in Figure C-1 (Appendix C).

Figure 5-7 illustrates the periodic oscillations in the morphology of both bead-like (a–c) and prismatic (d–f) nanowires. The 3D models and drawings in Figure 5-7(a), (b) and Figure 5-7(d), (e) provide an approximation of the nanowire shape, morphology, and side facets in the corresponding zone axis. In our modelling, we assumed a flat growth front (top facet) perpendicular to all side facets, identified as

$\{110\}_{\mathrm{TiO_2}}$ for bead-like nanowires and $\{2.4\ 2.4\ 1\}_{\mathrm{TiO_2}}$ for prismatic nanowires. For bead-like nanowires, the periodic expansion and contraction cause the growth front to oscillate between a rhombohedral shape (section I) and a hexagonal shape (section II), as depicted in the cross-sectional schematic (Figure 5-7(c)). The formation of embedded nanoparticles is linked to these oscillations, as they appear at the transition from expansion to contraction (section II to section I). In contrast, ideal prismatic nanowires would not exhibit growth front oscillations. However, the prismatic nanowire shown in Figure 5-7(d) to f features small $\{011\}_{\mathrm{TiO_2}}$ side facets, as revealed by the TEM image (d) and represented in the 3D model (e). The top facets of cross-sections I and II are illustrated in Figure 5-7(f). Although growth front oscillations in prismatic nanowires are minimal, the formation of embedded nanoparticles still aligns with these fluctuations. These morphological variations may be attributed to thermal fluctuations during growth.

Figure 5-6(d) to (f) presents another prismatic nanowire observed along the $<3\bar{1}3>_{\mathrm{TiO_2}}$, $<1\bar{1}1>_{\mathrm{TiO_2}}$, and $<1\bar{2}1>_{\mathrm{TiO_2}}$ zone axes, respectively. Prismatic nanowires are composed of two $\{1\bar{1}0\}_{\mathrm{TiO_2}}$ and four $\{10\bar{1}\}_{\mathrm{TiO_2}}$ parallel facets (see Figure 5-4and Figure 5-6), similar to those previously reported in [15]. In addition to the ideal prismatic structure, small $\{011\}_{\mathrm{TiO_2}}$ facets emerge, as shown in the micrographs taken along $<3\bar{1}3>_{\mathrm{TiO_2}}$, $<1\bar{1}1>_{\mathrm{TiO_2}}$, and $<1\bar{2}1>_{\mathrm{TiO_2}}$ in Figure 5-6(d), (e), and (f), respectively. The appearance of these extra $\{011\}_{\mathrm{TiO_2}}$ facets is often associated with embedded nanoparticles. Assuming a flat growth front that is perpendicular to the axial direction (i.e., $<111>_{\mathrm{TiO_2}}$)—identified as $\{2.4\ 2.4\ 1\}_{\mathrm{TiO_2}}$—this growth front slightly alters its shape due to the presence of additional $\{011\}_{\mathrm{TiO_2}}$ facets, as illustrated by the comparison of planes I and II in Figure 5-7(d-f).

Interestingly, these Au nanoparticles display a new OR, that is close to $<110>_{Au}//<1\bar{2}1>_{TiO_2}$ & $\{1\bar{1}1\}_{Au}//\{10\bar{1}\}_{TiO_2}$, as depicted in the overlapping diffraction patterns in Figure 5-6(f) and Figure 5-4(e). Due to the substantial lattice mismatch between Au and TiO_2, this OR is not among the favorable ones reported for non-embedded Au nanoparticles on rutile substrates or ion-implanted embedded Au nanoparticles [127], [136], [137]. However, with this new OR, the facets required to enclose the Au nanoparticles—two sets of $\{111\}_{Au}$ and one set of $\{100\}_{Au}$—have interplanar spacings and angles that closely match a few TiO_2 low-index planes, specifically the $\{101\}_{TiO_2}$, $\{111\}_{TiO_2}$, and $\{120\}_{TiO_2}$, likely surrounding the embedded nanoparticles.

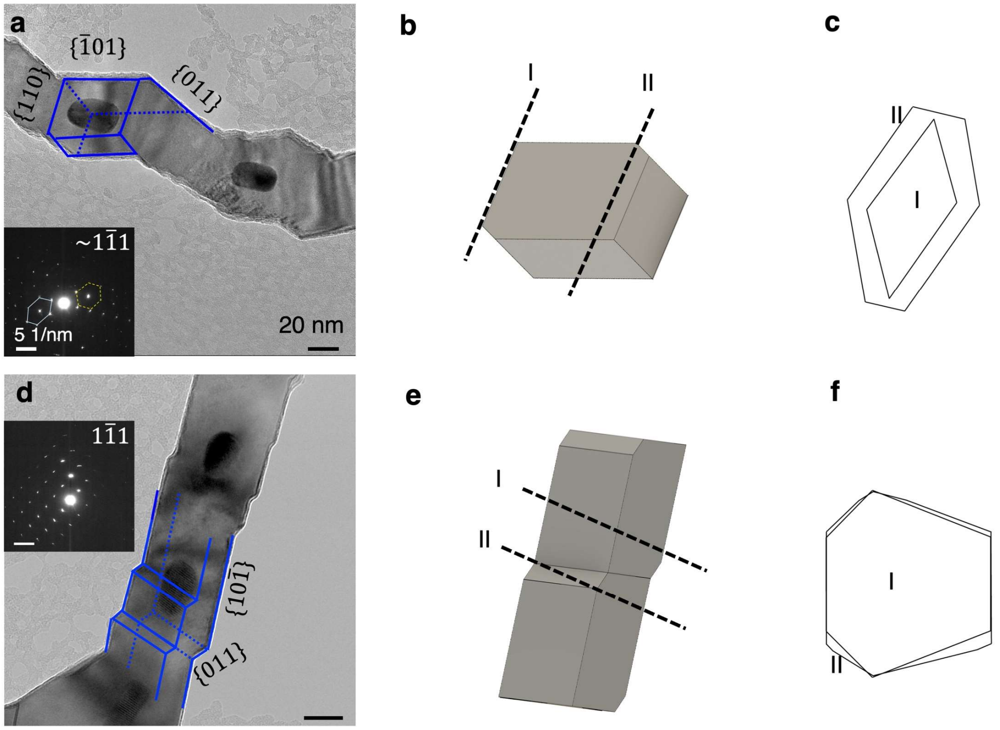

Figure 5-7. TEM bright-field (BF) images of (a) bead-like and (d) prismatic nanowires, along with their corresponding electron diffraction patterns. (b) and (e) 3D models of the bead-like and prismatic nanowires, respectively, with two sectioned regions (I and II) to reveal the imaginary top facets. (c) and (f) top-view schematics display the cross-sectional dimensions in regions I and II. The indexing of the corresponding diffraction patterns is shown in detail in Figure C-1 (Appendix C).

Figure 5-8 presents a randomly shaped nanowire and confirms the commonly observed OR between the Au nanoparticle and TiO_2 nanowire. The nanowire rotates from the $<011>_{TiO_2}$ to approximately $<223>_{TiO_2}$, with the latter displaying $\{1\bar{1}0\}_{TiO}$ facets edge-on. When viewed close to $<223>_{TiO_2}$ as shown in the red square of Figure 5-8, the large, embedded nanoparticle exhibits a $<110>_{Au}$ diffraction pattern, outlined by the yellow dashed line. Consequently, this Au nanoparticle maintains an OR where $<110>_{Au}//<223>_{TiO_2}$ & $\{1\bar{1}1\}_{Au}//\{1\bar{1}0\}_{TiO}$. This finding is consistent with the OR observed in the bead-like nanowires shown in Figure 5-6(c), as well as the most favorable OR reported for this system—paralleling $\{1\bar{1}1\}_{Au}$ to $\{1\bar{1}0\}_{TiO}$ with possible in-plane rotations.

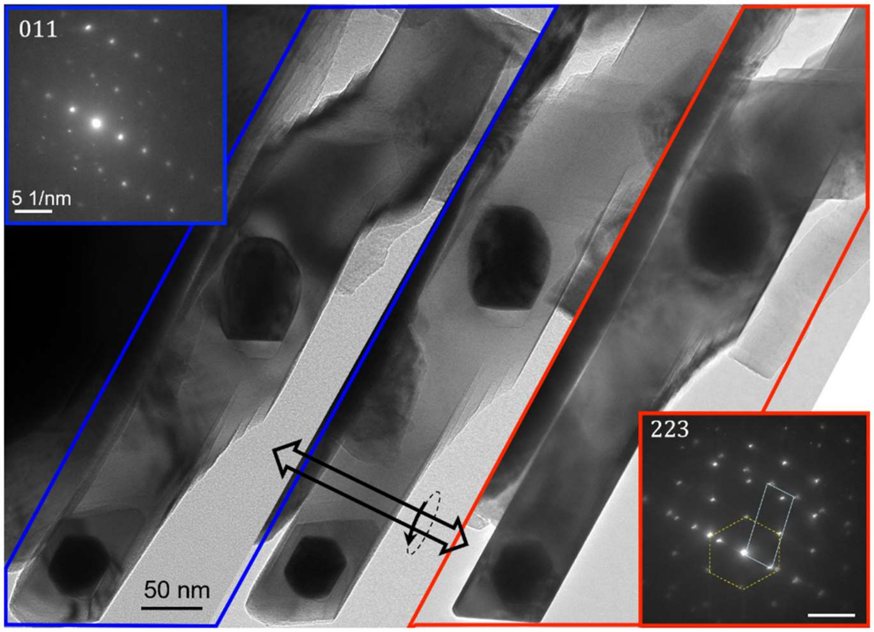

Figure 5-8. TEM bright-field (BF) images of four nanowires from different zone axes, with corresponding electron diffraction patterns. Two embedded nanoparticles of different sizes match varying nanowire dimensions, with a larger nanoparticle showing a $<110>_{Au}$ diffraction pattern (yellow dashed line) in relation to the $\sim<223>_{TiO_2}$ zone. The indexing of the corresponding diffraction patterns is shown in detail in Figure C-1 (Appendix C).

To investigate Au embedded nanoparticles at the growth front, TEM micrographs of representative bead-like and prismatic nanowires are shown in Figure 5-9(a) to (b) and (c)-(d), respectively. A significant reduction in nanowire width underneath the Au seed is expected due to large thermal fluctuations induced during the air-cooling process. This often leads to a change in the axial direction of prismatic nanowires, transitioning from $<111>_{TiO_2}$ to $<110>_{TiO_2}$ beneath the seeds (see Figure 5-10). Figure 5-9(a) to b display one bead-like nanowire from the zone axes of $<1\bar{1}1>_{TiO_2}$ and $<1\bar{1}3>_{TiO_2}$, respectively. The Au nanoparticles maintain an approximate OR with TiO_2, i.e., $<112>_{Au}//<1\bar{1}3>_{TiO_2}$ & $\{1\bar{1}0\}_{Au}//\{110\}_{TiO_2}$, with an offset of around 7° compared to one of the preferred ORs (ORd in ref. [127]). This can be further supported by the moiré fringes visible in the nanoparticle in Figure 5-9(b), which aligns well with those generated by the $\{1\bar{1}0\}_{Au}$-$\{110\}_{TiO_2}$ pair. During the Au nanoparticle embedding, the seed-nanowire interface has a curved morphology, likely consisting of inclined facets, as shown in Figure 5-9(a) to b. This deviates from the previously reported flat growth front, i.e., $\{110\}_{TiO_2}$ [15], without considering the embedding processes.

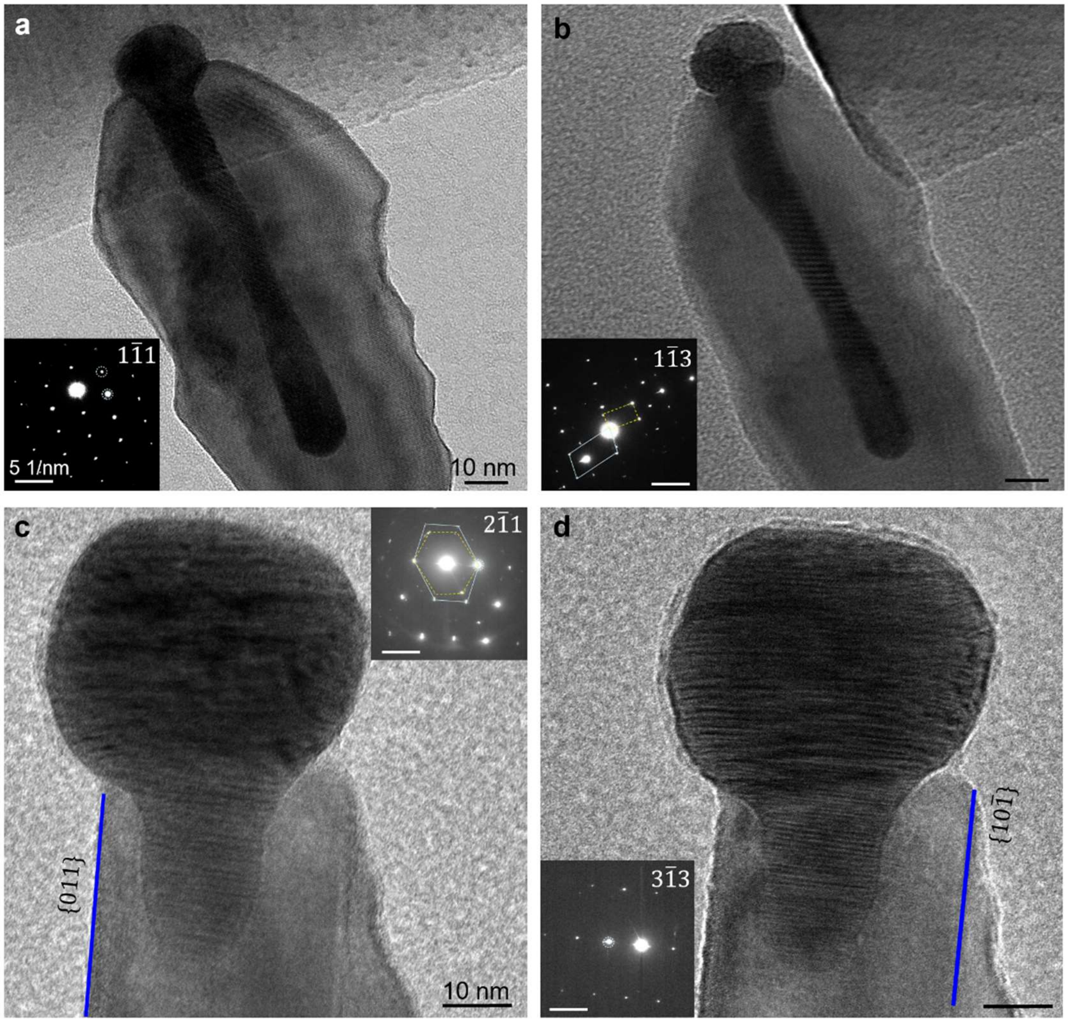

Figure 5-9. TEM -BF images and corresponding diffractions of the growth front: grown along <110> (bead-like, a-b) and grown along $<111>_{TiO_2}$ (c-d). (a) $<110>_{TiO_2}$ nanowire viewed along $<1\bar{1}1>_{TiO_2}$. (b) The same nanowire viewed along $<1\bar{1}3>_{TiO_2}$, highlighted by blue solid lines, with Au viewed along the $<112>_{Au}$ zone axes, shown by the yellow dashed line, indicating an OR of $\sim<112>_{Au}//<1\bar{1}3>_{TiO_2}$ & $\{1\bar{1}0\}_{Au}//\{110\}_{TiO_2}$. (c) $<111>_{TiO_2}$ nanowire viewed along $<2\bar{1}2>_{TiO_2}$, showing $<110>_{Au}$ diffraction pattern in the yellow dashed line and forming the new OR of $\sim<110>_{Au}//<2\bar{1}2>_{TiO_2}$ & $\{1\bar{1}1\}_{Au}//\{101\}_{TiO_2}$. (d) The same nanowire viewed along $<3\bar{1}3>_{TiO_2}$. In each diffraction pattern, the {101} reflections, corresponding to the edge-on side facets, are labelled with dashed circles. In (a-b), a solid yellow circle highlights the most possible growth front. All scale bars are 10 nm in BF images and 5 1/nm for diffraction patterns. The indexing of the corresponding diffraction patterns is shown in detail in Figure C-1 (Appendix C).

Within a prismatic nanowire, an OR of $\sim<110>Au//<2\bar{1}2>_{TiO_2}$ & $\{1\bar{1}1\}_{Au}//\{101\}_{TiO_2}$ is confirmed by the overlapping diffraction inset in Figure 5-9(c).

Although this OR is ~13° offset from the new OR shown in Figure 5-4 and Figure 5-6, it retains the key characteristic, that $\{111\}_{Au}$ is parallel to $\{101\}_{TiO_2}$. Notably, this nanowire grows under an argon pressure of 8,000 Pa, in contrast to the 11 Pa used for other nanowires. Higher argon pressure reduces the growth of nanowire, which helps to preserve the morphology of the growth front during air-cooling processes. Figure 5-9(c) to (d) have a close tangent view of the growth front among the six low-index zone axes accessible within the TEM tilting limits. The curved growth front is clearly evident during the embedding processes. In summary, the embedded Au nanoparticles in bead-like nanowires likely maintain the reported ORs, aligning Au low-index planes with $\{110\}_{TiO_2}$ (i.e., Au/$\{110\}_{TiO_2}$ interfaces), the imaginary growth front. On the other hand, the embedded Au nanoparticles in prismatic nanowires exhibit new ORs, aligning Au low-index planes with $\{101\}_{TiO_2}$. The embedding process is likely associated with a curved growth front.

Figure 5-10 shows a prismatic nanowire growing with Ar pressure of 11Pa, the same as other nanowires except Figure 5-9(c) to (d). Distant from the growth front, the embedded Au nanoparticle shows a new OR of $<001>_{Au}//<31\bar{3}>_{TiO_2}$ & $\{2\bar{2}0\}_{Au}//\{101\}_{TiO_2}$. Similar to the new OR in Figure 5-6(f) and Figure 5-4(e), this OR aligns Au low-index planes, such as $\{110\}_{Au}$ and $\{111\}_{Au}$ to the $\{101\}_{TiO_2}$, differing from previously reported ORs associated with $\{110\}_{TiO_2}$. It is worth noting that the Au nanoparticle also shifts its crystallographic orientation when the nanowire's axial direction changes from $<111>_{TiO_2}$ to $<110>_{TiO_2}$, as indicated by the yellow arrows in Figure 5-10(a) and (b). This can be further supported by the fact that near the seed-nanowire interface, the $\{002\}_{Au}$ is oriented 25° off parallel from the $\{1\bar{1}0\}_{TiO_2}$ as illustrated in Figure 5-10(d). This is incompatible with the new OR described above. During the embedding processes, the curved growth front is also evident in this nanowire.

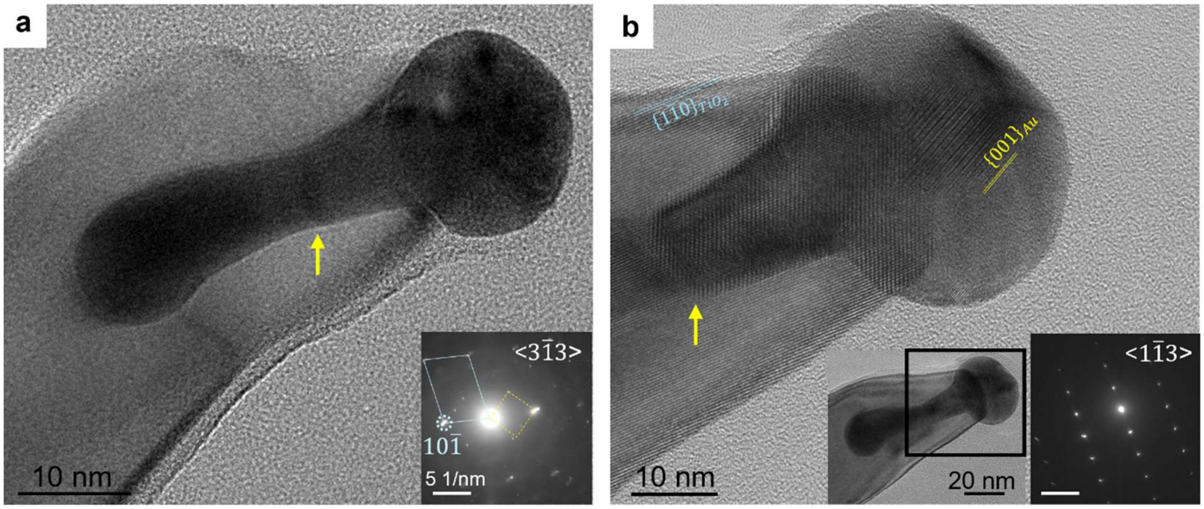

Figure 5-10. (a) Nanowire segment grown along $<111>_{TiO_2}$ (far from the nanowire tip) viewed along $<313>_{TiO_2}$, showing $<110>_{Au}$ diffraction pattern in the yellow dashed line and forming the OR of ~$<001>_{Au}//<31\bar{3}>_{TiO_2}$ & $\{2\bar{2}0\}_{Au}//\{101\}_{TiO_2}$. (b) Nanowire segment grown along $<110>_{TiO_2}$ (close to the nanowire tip) viewed along $<1\bar{1}3>_{TiO_2}$.

Figure 5-11 illustrates a schematic of the mechanism behind the formation of Au nanopeapods in the bead-like (a) and prismatic (b) nanowires. During growth, a small amount of Ni is incorporated into the Au seed at high temperatures, represented by green dots. Ni can alter the preferential Au-TiO_2 interfaces, extending beyond the commonly reported Au/$(110)_{TiO_2}$ interfaces, at both the growth front and embedded nanoparticles. This modification likely occurs because (i) Ni has a stronger affinity for oxygen and interacts more strongly with TiO_2 than Au does, as proved by experimental studies [138], [139], [140] and atomistic simulation [141], and (ii) Ni has a smaller lattice parameter (0.352nm) compared to Au (0.408nm), reducing the lattice mismatch between Au with TiO_2, as better lattice matching can be achieved by slightly compressing the Au lattice at room temperature [127]. Although Au is near their liquid state at the growth temperature (i.e., 1000°C), the changing trends in lattice parameters, or precisely, average atomic distances, with the addition of Ni, are expected to be consistent. Furthermore, the volume thermal expansion coefficient of Au is about four times greater than that of TiO_2, making the reduction in lattice parameters through adding Ni necessary at higher temperatures [142], [143].

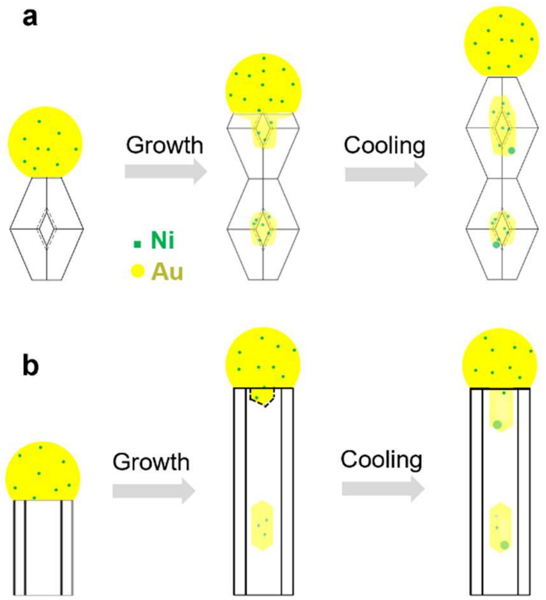

Figure 5-11. Schematic showing the formation of Au-Ni nanoparticles within TiO_2 nanowires with (a) bead-like shape and (b) prismatic shape. During growth, Ni dissolves into the Au seed, affecting Au-TiO_2 interface and possible migration rates, resulting in irregularly shaped nanoparticles in bead-like nanowires and regular facets in prismatic nanowires. (c) Upon cooling, Ni segregates into specific regions of the Au seed and nanoparticles, represented by green dots.

It is reasonable to assume that preferential Au-TiO_2 interfaces, consisting of low-index planes from both lattices, represent low-energy interfaces that migrate more slowly than other interfaces. At the growth front of bead-like nanowires grown along $[110]_{TiO_2}$, the

Au seed is likely to form low-energy interfaces with the TiO_2 nanowires, as predicted by previously reported ORs [36], where a low-index plane of the Au seed aligns parallel to the $[110]_{TiO_2}$ plane. These low-energy interfaces migrate more slowly than other interfaces at the growth front, which may curve assisted by the periodic bead-like morphology, thereby embedding the Au nanoparticles. With the reported ORs, the embedded Au nanoparticle have only one set of low-energy interfaces, i.e., $Au/\{110\}_{TiO_2}$ interface, while the other interfaces involve high-index planes. This likely causes slow migration on one interface and fast migration on the others, leading to irregularly shaped nanoparticles being embedded into the nanowire.

For prismatic nanowires grown along $[111]_{TiO_2}$, the growth front, identified as $\{2.4\ 2.4\ 1\}_{TiO_2}$ if flat, may consist of small segments of $\{111\}_{TiO_2}$ and $\{120\}_{TiO_2}$. These segments can align parallel to $\{111\}_{Au}$ and $\{100\}_{Au}$ planes, forming low-energy interfaces that have slow migration rates. As the Au nanoparticles start to sink into the nanowire, additional $\{111\}_{Au}$ align with $\{101\}_{TiO_2}$ creating another set of low-energy interfaces that further facilitate this embedding process. This results in well-defined shape of the embedded nanoparticles, which agrees well with the observed morphology and the newly discovered Au-TiO_2 OR in Figure 5-4(e), Figure 5-6(f), and Figure 5-9. Notably, a slight expansion in Au lattice helps mitigate the lattice mismatch since the interplanar spacings of $\{111\}_{Au}$ and $\{101\}_{TiO_2}$ are 0.235nm and 0.249nm at room temperature, respectively. At higher temperatures, this condition is achievable even with Ni solutes in the Au lattice because Au has larger thermal expansion coefficient than TiO_2. During cooling to room temperature, the removal of Ni from the Au lattice is favorable since Ni will reduce the lattice parameter of embedded nanoparticles. This is consistent with EDX maps in Figure

5-4, where a diminished Ni signals in embedded Au nanoparticles within prismatic nanowires compared to bead-like ones. A change in the growth cross-section may facilitate the formation of embedded nanoparticles, as it energetically allows for the induction of new Au-TiO_2 interfaces that can compensate for the energy changes caused by the inclined facets of the nanowires and the surface curvature variations of the seed [20]. Table 5-1 provides a summary of the key characteristics observed in bead-like and prismatic nanowires, enhancing the clarity of the narrative.

Table 5-1. Overview of the characteristics observed in bead-like and prismatic nanowires.

Nanowire types	**Bead-like nanowires**	**Prismatic nanowires**
Axial directions	Along $[110]_{TiO_2}$, vertical to the substrate	Along $<111>_{TiO_2}$, inclined at ~65.51° to the substrate
Side facets	Bounded by two $\{1\bar{1}0\}_{TiO_2}$ facets and eight $\{101\}_{TiO_2}$ facets	Bounded by two $\{1\bar{1}0\}_{TiO_2}$ and four $\{10\bar{1}\}_{TiO_2}$ parallel facets, probably with trivial $\{011\}_{TiO_2}$ facets
Growth front oscillation	Significant oscillation by transiting between rhombohedral shape to hexagonal shape	No oscillation or minor ones influenced by trivial $\{011\}_{TiO_2}$ facets
Au-TiO_2 orientation relationships (ORs)	Previously reported ORs, aligning Au low-index planes with $\{110\}_{TiO_2}$	Novel ORs, aligning Au low-index planes with $\{101\}_{TiO_2}$
Embedded nanoparticles morphology	Particles lack well-defined polygonal shapes	Particles exhibit well-defined polygonal shapes
Embedded nanoparticles composition	Limited phase separation upon cooling	Ni segregation upon cooling

5.4. Summary

In this paper, we reported the endotaxial growth of embedded Au nanoparticles within TiO_2 nanowires by introducing small amounts of Ni into the Au seed. A different orientation relationship between Au and TiO_2 and the corresponding changes in the preferential Au-TiO_2 interface are observed in this case. This corresponds to the embedding of Au nanoparticles within the nanowires, with distinct morphologies depending on the axial direction: irregularly shaped nanoparticles in bead-like nanowires grown along $[110]_{TiO_2}$, and well-faceted nanoparticles in prismatic nanowires grown along $<111>_{TiO_2}$. The observed endotaxial embedding growth is closely associated to the new orientation relationship between Au and TiO_2. These findings highlight the critical role of seed composition and interface energetics in controlling vapor-phase growth dynamics of nanowires, emphasizing the importance of crystallographic factors.

Chapter 6

Spectroscopic Insights into Controlling Sidewall Faceting of TiO_2 Nanowires via Au-Ag Bimetallic Seeds

In this chapter, we investigate how Au-Ag bimetallic seeds and their compositional heterogeneity—particularly Ag segregation—affect the morphology of TiO_2 nanowires. Section 6.1 presents transmission electron microscopy (TEM) results, including a three-dimensional reconstruction that reveals Ag-rich domains near the growth front. Section 6.2 describes X-ray absorption spectroscopy (XAS) analyses, which probe the seed composition and local chemical environment of Au and Ag. Although the absorbed growth species at Au-Ag bimetallic seeds likely exhibit variations in the local compositions and bonding configurations, the bonding characteristics, especially within the first-nearest neighbors, often closely resemble those observed in stable crystalline phases [144], [145], [146]. Thus, atomic models from crystallographic databases are used to qualitatively interpret the obtained XAS spectra. Through this combined structural and spectroscopic approach, we aim to understand how seed composition influences nanowire growth direction and sidewall faceting, contributing to the broader goal of achieving controlled and tunable oxide nanowire synthesis.

6.1. 3D Configuration of Ag-rich Domains at the Growth Front

Nanowires often contain segments with two distinct morphologies: a <111>-grown segments with prismatic shape and a <110>-grown segments with bead-like shape, as shown in Figure 6-1(a) and (b), respectively. In a controlled set of nanowires, growth occurs exclusively along $<110>_{TiO_2}$ with bead-like morphology underneath pure Au seeds, consistent with previous reports [30], [116]. Both prismatic and bead-like segments are enclosed by $\{10\bar{1}\}_{TiO_2}$ and $\{1\bar{1}0\}_{TiO_2}$ side facets, labelled in light and dark blue, respectively, in the inserted nanowire schematics. The seeds are consistently covered by thin layers of a few nm in thickness (as shown in the insets I and II in Figure 6-1), mainly composed of Ti and O. According to previous studies [116], the vapor growth species, are absorbed onto the seeds and then subsequently transported to the growth front to facilitate nanowire growth. Although oxide vaporization is limited at current temperatures, several observations indicate that the adsorbate is TiO_x: metallic Ti is unstable under the oxidizing conditions; almost no nanowires form when the vessel is open; and adding carbon powder—which reduces TiO_x to Ti—suppresses nanowire growth. TiO_x adsorption is energetically favorable because the Au–rutile interfacial energy (~0.5 J m^{-2}) is lower than the surface energy of bare Au, causing TiO_x species to wet and stabilize the seeds [116]. Additionally, the Au-Ag bimetallic seeds are often not perfect spherical because they typically contain Au-rich and Ag-rich domains, as demonstrated by the corresponding EDX compositional maps in Figure 6-2(a) and Figure 6-3. Notably, Ag-rich domains were consistently observed at the surface, with no central Ag enrichment detected across more than 30 nanowires. The existence of distinct Ag-rich and Au-rich domains deviates from the Ag-Au isomorphous phase diagram, which predicts complete solubility of Ag and Au in both solid and liquid states. This suggests that the segregation of Ag and Au may be influenced by the adsorption of growth species on the seed. In agreement with previous reports [59], [116], Ag-rich domains are in contact with the growth front on top of prismatic segments, whereas Ag-rich domains are positioned away from the growth front for bead-like segments.

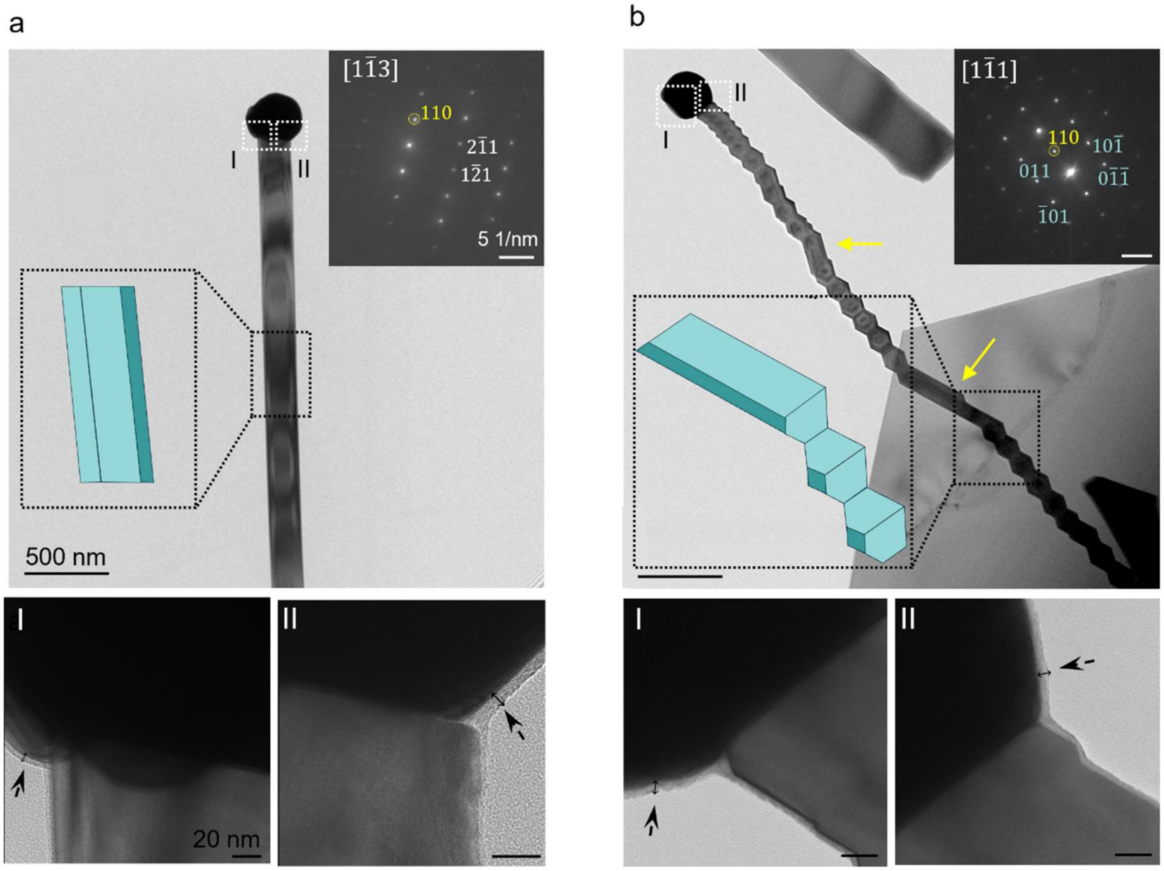

Figure 6-1. Transmission electron microscopy-bright-field (TEM-BF) images of (a) a long $<111>_{TiO_2}$-grown prismatic segment, viewed along $[1\bar{1}3]_{TiO_2}$, and (b) a $<110>_{TiO_2}$-grown bead-like segment, viewed along $[1\bar{1}1]_{TiO_2}$, which contains small prismatic segments, labelled by yellow arrows. Insets are the three-dimensional (3D) schematics illustrating the side facets of nanowires, where $\{10\bar{1}\}_{TiO_2}$ and $\{1\bar{1}0\}_{TiO_2}$ side facets are labelled by light and dark blue, respectively. The images labeled (I) and (II) provide higher-magnification views of the region around the growth front and the outer layer surrounding the seed, extracted from the highlighted squares in (a) and (b), respectively. Yellow and cyan indices in the diffraction patterns indicate the top and side facets, respectively.

Figure 6-3 presents EDS compositional maps for bead-like nanowires, highlighting the Au-rich and Ag-rich domains. The Ag-rich domain in these structures is located away from the growth front. Representative EDS spectra for both Au-rich and Ag-rich domains are provided in Figure 6-4. Quantitative EDS results of 10 nanowires, summarized in Table 6-1, show that the Au-rich domains contain approximately ~91-96 at.% Au and 4-9 at.% Ag, whereas the Ag-rich regions contain about 20–33 at.% Au and 67–80 at.% Ag.

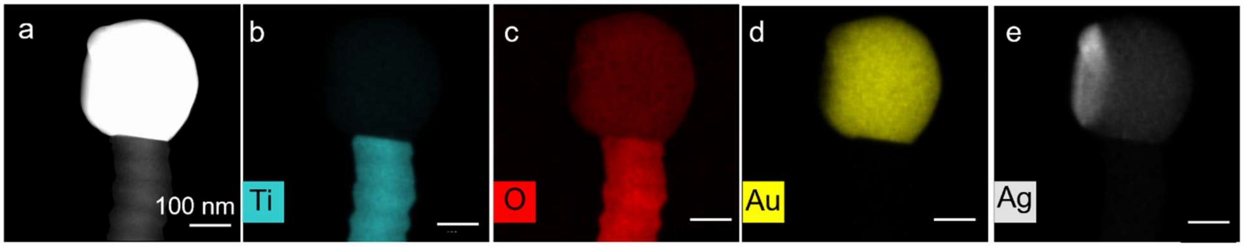

Figure 6-2. High-angle annular dark field (HAADF) image along with Ti, O, Au, and Ag EDX elemental mapping of the bead-like nanowire. Ag-rich segregation is located away from the seed-nanowire interface, contributing to the bead-like morphology of the nanowire.

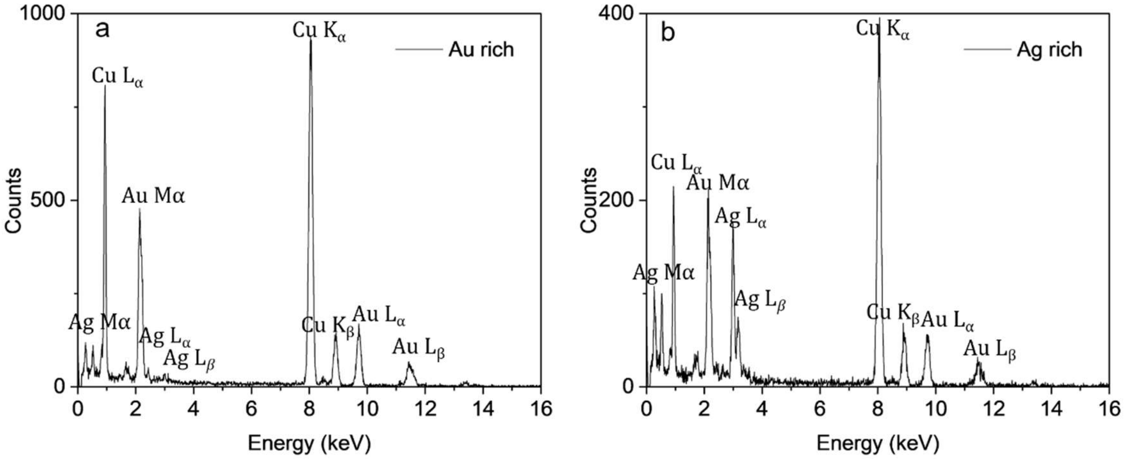

Figure 6-3. Energy dispersive X-ray (EDX) spectra of TiO_2 nanowires with an Au-Ag seed, showing (a) an Au-rich region and (b) an Ag-rich region.

Table 6-1. Chemical compositions of the Au-rich and Ag-rich regions in a few seeds. EDX signals for quantification were obtained from the central areas of the Au-rich and Ag-rich regions, selected using polygonal tools available in the EDX software.

Sample	**Au rich domain**		**Ag rich domain**	
	Au (at.%)	Ag (at.%)	Au (at.%)	Ag (at.%)
NW 1	94	6	26	74
NW 2	93	7	27	73

NW 3	96	4	33	67
NW 4	94	6	30	70
NW 5	93	7	26	74
NW 6	93	7	26	74
NW 7	96	4	29	71
NW 8	93	7	31	69
NW 9	96	4	26	74
NW 10	90	9	23	77

To pinpoint the three-dimensional configuration of Ag-rich domains at the growth front, we analyzed >20 nanowires, each along different zone axes, with four representative examples shown in Figure 6-4(a-d). The growth front, marked in yellow in Figure 6-4, corresponds to $\{1\bar{1}0\}_{\mathrm{TiO_2}}$ for both <110>-grown bead-like and <111>-grown prismatic nanowires. Additionally, the growth front periodically alternates between hexagonal and rhombohedral cross-sections in bead-like segments, while maintaining a hexagonal cross-section in prismatic segments. Figure 6-4(a) and (b) depict typical prismatic segments, exhibiting the hexagonal cross-sectional growth front. Ag-rich domains remain consistently located at the corner between the $\{10\bar{1}\}_{\mathrm{TiO_2}}$ and $\{1\bar{1}0\}_{\mathrm{TiO_2}}$ side facets for prismatic segments, as highlighted by the black circles. Figure 6-4(c) and (d) capture transitions from prismatic to bead-like segments, which were rarely observed. Ag-rich domains either gradually move away from the growth front in Figure 6-4(c) with a rhombohedral growth front, or flow toward the corner between $\{10\bar{1}\}_{\mathrm{TiO_2}}$ facets, as shown in Figure 6-4(d) with a hexagonal growth front.

Previous study [30] suggested that nucleation preferentially occurs at the corner between $\{10\bar{1}\}_{\mathrm{TiO_2}}$ facets, the common corner of both hexagonal and rhombohedral growth fronts, followed by the lateral propagation across the growth front, in bead-like nanowires with pure Au seeds. The Au-Ag seeds are not homogenous as pure Au seeds because they likely contain distinct Au-rich and Ag-rich domains. However, the above conclusions remain valid as long as Ag-rich domains are distant from the growth front, as shown in Figure 6-4(c) and Figure 6-2. When the Ag-rich domain migrates towards the corner between $\{10\bar{1}\}_{\mathrm{TiO_2}}$ facets, asymmetric bead-like growth, only underneath the Ag-rich domain, is facilitated (as suggested in Figure 6-4(d)), assuming Ag-rich domains can significantly promote nucleation. If so, Ag-rich domains promote nucleation at the junction between the $\{10\bar{1}\}_{\mathrm{TiO_2}}$ and $\{1\bar{1}0\}_{\mathrm{TiO_2}}$ side facets, maintaining a hexagonal growth front for prismatic nanowires, as shown in Figure 6-4(a) and (b). This assumption is reasonable given that Ag has a stronger bonding affinity to O compared to Au, which can be essential in transporting O-containing growth species to the growth front.

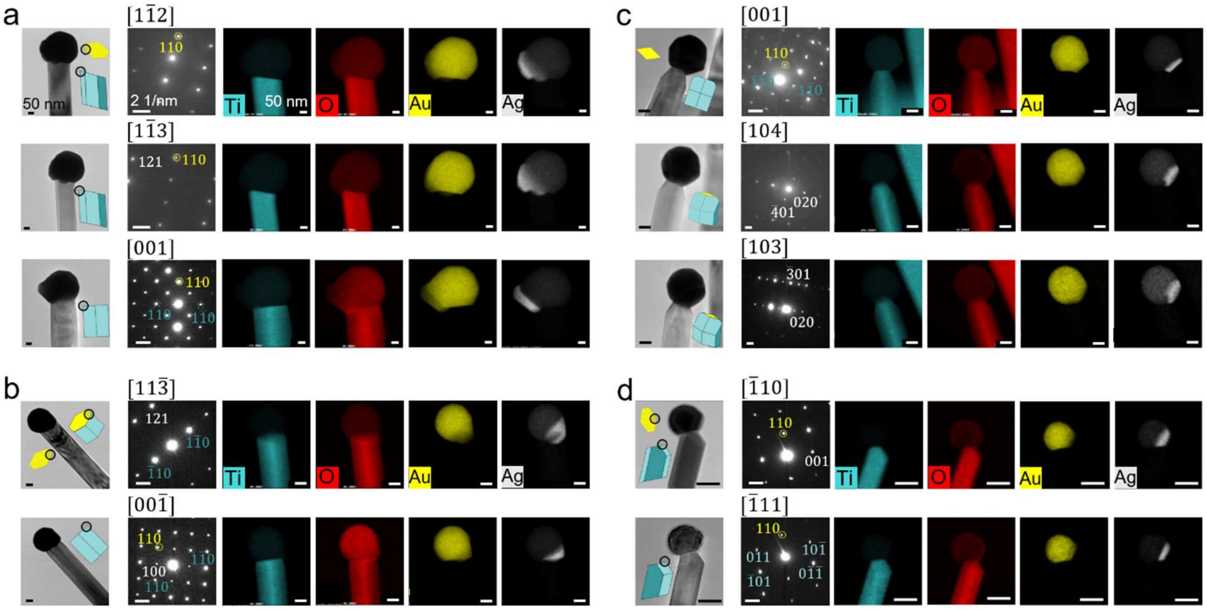

Figure 6-4. EDX elemental mapping of Ti, O, Au, and Ag for four typical nanowires, each examined from different zone axes to reconstruct the three-dimensional composition configurations at the growth front. The inset includes the nanowire schematic viewed along with the corresponding

zone axis and the schematic of the growth front, with the black circles marking the location of Ag-rich domains. $\{10\bar{1}\}_{TiO_2}$ and $\{1\bar{1}0\}_{TiO_2}$ side facets are labelled by light and dark cyan, respectively. The top $\{110\}$ facet and the $\{1\bar{1}0\}$ side facets in the diffraction patterns are also highlighted in yellow and cyan, respectively.

6.2. X-ray Spectroscopic Insights of the Bonding Environment at the Seeds

To investigate the local atomic environment and bonding at the seeds, XAS analysis was conducted on nanowires grown with Au-Ag seeds and pure Au seed (as the control). Figure 6-5(a) and (b) show the Au L_3-edge XAS spectra in pure Au and Au-Ag seeds, respectively, while Figure 6-5(c) presents the Ag K-edge spectrum for the Au-Ag seed. The XANES, extending approximately 50–100 eV above the edge to cover the specific features at lower energies, and EXAFS region, beyond 100 eV, are highlighted. Additionally, overlapped XANES and EXAFS spectra with both Au and Ag foils are provided on the left and right graphs, respectively. Note that the Au spectrum in Figure 6-5(a) was collected by Minghui Lin; however, the data analysis and comparison were performed by the author.

Four near-edge peaks, A−D, are labeled in the Au XANES L_3-edge spectra in Figure 6-5(i). Compared to Au foil, both pure Au and Au-Ag seeds have a pronounced difference in the shape and position of peak A and a slight blueshift in peaks B-D. Comparable spectral changes have been reported in Au/TiO_2 (rutile [147], [148] and/or anatase [147]) nanocatalysts, where Au nanoparticles were encapsulated by TiO_x overlayers, considering similar uncertainties in their local environment. Notably, the white line intensity (associated with peak A), which corresponds to the d-orbital occupancy (i.e., the charge states) of Au, remains a topic of debate regarding the extent of charge transfer between Au and TiO_2, in different nanocatalysts [147], [148] and may not be directly align with the present spectra due to the lack of normalization details in these previous reports.

When comparing Au L_3-edge spectra of pure Au and Au-Ag seeds (Figure 6-5(i)), peak A exhibits slight variation in shape while peaks B-D show subtle broadening and blueshifts, suggesting a minor modification of the electronic states of Au due to Ag incorporation. Similar changes in peak A for Au-Ag core-shell structure [149], [150] and subtle blueshifts in Ag-Au nanoclusters [151] have been attributed to the d-electron transfer from Au to Ag. As shown in Figure 6-5(ii), Ag L_3-edge spectrum of Au-Ag seeds exhibits broadened and blueshifted peaks, as compared to the Ag foil. Significant spectral changes observed here are consistent with previous studies on Ag/TiO_2 and Ag-Au/TiO_2 nanocatalysts [152], as a result of the presence of oxidized silver on TiO_2, in addition to the subtle spectral changes caused by alloying with Au [152], [153].

The k^2-weighted $\chi(k)$ spectra in Figure 6-5(iii), (iv) and the corresponding Fourier Transform (FT) of the k^2-weighted EXAFS in Figure 6-5(v), (vi) are presented to analyze the EXAFS oscillations at higher energies. The $\chi(k)$ spectra for Au L_3-edge (Figure 6-5(iii)) exhibit a clear phase shift toward higher k-values (above 7 $Å^{-1}$) from the Au foil to the pure Au seed, and further to the Au-Ag seed. Additionally, a slight increase in intensity is observed for the Au-Ag seed compared to the pure Au. This phase shift has been reported in Au-Ag nanoparticles [154], [155] and is attributed to an increased number of Ag neighbors surrounding the absorbing Au atom.

In the FT spectra for Au L_3-edge (Figure 6-5(v)), the main scattering peak for Au foil at ~2.4 eV, corresponding to the first coordination shell, shifts to lower R-values to

~2.3 eV in the pure Au seed, and further to ~2.28 eV in the Au-Ag seed, with a gradual increase in intensity. This reduction in bond length and increase in FT intensity are attributed to interactions between Au (or Au-Ag) and TiO_x species, as supported by previous EXAFS studies on Au/TiO_2 systems [156]. The intensity of the main scattering peak increases in the Au-Ag seed, consistent with previous reports [154], is attributed to the Au-Ag coordination. The appearance of a double peak in the first shell region can be explained by the interference between Au–Au and Au–Ag backscattering paths, which differ in both phase and amplitude.

For Ag k-edge, k^2-weighted $\chi(k)$ spectra in Figure 6-5(iv) and FT of the k^2-weighted EXAFS in Figure 6-5(vi) show a greater intensity in Au-Ag seed compared to Ag foil while less pronounced phase shift is detected compared to Au L_3 edge in Figure 6-5(iii) and (v). This can be attributed to the surrounding TiO_x and/or Au around Ag atoms in Au-Ag seed and consequently increased coordination number as reported in.[157]. A recognizable peak near 1.9 Å, also present in Ag foil, may partially arise from short-range Ag–Ag interactions, but in the Au–Ag sample, it could also reflect Ag–O coordination as reported for oxidized Ag species [158].

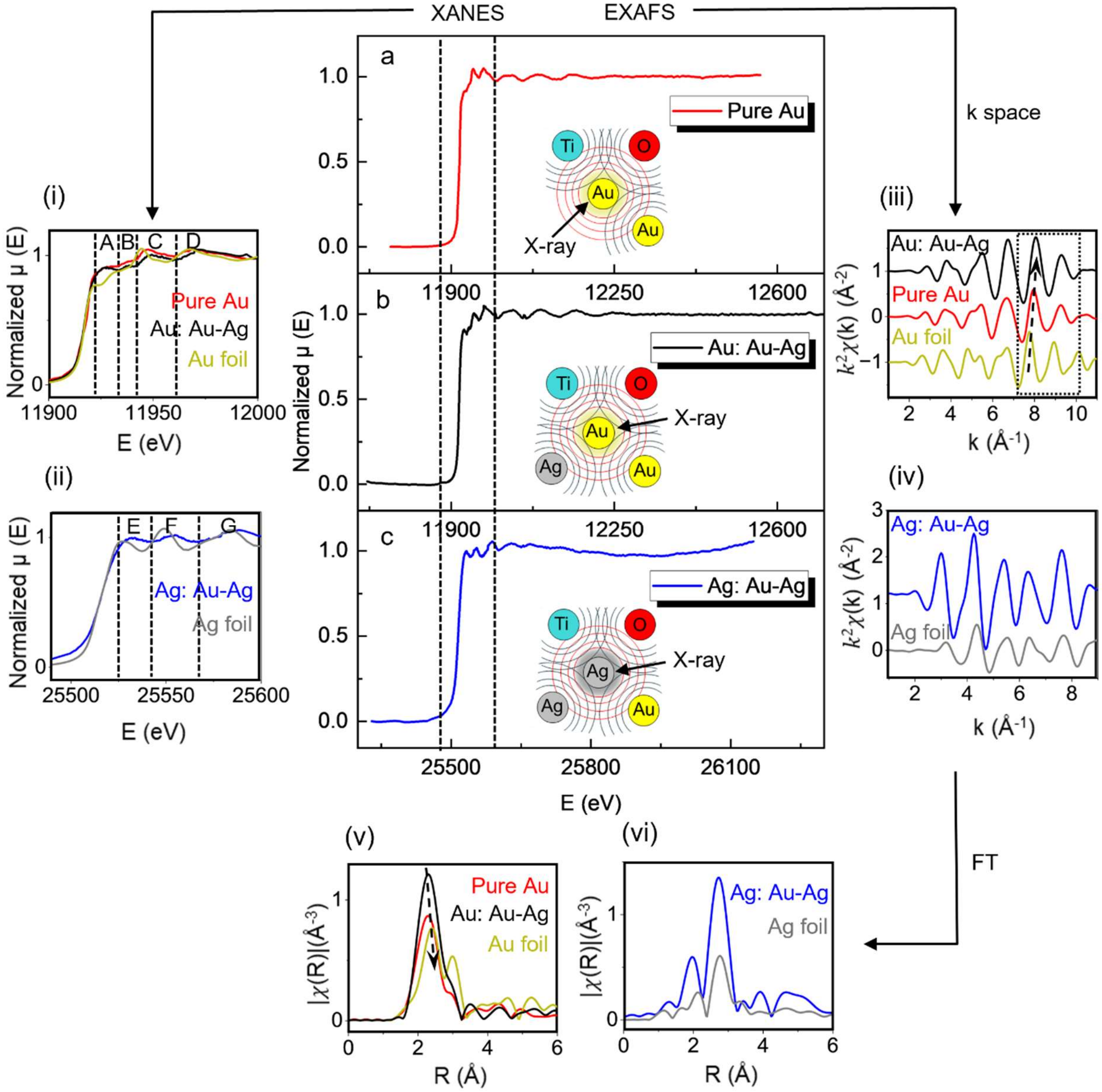

Figure 6-5. Experimental X-ray absorption spectroscopy (XAS) data comprising: (a) Au L_3-edge spectrum for the pure Au seed, (b) Au L_3-edge spectrum for the Au-Ag seed, and (c) Ag K-edge spectrum for the Au-Ag seed. Insets in a, b, and c illustrate schematic models of the photoelectron scattering paths, indicating potential neighboring atoms in each case.

(i) The Au L_3-edge XANES spectra of pure Au, the Au-Ag seed, and bulk Au foil (as a reference), showing four distinct peaks labeled A, B, C, and D.

(ii) The Ag K-edge XANES spectra for Ag foil (reference) and the Au-Ag seed, displaying three primary peaks marked E, F, and G.

(iii) and (iv) display the k^2-weighted $\chi(k)$ spectra for the Au L_3-edge and Ag K-edge, respectively, with a notable phase shift at higher k-values (above 7 Å^{-1}) observed from Au foil to pure Au and further to the Au-Ag seed.

(v) and (vi) present the Fourier transforms of the k^2-weighted EXAFS spectra for the Au L_3-edge and Ag K-edge, respectively. In (v), an arrow highlights both a phase shift and a reduction in intensity for the Au L_3-edge.

To further interpret XAS spectra, simulated spectra based on representative atomic structures (Table 3-4 and Table 3-5in chapter 3) were applied to construct experimental XANES spectra. While the adsorbed growth species on the Au–Ag bimetallic seeds may vary in local composition and bonding configuration, their bonding characteristics—particularly among first-nearest neighbors—often closely resemble those found in stable crystalline phases [144], [145], [146]. The simulated XANES spectra for all proposed atomic models are shown in Figure 3-13of chapter 3. To assess the reliability of the Au–Ag models within Au-rich and Ag-rich domains, we compared their simulated spectra against that of pure Au foil in Figure 6-6(a), (b). The slight blueshift observed in peaks A–D of the Au spectra and peaks E–G of the Ag spectra for the experimental Au–Ag seed—relative to the pure Au seed and Au foil in Figure 6-5(i), (ii)—is further supported by comparisons with the simulated spectra of the Au-rich and Ag-rich models (see Figure 6-6(a), (b)). The best-fit models, with R factor of <0.002, are displayed at the top of Figure 6-7(a, b, c) and summarized in Table 6-2.

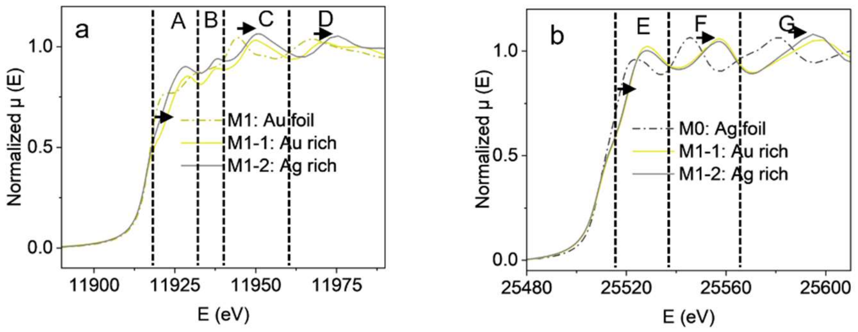

Figure 6-6. (a) Comparison of Au L3-edge in Au foil (M1), Au in Au-rich model (M1-1), and Au in Ag-rich model (M1-2). (b) Comparison of Ag k-edge in Ag foil (M0), Ag in Au-rich model (M1-1), and Ag in Ag-rich model (M1-2).

In pure Au seeds, metallic Au (M1) is the dominant component, accounting for 86% of the total weight, while Au-Ti models (M4 & M5) contribute the remaining 14%. Evidence for bonding characteristics among first-nearest Au–Ti neighbors is further supported by the Ti K-edge XAS spectrum, as shown in Figure 6-8, which compares the Ti K-edge XAS spectrum collected at the seed region of the current pure-Au sample (black line) with those of rutile TiO$_2$ [159] (blue line), AuTi$_3$ (purple line), and Ti foil (green line) [160], [161]. The pre-peak at 4966 eV and 4970 eV, resembling the feature of AuTi$_3$ spectra. The pre-edge peaks, however, are commonly observed in rutile TiO$_2$, at around 4969 eV and 4973 eV [162], [163]. As the AuTi$_3$ spectrum is only available over a limited energy range, further analysis is constrained.

In Au-Ag seeds, the major contributors are the Au-rich solution (M1-1, 76% by weight) and Ag-rich solutions (M1-2, 16%). Notably, the inclusion of Au-O models results in poorer fitting for both pure Au and Au-Ag seeds, suggesting that Au-O bonding of (long-ranged ordered) Au$_2$O$_3$ type is beyond the XANES resolution. On the other hand, Ag-rich solution (M1-2, 40%) dominates Ag spectra of Au-Ag seeds, followed by Au-rich solution

(M1-1, 4%), and Ag-Ti (M7, 38%), and Ag-O (M9 & 11, 16%). Adding Ag-O model significantly improves fitting, suggesting possible Ag-O bonding. The LCF fitting results suggest that Ag likely adopts a distorted octahedral coordination as for Ag_3O_4 (M11) and a tetrahedral geometry as for AgO (M9).

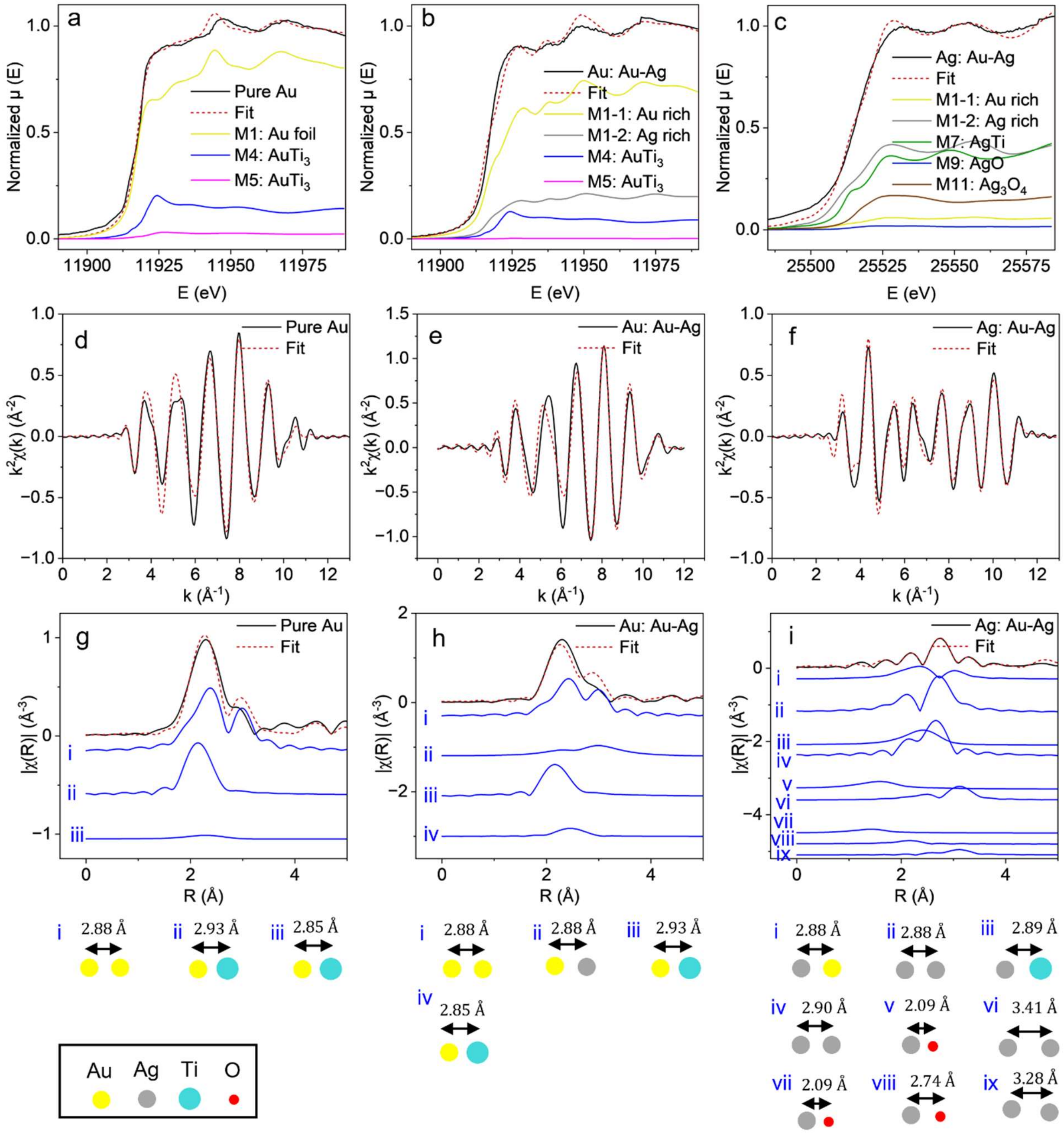

Figure 6-7. XANES-LCF and EXAFS R/k space fitting results for Au L$_3$ edge and Ag K edge absorbers in pure Au and Au-Ag seeds. (a, b, c) present the LCF fitting results, showing the best fit derived from all possible theoretical models that reconstruct the experimental spectra. (d, e, f) display the k-space fitting of the Au L$_3$ edge and Ag K edge for pure Au, Au absorber in Au-Ag seed, and Ag absorber in Au-Ag seed. (g, h, i) illustrate the Fourier-transformed (FT) EXAFS spectra for the Au L$_3$ and Ag K edges in pure Au and Au-Ag seeds, along with the contributions of the most significant photoelectron scattering paths between 1st nearest neighbors (1st shell), with their geometries depicted in the lower panels.

Table 6-2. Linear Combination Analysis (LCA) best fitting results for Au absorber in both pure Au and Au-Ag seed, as well as Ag absorber in the Au-Ag seed.

Parameter	**Au absorber in pure Au**		**Au absorber in Au-Ag**		**Ag absorber in Au-Ag**	
	Best fit value	Standard error	Best fit value	Standard error	Best fit value	Standard error
E0 shift	**-0.023**	0.014	**-0.845**	0.083	**0.846**	0.018
M1: Au foil	**0.862**	0.010	---	---	---	---
M1-1: Au rich	---	---	**0.760**	0.023	**0.050**	0.010
M1-2: Ag rich	---	---	**0.160**	0.013	**0.406**	0.021
M2: AuTi	---	---	---	---	---	---
M3: AuTi	---	---	---	---	---	---
M4: $AuTi_3$	**0.104**	0.020	**0.069**	0.021	---	---
M5: $AuTi_3$	**0.033**	0.010	**0.011**	0.010	---	---
M6: Au_2O_3	---	---	---	---	---	---
M7: AgTi	---	---	---	---	**0.385**	0.018
M8: $AgTi_3$	---	---	---	---	---	---
M9: AgO	---	---	---	---	**0.015**	0.011
M10: Ag_2O_3	---	---	---	---	---	---
M11: Ag_3O_4	---	---	---	---	**0.144**	0.012
M12: Ag_2O	---	---	---	---	---	---
Total	**1.000**	0	**1.000**	0	**1.000**	0
R factor	**0.0002**	---	**0.001**	---	**0.001**	---
χ^2_{reduced}	**0.0001**	---	**0.0008**	---	**0.0009**	---

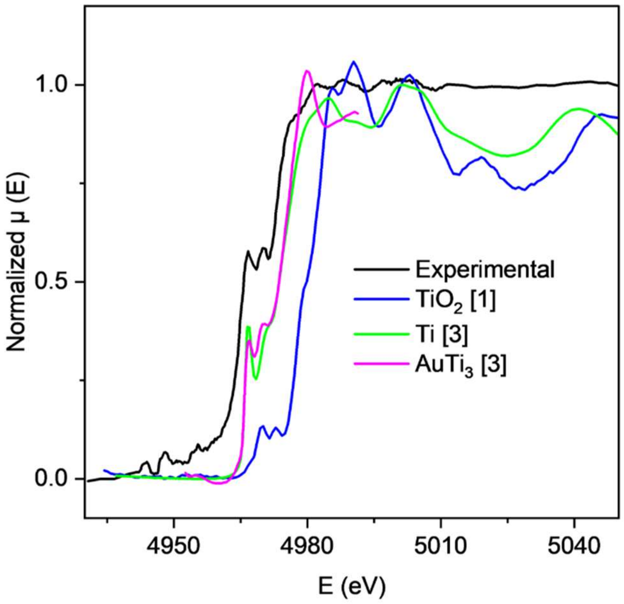

Figure 6-8. Ti K-edge XAS spectra of the TiO_2 nanowire sample (black line) compared with rutile TiO_2 (blue line, Ref. [159]), elemental Ti (green line, Ref. [161]), and $AuTi_3$ (purple, Ref. [161]).

The relative volumes of Au-rich and Ag-rich domains were estimated by dividing the XANES-fitted elemental weights by the corresponding atomic percentages from EDX. For Au spectra, fitted weights of 76% (Au-rich) and 16% (Ag-rich), with atomic fractions of 94% and 30% (Table 6-1), yield volume estimates of 0.81 (Au-rich domain) and 0.53 (Ag-rich domain). For Ag, fitted weights of 5% (Au-rich) and 41% (Ag-rich), with atomic fractions of 6% and 70% (Table 6-1), give volumes of 0.83 (Au-rich) and 0.58 (Ag-rich). The close match between Au and Ag cases further supports the validity of the fitting.

To address potential discrepancies between the experimental and simulated spectra of Au-Ag solutions, the experimental spectra of Au foil and Ag foil were applied as substitutes for Au-rich solution in fitting the Au spectra and Ag-rich solution in fitting the Ag spectrum. (Detailed in Figure 6-9 and Table 6-3). It is important to note that the weights of atomic models considering growth species are similar, with 10% Au-Ti (M4 & M5) in the Au L3-edge spectrum as well as 35% Ag-Ti (M7) and 11% Ag-O (M9 & M11) in the

Ag K-edge spectrum. However, lower contributions from Au foil (M1, 69%) and Ag foil (M0, 39%), are reasonable, as these models tend to overestimate the actual Au concentration in the Au-rich domain and Ag concentration in the Ag-rich domain, respectively. The R-factors and standard errors for the calculated model weights, using Au foil and Ag foil, are higher, suggesting a poorer fitting using Au and Ag experimental spectra.

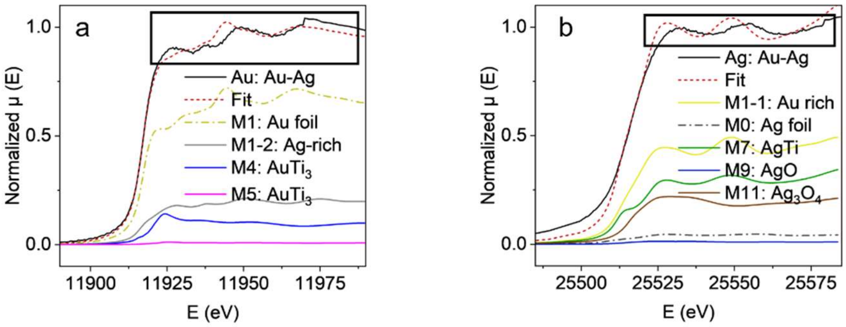

Figure 6-9. LCF fitting of the experimental XANES spectrum using (c) pure Au foil (M1) and (d) pure Ag foil (M0) as substitutes for the Au-rich and Ag-rich models, respectively. The XANES spectra include the experimental sample (black solid line), the best fit obtained through LCF (red dashed line), and contributions from M1, M1-2, M4, and M5 for the Au case, as well as M1-3, M0, M7, M9, and M11 for the Ag case. The black square highlights the discrepancy between experimental data and the fit.

Table 6-3. Fitting parameters for the best-fit combination in LCF for Au L$_3$-edge and Ag K-edge absorbers, using M1 (Au foil) and M0 (Ag foil) as substitutes for the Au-rich and Ag-rich models, respectively (highlighted in red).

Parameter	**Au absorber in Au-Ag**		**Ag absorber in Au-Ag**	
	Best fit value	Standard error	Best fit value	Standard error
E0 shift	**-0.313**	0.075	**0.215**	0.082
M1: Au foil	**0.690**	0.108	---	---
M1-2: Au in Ag rich	**0.200**	0.102	**---**	---
M0: Ag foil	---	---	**0.395**	0.153
M1-1: Ag in Au rich	**---**	----	**0.045**	0.017
M2: AuTi	**---**	**---**	----	**---**
M3: AuTi	**---**	----	**---**	----

M4: $AuTi_3$	**0.089**	0.023	---	---
M5: $AuTi_3$	**0.008**	0.015	---	---
M6: Au_2O_3	---	---	---	---
M7: AgTi	---	---	**0.342**	0.044
M8: $AgTi_3$	---	---	---	---
M9: AgO	---	---	**0.012**	0.023
M10: Ag_2O_3	---	---	---	---
M11: Ag_3O_4	---	---	**0.189**	0.017
M12: Ag_2O	---	---	---	---
Total	**0.987**	0.064	**0.983**	0.033
R factor	**0.0009**	---	**0.001**	---
χ^2_{reduced}	**0.0006**	---	**0.0014**	---

In addition, a k^2-weighting factor was applied to $\chi(k)$, and EXAFS fitting was conducted in both k-space (Figure 6-7d, e, f) and R-space within a 6 Å radius (Figure 6-7g, h, i). To further evaluate the phase shifts and overall fit quality, the real part of the Fourier-transformed EXAFS signal ($\mathrm{Re}[\chi(R)]$) is presented in Figure 6-10(a, b, c) for the pure Au seed, Au in Au-Ag seed, and Ag in Au-Ag seed, respectively. The close agreement between the experimental and fitted $\mathrm{Re}[\chi(R)]$ curves in all three cases indicates minimal or no phase shift, confirming the reliability and quality of the fitting. This supports the structural parameters extracted from the EXAFS analysis and demonstrates that the proposed models capture the key features of the local environment around the absorber atoms. All single-scattering paths derived from Feff modeling for the first shell are illustrated as the blue curves and corresponding atomic schematics in the lower panels of Figure 6-7g, h, i. A full-shell fitting is provided in Figure 6-10d, e, f. The strong agreement between experimental and fitted spectra in both $\chi(k)$ space (Figure 6-7d, e, f) and $\chi(R)$ space (Figure 6-7g, h, i) confirms the reliability of the EXAFS fit.

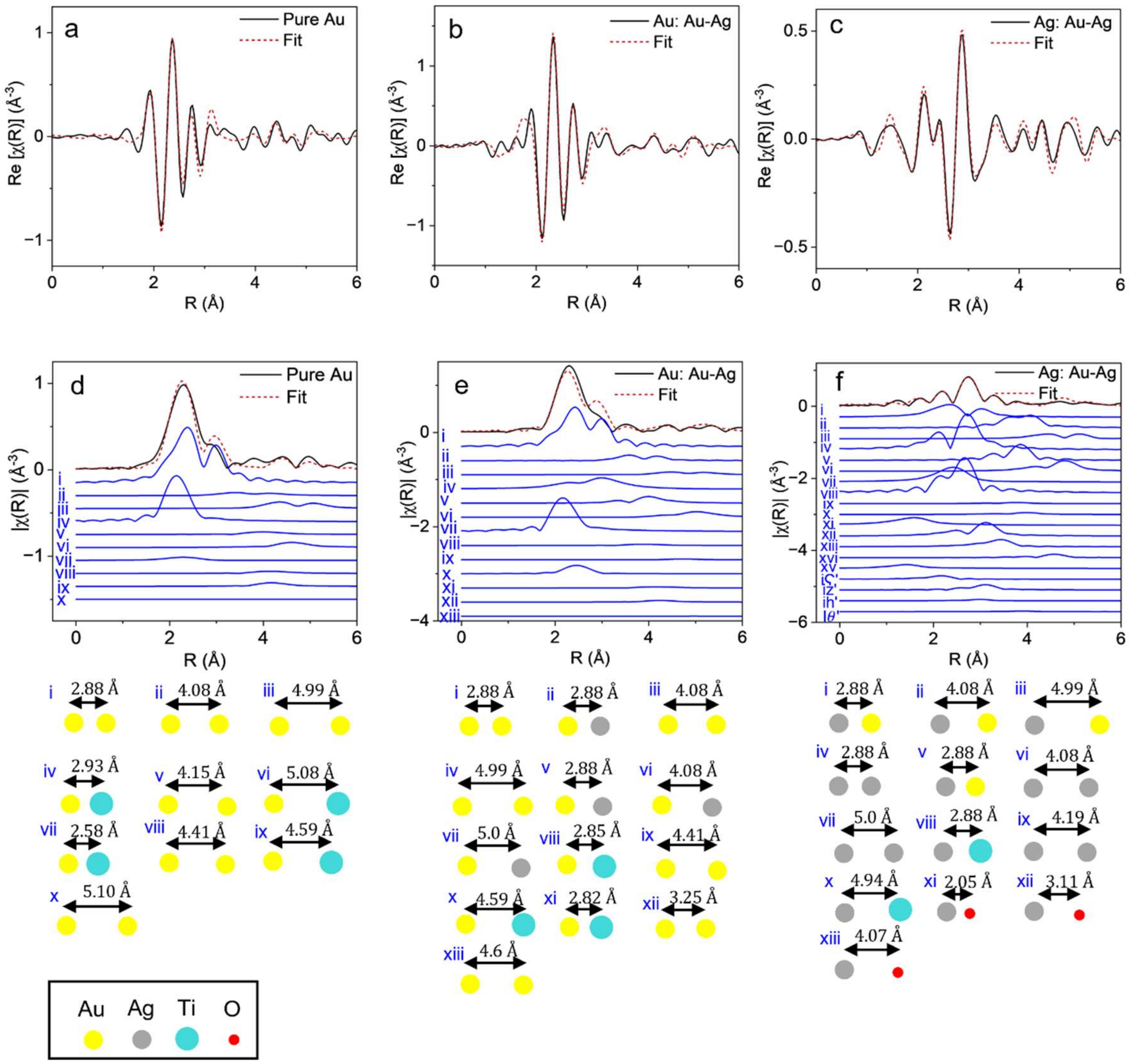

Figure 6-10. Real part of the Fourier-transformed EXAFS signals (Re[χ(R)]) for: (a) pure Au seed, (b) Au in the Au-Ag seed, and (c) Ag in the Au-Ag seed. Panels (d, e, f) show the magnitude of the R-space fitting for the first-shell single photoelectron scattering paths corresponding to the three nearest neighbors. The black solid lines represent the experimental data, the red dashed lines indicate the fit, and the blue lines highlight the contributions of the most significant photoelectron scattering paths, with their geometries displayed below each graph. These graphs provide additional support to the first-shell R-space fittings discussed in the manuscript.

The bonding distances (R), coordination numbers (CN), disorder factors (σ^2), and E_0 shifts obtained from the fitting process are summarized in Table 6-4, Table 6-5, and Table 6-6. The parameter ΔR represents the difference between the theoretical bonding distance and the fitted value, where ΔR < 0.1 Å indicates an acceptable fit [164], which holds true for nearly all first-shell scattering paths and the majority of second- and third-shell paths. The strong agreement between theoretical parameters and fitted values supports the validity of the models used in LCF fitting, confirming the presence of specific bonding interactions between the seed and growth species.

The most significant deviation in bonding distance was observed for the Au-Ti bond (Path #4) in pure Au and the corresponding Au-Ti bond (Path #7), indicating local structural distortions at the interface. This contraction of the Au-Ti bond length to approximately 2.65 Å aligns with findings from ab initio simulations, which investigated the stability and properties of Au/TiO_2(110) interfaces using density functional theory (DFT) calculations [165]. These studies demonstrated that the most stable adsorption site for an Au atom is directly atop the fivefold-coordinated Ti surface atom, resulting in a bond length of approximately 2.66 Å [166]. Experimental X-ray spectroscopy and micro-LEED (low-energy electron diffraction) measurements confirm a similar contraction in the Au-Ti bonding distance, highlighting the effect of interface reconstruction [167].

Table 6-4. Results of $k2$-weighted fitting of EXAFS in R space with all the single scattering paths for Au absorber in pure Au seed. CN was fixed to standard values. R was fitted for the first coordination shell, while for higher shells, R was fixed to the fitted value from the first shell. σ^2 and E_0 were constrained during the fitting.

				Au absorber in pure Au seed			
Model	**Path#**	**Shell**	**CN**	**R (Å)**	**Δ*R* (Å)**	**σ^2**	**E_0 shift (eV)**
M1: Au	1	Au-Au	12	2.82	-0.07	0.011	2.295
	2	Au-Au	6	3.97	-0.11	0.018	2.295
	3	Au-Au	24	4.91	-0.09	0.015	2.295
M4: AuTi3	4	Au-Ti	12	2.64	-0.30	0.006	2.295
	5	Au-Au	6	4.20	0.050	0.005	2.295
	6	Au-Ti	24	5.13	0.050	0.005	2.295

M5: AuTi3	8	Au-Ti	12	2.90	0.050	0.014	2.295
	9	Au-Au	8	4.36	-0.02	0.006	2.295
	10	Au-Ti	12	4.64	0.05	0.006	2.295

Table 6-5. Results of *k*2-weighted fitting of EXAFS in R space with all the single scattering paths for Au absorber in the Au-Ag seed. CN was fixed to standard values. R was fitted for the first coordination shell, while for higher shells, R was fixed to the fitted value from the first shell. σ^2 and E_0 were constrained during the fitting.

Au absorber in Au-Ag seed							
Model	**Path#**	**Shell**	**CN**	**R (Å)**	**Δ*R* (Å)**	$\boldsymbol{\sigma^2}$	**E_0 shift (eV)**
Au	1	Au-Au	12	2.80	-0.08	0.007	1.620
	2	Au-Au	6	3.98	-0.10	0.010	1.620
	3	Au-Au	24	4.95	-0.04	0.010	1.620
Au-Ag	4	Au-Ag	12	2.84	-0.05	0.006	1.620
	5	Au-Ag	6	3.98	-0.09	0.007	1.620
	6	Au-Ag	24	4.96	-0.02	0.010	1.620
M4: $AuTi_3$	7	Au-Ti	12	2.63	-0.30	0.005	1.620
	8	Au-Au	6	4.09	-0.06	0.006	1.620
	9	Au-Ti	24	5.18	0.09	0.009	1.620
M5: $AuTi_3$	10	Au-Ti	12	2.95	0.10	0.007	1.620
	11	Au-Au	8	4.36	-0.05	0.009	1.620
	12	Au-Au	12	4.67	0.08	0.010	1.620

Table 6-6. Results of *k*2-weighted fitting of EXAFS in R space with all the single scattering paths for Ag absorber in the Au-Ag seed. CN was fixed to standard values. R was fitted for the first coordination shell, while for higher shells, R was fixed to the fitted value from the first shell. σ^2 and E_0 were constrained during the fitting.

Ag absorber in Au-Ag seed							
Model	**Path#**	**Shell**	**CN**	**R (Å)**	**Δ*R* (Å)**	$\boldsymbol{\sigma^2}$	**E_0 shift (eV)**
Au-Ag	1	Ag-Au	12	2.86	-0.01	0.006	-1.853
	2	Ag-Au	6	4.05	-0.03	0.007	-1.853
	3	Ag-Au	24	5.07	0.09	0.010	-1.853
Ag	4	Ag-Ag	11	2.80	-0.08	0.007	-1.853
	5	Ag-Ag	6	3.98	-0.090	0.009	-1.853

	6	Ag-Ag	24	4.94	-0.05	0.010	-1.853
	7	Ag-Ti	8	2.98	0.09	0.006	-1.853
M7: AgTi	8	Ag-Ag	4	2.87	-0.03	0.006	-1.853
	9	Ag-Ag	2	3.98	-0.09	0.010	-1.853
	10	Ag-Ag	4	4.20	0.09	0.010	-1.853
	11	Ag-O	4	2.19	0.09	0.006	-1.853
M9: AgO	12	Ag-Ag	12	3.38	-0.02	0.008	-1.853
	13	Ag-O	12	4.093	0.09	0.010	-1.853
	14	Ag-Ag	6	4.92	0.10	0.010	-1.853
M11: Ag_3O_4	15	Ag-O	1	1.94	-0.15	0.005	-1.853
	16	Ag-O	1	2.72	-0.02	0.006	-1.853
	17	Ag-Ag	1	3.38	0.10	0.007	-1.853
	18	Ag-O	1	3.60	-0.09	0.007	-1.853
	19	Ag-O	1	4.56	-0.02	0.009	-1.853

6.3. Summary

Our findings reveal that the location of Ag-rich domains within Au–Ag bimetallic seeds at the growth front play a decisive role in directing sidewall faceting and growth direction of TiO_2 nanowires. When Ag-rich domains are positioned at the junction of $\{10\bar{1}\}_{TiO_2}$ and $\{1\bar{1}0\}_{TiO_2}$ facets of the growth front, they promote site-specific nucleation and enable the transition from bead-like <110> growth to prismatic <111> growth. Spectroscopic analyses suggest the presence of Ag–O bonding, indicating Ag's stronger affinity for oxygen-containing growth species. We believe that this site-specific nucleation, introduced by Ag-rich domains, at the growth front stabilizes the hexagonal growth front and guides directional growth. Our findings offer a new strategy for controlling nanowires' morphology through compositional tuning at the nanoscale.

Chapter 7

Conclusion and Future Work

This chapter concludes the thesis by summarizing the main findings and contributions of this research on the synthesis of TiO_2 nanowires, with emphasis on the controlled and optimized growth conditions achieved through tuning oxygen partial pressure and seed composition. The experimental techniques and approaches used to implement the method were described in Chapter 3, while the results were presented in Chapters 4 to 6. Finally, this chapter outlines potential directions for future work.

7.1. Conclusion

This thesis provided detailed growth conditions for applying the vapor–adsorbate–solid (VAdS) method to the synthesis of TiO_2 nanowires with tailored morphologies.

Compared with the reported open-flow PLD systems, the closed geometry used here enabled reproducible growth across a wide sealing pressure range, from 40 kPa down to 0.4 Pa, and with various seed systems.

Systematic studies of seed composition revealed how seed chemistry and interfacial energetics control nanowire growth. Nanowires grown from Au–Ni thin-film seeds exhibited less uniformity and zigzag morphologies, while nanoparticle-deposited Au seeds produced more vertically aligned, bead-like nanowires in $< 110 >_{TiO_2}$, and Au–Ag seeds yielded slightly kinked nanowires transitioning toward prismatic forms in $< 111 >_{TiO_2}$.

At the atomic scale, introducing Ni into Au seeds created a new orientation relationship at the Au–TiO_2 interface, leading to endotaxial embedding of Au nanoparticles inside nanowires. These embedded one-dimensional hybrid nanosystems exhibited distinct morphologies depending on nanowire orientation: irregularly shaped nanoparticles in bead-like [110] nanowires and faceted nanoparticles in prismatic <111> nanowires. This finding highlights the role of seed composition in tuning interface stability and growth dynamics.

Finally, the role of Ag-rich domains in Au–Ag bimetallic seeds was identified as a decisive factor in controlling nanowire morphology. When Ag segregated to the junction of $\{10\bar{1}\}_{TiO_2}$ and $\{1\bar{1}0\}_{TiO_2}$ facets, it promoted site-specific nucleation, stabilizing the hexagonal growth front and enabling transitions from bead-like $< 110 >_{Ti\ {}_2}$ to prismatic $< 111 >_{TiO_2}$ nanowires. Spectroscopic analyses confirmed Ag–O interactions, underscoring Ag's stronger affinity for oxygen and its role in directing growth.

Overall, this work demonstrates that TiO_2 nanowire morphology, growth direction, and interface structure can be tuned by manipulating growth conditions and seed composition. The results provide detailed VAdS growth conditions and new insights into how nanoscale interface chemistry and crystallography—through Ag- and Ni-induced modifications—can be harnessed to engineer one-dimensional nanostructures, including kinked nanowires with different growth directions and hybrid systems with embedded nanoparticles. These findings establish a framework for tailoring oxide nanowires for future applications in electronics, optics, and catalysis.

7.2. Contributions

- **Established a detailed protocol for the vapor-adsorbate-solid growth method**, with optimized sealing pressures, enabling reproducible growth of TiO_2 nanowires with varying seed compositions.
- **Revealed the role of seed chemistry at the nanowire–seed interface**, showing how the incorporation of Ag or Ni modifies interface energetics and, in turn, tunes nanowire morphology and growth direction.
- **Demonstrated the role of crystallographic orientation relationships in nanoparticle embedding**, extending the understanding of endotaxial growth beyond growth oscillations and seed composition.

7.3. Future Works

- **Develop surfactant-free nanoparticle synthesis**: Explore methods to eliminate stabilizing agents (e.g., PBS) from Au and Au–Ag nanoparticle solutions in order to achieve longer, more uniform TiO_2 nanowires—ideally reaching tens of microns in length.
- **Optimize Au–Ni seed formulation**: Systematically incorporate controlled amounts of Ni nanoparticles into Au-based seeds to establish a reproducible strategy for growing well-defined nanowires using Au–Ni bimetallic systems, and to investigate how Ni content influences nanopeapod formation.
- **Explore alternative seed compositions**: Investigate other bimetallic or alloy seed systems beyond Au–Ag and Au–Ni to broaden the range of materials applicable to VAdS-based nanowire synthesis.
- **Study the influence of additional growth parameters**: Examine how factors such as growth temperature, substrate type, and ambient Ar atmosphere with higher purity affect nanowire formation and morphology. This will help refine the process and expand the application of the VAdS method to other oxide nanowires, aiming to establish it as a versatile and widely applicable technique under diverse growth conditions.
- **Integrate nanowires into functional devices**: Implement the synthesized TiO_2 nanowires in sensor-based platforms to evaluate their performance and potential for real-world applications.

Appendix A:

A.1. Substrate Preparation and Handling

For sample preparation, single-crystal TiO_2 (rutile) substrates measuring 10 × 10 × 1 mm were obtained from MTI Corporation. These substrates featured a (110) surface termination, one-side EPI polishing, a surface roughness below 5 Å, and belonged to the tetragonal space group $P4_2/mnm$ (a = 4.5936 Å, c = 2.9582 Å). Each crystal was cut into four smaller pieces (5 × 5 × 1 mm) using a diamond scribe. The cutting procedure involved manually securing the substrate onto a slide, aligning the cutter wheel along the center of one edge, and applying uniform pressure along the surface until a clean, continuous score line was formed. The substrate was then carefully broken along the score to produce two halves. Repeating this process yielded four equally sized samples. It is important to wear gloves during handling to prevent surface contamination, particularly on the polished side, as the gold–rutile interface is highly sensitive to surface cleanliness.

A.2. Substrate Cleaning

Following cutting, the rutile substrates were cleaned via ultrasonication in acetone. Each sample was placed in a 10 mL disposable test tube filled with 99.99% pure acetone. The samples underwent ultrasonic cleaning for 30 minutes. After each cycle, the acetone and test tube were replaced, and the process was repeated 4 times. After the final cycle, the substrates were removed and allowed to dry naturally in ambient conditions. The cleaning setup in shown in Figure A-1, where the areas marked with red rectangles indicate the disposable tubes containing acetone and substrates.

Figure 7-1. Substrate cleaning setup, showing disposable glass tubes (highlighted with red rectangles) containing acetone and the samples, placed inside an ultrasonic bath filled with water and operated for 30 minutes.

A.3. Au–Ni Bimetallic Nanoparticle Formation

For the Au–Ni system, a sputtering technique was used instead of colloidal deposition. A ~12 nm-thick gold layer containing a small amount of nickel impurities was sputtered onto the cleaned rutile surface for 2 seconds. The deposition was carried out using an Ernest F. Fullam Inc. (EffaCoater) system, with high-purity gold (99.99%, purchased from Ted Pella Inc.) as the target material. Ni was unintentionally introduced during the gold deposition process, likely originated from within the deposition chamber due to prior Ni depositions. Sputtering was carried out under ultra-high purity argon gas (Grade 5.0, 99.999% Ar) at a partial pressure of 200 mTorr and a current of 75 mA. After sputtering, the sample was placed inside a cleaned quartz cubicle and transferred to a heat-treatment furnace for a preheating step at 400 °C for 1 hour. This step served to remove any residual hydrocarbon contamination and initiate thermodynamic instability in the thin film, facilitating the onset of the dewetting process.

A.4. Au Nanoparticle Deposition

For the deposition of pure Au nanoparticles (NP), the Turkevich method was employed. Commercially prepared Au nanoparticle suspensions with an average diameter of 20 nm (purchased from Millipore Sigma) and stabilized in phosphate-buffered saline (PBS) were used. To achieve a target surface density of approximately 1–100 particles/μm^3, the suspension was diluted using 0.3 mL of AuNP solution with 3 mL of deionized water. To remove possible contaminants from the stabilizing agent, centrifugal cleaning was performed:

1. The diluted AuNP solution was centrifuged at a speed of 9000–10,000 until the particles formed a pellet.
2. The supernatant containing salts and impurities was carefully decanted.
3. The pellet was resuspended in ~3 mL of deionized water.

4. This centrifugation and washing cycles were repeated four times to ensure purity.
5. After the final wash, the cleaned AuNPs were redispersed in deionized water for storage and use.

To deposit the nanoparticles, 0.2 mL of the cleaned AuNP solution was dropped onto a rutile substrate pre-heated to 150 °C on a hotplate. The substrate was maintained at this temperature for 5–10 minutes to ensure complete solvent evaporation. To eliminate hydrocarbon contamination, plasma cleaning was performed using Targeo EM Plasma Cleaner under the following conditions: 75 W power, pulse ratio of 255, Ar flow at 10 sccm, N_2 flow at 5 sccm, and a total treatment time of 7 minutes.

A.5. Au–Ag Bimetallic Nanoparticle Preparation

The same Turkevich-based approach was used to prepare Au–Ag bimetallic seeds using a volume ratio of 60:40 (Au:Ag). To prepare the individual solutions, 0.6 mL of Au nanoparticles was mixed with 3 mL of deionized water, and 0.4 mL of Ag nanoparticles was combined with 2 mL of deionized water. Each nanoparticle suspension was then independently subjected to four rounds of centrifugation and washing, as described earlier, to remove stabilizing agents and impurities. After purification, the two solutions were gently mixed to ensure homogeneity. The resulting bimetallic nanoparticle mixture was then deposited onto the rutile substrate and subsequently plasma cleaned under the same conditions used for the pure Au samples.

A6. Tube Sealing and Heat-Treatment

The sealing process involved the following steps:

1. The tube was first evacuated using the mechanical pump to reach ~2×10^{-3} Torr.
2. After allowing the pressure to stabilize for 15 minutes, Ar gas (with 99.997% purity) was introduced.
3. The evacuation and Ar purging cycle was repeated four times to effectively dilute and remove residual oxygen.

Despite the Ar refilling process, a small amount of oxygen remained due to the 0.003% impurity level in the Ar gas. Once the final Ar backfill was completed, the tube was sealed by flame-melting the neck while under controlled Ar pressure. The Ar pressure was varied in different trials—gradually reduced from near-atmospheric pressure (~93 kPa) to ~0.4 Pa—in order to identify the optimal gas environment for subsequent nanowire formation. The estimated oxygen partial pressure at each Ar pressure was calculated and is reported in the next chapter.

The sealed tube containing the sample was then placed in a furnace at 1000 °C for 1 hour. After the thermal treatment, the glass tube was broken open inside a secure container using a crucible tong. Care was taken not to touch the sample surface during retrieval, as this could damage the nanowires formed during the cooling and retraction phase.

Appendix B:

B.1. Fundamentals of X-ray Absorption Spectroscopy (XAS)

When materials are exposed to high-energy X-rays, electrons in their inner atomic shells may absorb the energy and transition to higher, unoccupied states. This absorption process varies with the energy of the X-rays and is described by the absorption coefficient, which is typically plotted as a function of energy to generate the X-ray absorption spectrum. Generally, this coefficient decreases smoothly with increasing energy, except at specific energies corresponding to the binding energies of core electrons—these sharp rises are known as absorption edges.

The detailed structure near and beyond these edges, collectively called X-ray Absorption Fine Structure (XAFS), is highly sensitive to the local chemical environment and the electronic structure of the absorbing atoms. XAFS is commonly divided into three regions: the edge itself, the near-edge region (XANES), and the extended fine structure (EXAFS). XANES, covering roughly 50–100 eV above the edge, provides insight into oxidation states and electronic configurations. EXAFS, which spans several hundred eV beyond the edge, contains oscillations resulting from the interference between the outgoing photoelectron wave and those backscattered by neighboring atoms. These oscillations can be analyzed to extract structural details such as coordination number, interatomic distances, and local disorder, particularly for atoms within about 5–10 Å of the absorber.

Together, XANES and EXAFS enable a detailed understanding of the local atomic structure, which is crucial in analyzing interfaces such as the one between gold and rutile in our system. To ensure high-quality data, XAS measurements are typically conducted using a synchrotron source, which provides a highly intense and tunable X-ray beam with excellent energy resolution.

B.2. Data Collection

XAS measurements at the Au-L_3 edge (11,919 eV) and Ag-K edge (25,514 eV) were carried out at the HXMA beamline of the Canadian Light Source (CLS). Among the possible absorption edges (e.g., Ti-K, Au-L_2), Au-L_3 was selected because it falls within the beamline's operational range (5–40 keV) and provides stronger signal intensity than the L_2 edge. This is due to the higher degeneracy of the $2p_{3/2}$ state (L_3) compared to the $2p_{1/2}$ (L_2), which is beneficial given the low concentration of gold at the interface. Additionally, the heavier TiO_2 matrix has a greater influence on spectral resolution than gold, reinforcing the choice of Au-L_3 as the target edge.

For silver, although L-edges ($L_3 \approx$ 3,351 eV) exist, they fall in the soft X-ray region and are not accessible or ideal for the HXMA beamline. Therefore, the Ag-K edge was chosen for its compatibility with the beamline's energy range and its ability to provide higher-energy, bulk-sensitive information, which is critical for analyzing Ag in the presence of thick oxide matrices.

Two standard modes are available in XAS experiments: transmission and fluorescence. In transmission mode, X-ray intensity before and after the sample is measured, and the absorption coefficient $\mu(E)$ is calculated based on the logarithmic ratio as follows:

$$\frac{I_1}{I_0} = e^{-\mu(E)x} \tag{3.1}$$

$$\mu(E)x = \ln\left(\frac{I_1}{I_0}\right) \tag{3.2}$$

where I_0 and I_1 are ionization chamber signal, respectively, $\mu(E)$ is absorption coefficient, x is the thickness of sample. In fluorescence mode, the emitted X-rays resulting from electron transitions back into core holes are detected by I_f detector. This mode is particularly effective for thick or dilute samples where transmission signals are weak. The relationship between the absorption coefficient and the signals is as follows:

$$\mu(E) \propto \frac{I_f}{I_0} \tag{3.3}$$

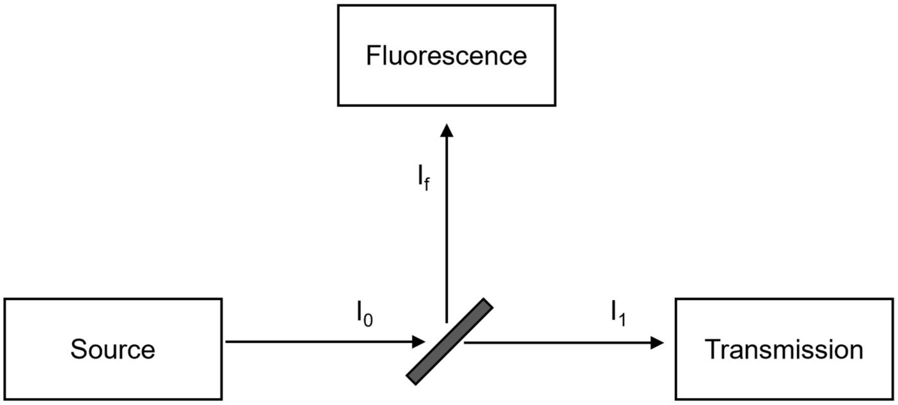

Figure B-1. General schematic setup of XAFS measurement illustrating both transmission and fluorescence detection modes.

In this study, fluorescence mode was chosen to measure the Au L_3-edge and Ag K-edge, as it was more suitable for the 1 mm-thick rutile substrates and the low concentration of species at the interface.

B.3. Data Analysis

The data reduction process for EXAFS involves analyzing the oscillations of the absorption coefficient above the edge and correlating them with the chemical environment surrounding the central absorber [168]. So, it is important to remove any background functions including intrinsic (due to absorption by the element of interest) and extrinsic background (arising from the response of detectors and elements other than the element of interest). This is achieved by transforming the absorption coefficient into a function χ(E), defined as [169]:

$$\chi(E) = \frac{\mu(E)_{exp} - \mu(E)_{bkg}}{\Delta\mu(E_0)_{exp}} \tag{1}$$

where $\mu(E)_{exp}$ is the experimentally measured absorption coefficient, $\mu(E)_{bkg}$ is the value on the background curve, and $\Delta\mu(E_0)_{exp}$ is the edge step, i.e., the difference between the pre-edge and post-edge background at the edge energy (E_0). Photo-electron energy is converted to wave number k using the following equation to further pronounce the oscillations of the spectrum [169].

$$k = \sqrt{\frac{2m(E - E_0)}{h^2}} \tag{2}$$

where E is energy of X-ray photons, E_0 is the edge energy, and h is the Planck constant. Therefore, the initial $\mu(E)_{exp}$ curve is converted to $\chi(k)$. Finally, by applying Fourier Transform (FT), $\chi(k)$ can be transformed to R space that consists of multiple shells contributed by different scattering paths.

From physical consideration, $\chi(k)$ is the probability of absorption and is related to the constructive/destructive interference of backscattering waves and the outgoing waves with sinusoidal pattern. This relationship can be defined by the following equation, known as the EXAFS equation [170]:

$$\chi(k) = S_0^2 \sum_i N_i \frac{f_i(k)}{kR_i^2} e^{-\frac{2R_i}{\lambda(k)}} e^{-2k^2\sigma_i^2} \sin(2kR_i + \Psi_i(k)) \tag{3}$$

In this equation, $f_i(k)$ and $\Psi_i(k)$ are the scattering amplitude and phase shift, respectively, reflecting the characteristics of the scattering atoms. The subscript i denotes the specific scattering path. The interatomic distance (R_i) refers to the average distance between the absorbing atom and the neighboring atom along scattering path i. The coordination number (N_i) indicates how many atoms are located at that particular distance. The disorder factor (σ_i^2) accounts for the thermal and static disorder in the interatomic distances, representing the mean square deviation from the average bond length. Additionally, the amplitude reduction factor (S_0^2) corrects for many-body effects that reduce the overall signal amplitude, and the energy shift (E_o) compensates for the difference between the experimentally determined edge energy and the theoretical value used in the calculations. Other terms serve to refine $\chi(k)$ for greater precision, such as $\lambda(k)$ which denotes the mean free path of photoelectrons, restricting EXAFS to a local region.

Since χ(k) contains oscillations in k-space, a Fourier Transform (FT) is applied to convert this function into R-space. This transformation reveals a radial distribution of scattering atoms around the absorber, allowing peaks to be associated with different coordination shells based on their distance. As a result, each shell can be defined by a specific R-range corresponding to a peak in the FT spectrum.

To extract structural parameters such as R_i, N_i, and σ_i^2 from $\chi(k)$, one typically fits theoretical models to the experimental data. These models are built using structural information from the XANES LCF, which helps identify the likely phases present. Based on this, a simple atomic cluster is created around the absorbing atom and used as input for FEFF, a program that calculates theoretical scattering paths. The cluster includes the absorber and nearby atoms within a few angstroms, capturing the local geometry. FEFF then computes $f_i(k)$ and $\delta_i(k)$ for each path, which are used in the fitting process to match the experimental EXAFS data. These paths are refined by adjusting parameters like R_i, N_i, σ_i^2, S_0^2, and E_0. Although many variables exist, the number of independent parameters that can be reliably extracted is limited by the data range[170]:

$$N_{ind} = \frac{2\Delta k \Delta R}{\pi} \tag{4}$$

where Δk and ΔR represent the range of k and R of the data. Therefore, it is necessary to limit the total number of free parameters (variables) from all paths to a value less than the number of independent parameters. In Larch, this limitation can be achieved by fixing the value or correlating the values of different paths. Constraints can also be applied to confine the value of each variable to a certain range to avoid irrational results. Larch then runs the simulation based on all the paths and constraints, providing results that best matched the experimental data. The number of shells considered increased incrementally until all major peaks were fitted with good quality which defined by R-factor and reduced χ^2 values. If the fit is unsatisfactory, it could be due to several factors such as the chosen theoretical models, improper selection of K and R ranges, or issues in data reduction. These issues should be identified through systematic analysis.

Appendix C:

Because the diffraction patterns shown in Chapter 5 are small, clearer patterns with indexing are provided here. In some zone axes, overlapping diffraction patterns of Au and TiO_2 can be observed. The TiO_2 side facets are highlighted in blue (indexing and circles), the top facets are marked in yellow, and the Au reflections are also indicated in yellow.

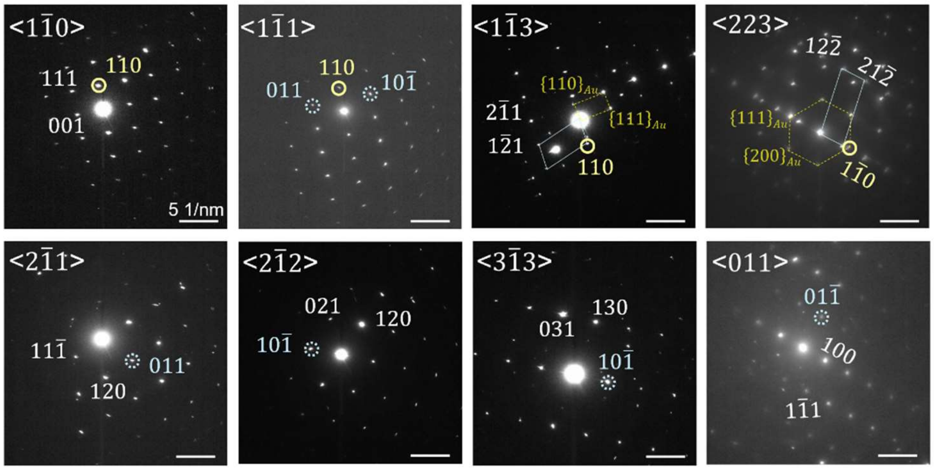

Figure C-1. Commonly observed diffraction patterns of nanowires (reported in Chapter 5) from different zone axes, enhancing the visibility of reflections. Yellow circles indicate the reflections for top facets, while the blue circles show the reflections for {101} side facets. In selected zone axes, blue lines represent the diffraction pattern for TiO_2, and the yellow dashed lines correspond to the diffraction patterns for Au. To ensure clarity and conciseness, repeated and equivalent zone axes have been excluded.

References

[1] M. A. Carpenter, S. Mathur, and A. Kolmakov, *Metal Oxide Nanomaterials for Chemical Sensors*. Springer Science & Business Media, 2012.

[2] J. Mei, T. Liao, L. Kou, and Z. Sun, "Two-Dimensional Metal Oxide Nanomaterials for Next-Generation Rechargeable Batteries," *Adv. Mater.*, vol. 29, no. 48, p. 1700176, 2017, doi: 10.1002/adma.201700176.

[3] K.-S. Lin and S. Chowdhury, "Synthesis, Characterization, and Application of 1-D Cerium Oxide Nanomaterials: A Review," *Int. J. Mol. Sci.*, vol. 11, no. 9, Art. no. 9, Sep. 2010, doi: 10.3390/ijms11093226.

[4] J. A. Rodriguez and M. Fernández-García, *Synthesis, Properties, and Applications of Oxide Nanomaterials*. John Wiley & Sons, 2007.

[5] T. Zhai *et al.*, "A Comprehensive Review of One-Dimensional Metal-Oxide Nanostructure Photodetectors," *Sensors*, vol. 9, no. 8, pp. 6504–6529, Aug. 2009, doi: 10.3390/s90806504.

[6] G. Shen, P.-C. Chen, K. Ryu, and C. Zhou, "Devices and chemical sensing applications of metal oxide nanowires," *J Mater Chem*, vol. 19, no. 7, pp. 828–839, 2009, doi: 10.1039/B816543B.

[7] Z. Zhou, C. Lan, R. Wei, and J. C. Ho, "Transparent metal-oxide nanowires and their applications in harsh electronics," *J. Mater. Chem. C*, vol. 7, no. 2, pp. 202–217, Jan. 2019, doi: 10.1039/C8TC04501A.

[8] R. S. Wagner and W. C. Ellis, "Vapor-liquid-solid mechanism of single crystal growth," *Appl. Phys. Lett.*, vol. 4, no. 5, pp. 89–90, Mar. 1964, doi: 10.1063/1.1753975.

[9] S. Kodambaka, J. B. Hannon, R. M. Tromp, and F. M. Ross, "Control of Si Nanowire Growth by Oxygen," *Nano Lett.*, vol. 6, no. 6, pp. 1292–1296, Jun. 2006, doi: 10.1021/nl060059p.

[10] F. Dehghan Nayeri and E. Asl Soleimani, "Influence of Seed Layers on the Vertical Growth of ZnO Nanowires by Low-Temperature Wet Chemical Bath Deposition on ITO-Coated Glass Substrate," *Exp. Tech.*, vol. 38, no. 4, pp. 13–20, Jul. 2014, doi: 10.1111/j.1747-1567.2012.00817.x.

[11] X. Feng, K. Shankar, O. K. Varghese, M. Paulose, T. J. Latempa, and C. A. Grimes, "Vertically Aligned Single Crystal TiO2 Nanowire Arrays Grown Directly on Transparent Conducting Oxide Coated Glass: Synthesis Details and Applications," *Nano Lett.*, vol. 8, no. 11, pp. 3781–3786, Nov. 2008, doi: 10.1021/nl802096a.

[12] J. Shi and X. Wang, "Growth of Rutile Titanium Dioxide Nanowires by Pulsed Chemical Vapor Deposition," *Cryst. Growth Des.*, vol. 11, no. 4, pp. 949–954, Apr. 2011, doi: 10.1021/cg200140k.

[13] S. Ramezani Sani, A. Morteza Ali, and R. Jafari, "The effect of carrier gas flow on structural and optical properties of TiO2 nanowires," *Phys. E Low-Dimens. Syst. Nanostructures*, vol. 43, no. 10, pp. 1809–1812, Aug. 2011, doi: 10.1016/j.physe.2011.06.016.

[14] Z. G. Shang, Z. Q. Liu, P. J. Shang, and J. K. Shang, "Synthesis of Single-Crystal TiO2 Nanowire Using Titanium Monoxide Powder by Thermal Evaporation," *J.*

Mater. Sci. Technol., vol. 28, no. 5, pp. 385–390, May 2012, doi: 10.1016/S1005-0302(12)60072-3.

[15] D. Y. Xie, M. Lin, W. Zhou, J. Wang, and G. Zhu, “Kinetically Favorable Vapor–Adsorbate–Solid Growth of Rutile Nanowires,” *Small Methods*, vol. 3, no. 7, p. 1900111, Jul. 2019, doi: 10.1002/smtd.201900111.

[16] F. Zhuge *et al.*, “Fundamental Strategy for Creating VLS Grown TiO $_2$ Single Crystalline Nanowires,” *J. Phys. Chem. C*, vol. 116, no. 45, pp. 24367–24372, Nov. 2012, doi: 10.1021/jp308945b.

[17] S. S. Leonard *et al.*, “Generation of Reactive Oxygen Species from Silicon Nanowires,” *Environ. Health Insights*, vol. 8s1, p. EHI.S15261, Jan. 2014, doi: 10.4137/EHI.S15261.

[18] R. S. Schäufele, M. Vazquez-Pufleau, and J. J. Vilatela, “Tough sheets of nanowires produced floating in the gas phase,” *Mater. Horiz.*, vol. 7, no. 11, pp. 2978–2984, 2020, doi: 10.1039/D0MH00777C.

[19] R. G. Hobbs, N. Petkov, and J. D. Holmes, “Semiconductor Nanowire Fabrication by Bottom-Up and Top-Down Paradigms,” *Chem. Mater.*, vol. 24, no. 11, pp. 1975–1991, Jun. 2012, doi: 10.1021/cm300570n.

[20] V. G. Dubrovskii, *Nucleation Theory and Growth of Nanostructures*. in NanoScience and Technology. Berlin, Heidelberg: Springer Berlin Heidelberg, 2014. doi: 10.1007/978-3-642-39660-1.

[21] B. A. Wacaser, K. A. Dick, J. Johansson, M. T. Borgström, K. Deppert, and L. Samuelson, “Preferential Interface Nucleation: An Expansion of the VLS Growth Mechanism for Nanowires,” *Adv. Mater.*, vol. 21, no. 2, pp. 153–165, 2009, doi: 10.1002/adma.200800440.

[22] Z. Razaghi and G. Zhu, “Microscopic Characteristics of Kinking Phenomenon in Vertically Free-Standing Nanowires,” *Crystals*, vol. 13, no. 10, Art. no. 10, Oct. 2023, doi: 10.3390/cryst13101459.

[23] K. W. Schwarz, J. Tersoff, S. Kodambaka, Y.-C. Chou, and F. M. Ross, “Geometrical Frustration in Nanowire Growth,” *Phys. Rev. Lett.*, vol. 107, no. 26, p. 265502, Dec. 2011, doi: 10.1103/PhysRevLett.107.265502.

[24] Y. Li, Y. Wang, S. Ryu, A. F. Marshall, W. Cai, and P. C. McIntyre, “Spontaneous, Defect-Free Kinking via Capillary Instability during Vapor–Liquid–Solid Nanowire Growth,” *Nano Lett.*, vol. 16, no. 3, pp. 1713–1718, Mar. 2016, doi: 10.1021/acs.nanolett.5b04633.

[25] I. R. Musin and M. A. Filler, “Chemical Control of Semiconductor Nanowire Kinking and Superstructure,” *Nano Lett.*, vol. 12, no. 7, pp. 3363–3368, Jul. 2012, doi: 10.1021/nl204065p.

[26] Z. H. Wu *et al.*, “Growth, branching, and kinking of molecular-beam epitaxial 〈110〉 GaAs nanowires,” *Appl. Phys. Lett.*, vol. 83, no. 16, pp. 3368–3370, Oct. 2003, doi: 10.1063/1.1618018.

[27] Y.-L. Sun, R. Matsumura, W. Jevasuwan, and N. Fukata, “Au–Sn Catalyzed Growth of Ge $_{1-x}$ Sn $_x$ Nanowires: Growth Direction, Crystallinity, and Sn Incorporation,” *Nano Lett.*, vol. 19, no. 9, pp. 6270–6277, Sep. 2019, doi: 10.1021/acs.nanolett.9b02395.

[28] F. M. Ross, J. Tersoff, and M. C. Reuter, “Sawtooth Faceting in Silicon Nanowires,” *Phys. Rev. Lett.*, vol. 95, no. 14, p. 146104, Sep. 2005, doi: 10.1103/PhysRevLett.95.146104.

[29] C.-Y. Wen *et al.*, “Periodically Changing Morphology of the Growth Interface in Si, Ge, and GaP Nanowires,” *Phys. Rev. Lett.*, vol. 107, no. 2, p. 025503, Jul. 2011, doi: 10.1103/PhysRevLett.107.025503.

[30] P. Zhou, Y. Liu, and G. Zhu, “Sawtooth Faceting in Rutile Nanowires,” *ACS Omega*, vol. 7, no. 12, pp. 10406–10412, Mar. 2022, doi: 10.1021/acsomega.1c07119.

[31] M. Lin, Y. Liu, and G. Zhu, “Mn-Promoted Growth of Mg-Based Spinel and Pyroxene Nanostructures,” *ACS Omega*, vol. 5, no. 3, pp. 1566–1571, Jan. 2020, doi: 10.1021/acsomega.9b03519.

[32] S. Wu *et al.*, “Crystal phase evolution in kinked GaN nanowires,” *Nanotechnology*, vol. 31, no. 14, p. 145713, Apr. 2020, doi: 10.1088/1361-6528/ab6479.

[33] Z. He, H. T. Nguyen, L. D. Toan, and D. Pribat, “A detailed study of kinking in indium-catalyzed silicon nanowires,” *CrystEngComm*, vol. 17, no. 33, pp. 6286–6296, Aug. 2015, doi: 10.1039/C5CE00773A.

[34] T. Burgess *et al.*, “Twinning superlattice formation in GaAs nanowires,” *ACS Nano*, vol. 7, no. 9, pp. 8105–8114, Sep. 2013, doi: 10.1021/nn403390t.

[35] R. E. Algra *et al.*, “Twinning superlattices in indium phosphide nanowires,” *Nature*, vol. 456, no. 7220, Art. no. 7220, Nov. 2008, doi: 10.1038/nature07570.

[36] H. Geaney *et al.*, “Role of Defects and Growth Directions in the Formation of Periodically Twinned and Kinked Unseeded Germanium Nanowires,” *Cryst. Growth Des.*, vol. 11, no. 7, pp. 3266–3272, Jul. 2011, doi: 10.1021/cg200510y.

[37] I. V. Markov, *Crystal Growth For Beginners: Fundamentals Of Nucleation, Crystal Growth And Epitaxy (Third Edition)*. World Scientific, 2016.

[38] V. A. Nebol’sin and A. A. Shchetinin, “Role of Surface Energy in the Vapor–Liquid–Solid Growth of Silicon,” vol. 39, no. 9, p. 5, 2003.

[39] H. Wang, L. A. Zepeda-Ruiz, G. H. Gilmer, and M. Upmanyu, “Atomistics of vapour–liquid–solid nanowire growth,” *Nat. Commun.*, vol. 4, no. 1, p. 1956, Oct. 2013, doi: 10.1038/ncomms2956.

[40] X. Duan and C. M. Lieber, “General Synthesis of Compound Semiconductor Nanowires,” *Adv. Mater.*, vol. 12, no. 4, pp. 298–302, 2000, doi: 10.1002/(SICI)1521-4095(200002)12:4<298::AID-ADMA298>3.0.CO;2-Y.

[41] Z.-Y. Zhou, Y. Ma, Q.-F. Han, and Y.-L. Liu, “Solubility, permeation, and capturing of impurity oxygen in Au/Ag: A comparative investigation from first-principles,” *Comput. Mater. Sci.*, vol. 114, pp. 79–85, Mar. 2016, doi: 10.1016/j.commatsci.2015.11.023.

[42] S. H. Oh *et al.*, “Oscillatory Mass Transport in Vapor-Liquid-Solid Growth of Sapphire Nanowires,” *Science*, vol. 330, no. 6003, pp. 489–493, Oct. 2010, doi: 10.1126/science.1190596.

[43] S. R. Hejazi, H. R. M. Hosseini, and M. S. Ghamsari, “The role of reactants and droplet interfaces on nucleation and growth of ZnO nanorods synthesized by vapor–liquid–solid (VLS) mechanism,” *J. Alloys Compd.*, vol. 455, no. 1–2, pp. 353–357, May 2008, doi: 10.1016/j.jallcom.2007.01.100.

[44] H. Simon, T. Krekeler, G. Schaan, and W. Mader, “Metal-Seeded Growth Mechanism of ZnO Nanowires,” *Cryst. Growth Des.*, vol. 13, no. 2, pp. 572–580, Feb. 2013, doi: 10.1021/cg301640v.

[45] P.-H. Shih and S. Y. Wu, “Growth Mechanism Studies of ZnO Nanowires: Experimental Observations and Short-Circuit Diffusion Analysis,” *Nanomaterials*, vol. 7, no. 7, p. 188, Jul. 2017, doi: 10.3390/nano7070188.

[46] Z. W. Pan, Z. R. Dai, and Z. L. Wang, “Nanobelts of Semiconducting Oxides,” *Science*, vol. 291, no. 5510, pp. 1947–1949, Mar. 2001, doi: 10.1126/science.1058120.

[47] Ü. Özgür *et al.*, “A comprehensive review of ZnO materials and devices,” *J. Appl. Phys.*, vol. 98, no. 4, p. 041301, Aug. 2005, doi: 10.1063/1.1992666.

[48] Z. Zhu *et al.*, “Rational Concept for Reducing Growth Temperature in Vapor–Liquid–Solid Process of Metal Oxide Nanowires,” *Nano Lett.*, vol. 16, no. 12, pp. 7495–7502, Dec. 2016, doi: 10.1021/acs.nanolett.6b03227.

[49] C. Soci *et al.*, “ZnO Nanowire UV Photodetectors with High Internal Gain,” *Nano Lett.*, vol. 7, no. 4, pp. 1003–1009, Apr. 2007, doi: 10.1021/nl070111x.

[50] L. E. Greene *et al.*, “General Route to Vertical ZnO Nanowire Arrays Using Textured ZnO Seeds,” *Nano Lett.*, vol. 5, no. 7, pp. 1231–1236, Jul. 2005, doi: 10.1021/nl050788p.

[51] Y. Zhang *et al.*, “Low-temperature growth and Raman scattering study of vertically aligned ZnO nanowires on Si substrate,” *Appl. Phys. Lett.*, vol. 83, no. 22, pp. 4631–4633, Dec. 2003, doi: 10.1063/1.1630849.

[52] A. Kolmakov and M. Moskovits, “CHEMICAL SENSING AND CATALYSIS BY ONE-DIMENSIONAL METAL-OXIDE NANOSTRUCTURES,” *Annu. Rev. Mater. Res.*, vol. 34, no. Volume 34, 2004, pp. 151–180, Aug. 2004, doi: 10.1146/annurev.matsci.34.040203.112141.

[53] A. Klamchuen *et al.*, “Rational Concept for Designing Vapor–Liquid–Solid Growth of Single Crystalline Metal Oxide Nanowires,” *Nano Lett.*, vol. 15, no. 10, pp. 6406–6412, Oct. 2015, doi: 10.1021/acs.nanolett.5b01604.

[54] M. Suzuki *et al.*, “Essential role of catalyst in vapor-liquid-solid growth of compounds,” *Phys. Rev. E*, vol. 83, no. 6, p. 061606, Jun. 2011, doi: 10.1103/PhysRevE.83.061606.

[55] L. D. Landau and E. M. Lifshitz, *Statistical Physics: Volume 5*. Elsevier, 2013.

[56] S. A. Kukushkin and A. V. Osipov, “Thin-film condensation processes,” *Phys.-Uspekhi*, vol. 41, no. 10, p. 983, Oct. 1998, doi: 10.1070/PU1998v041n10ABEH000461.

[57] A. M. Streets and S. R. Quake, “Ostwald Ripening of Clusters during Protein Crystallization,” *Phys. Rev. Lett.*, vol. 104, no. 17, p. 178102, Apr. 2010, doi: 10.1103/PhysRevLett.104.178102.

[58] V. G. Dubrovskii and N. V. Sibirev, “Growth rate of a crystal facet of arbitrary size and growth kinetics of vertical nanowires,” *Phys. Rev. E*, vol. 70, no. 3, p. 031604, Sep. 2004, doi: 10.1103/PhysRevE.70.031604.

[59] Z. Razaghi, D. Y. Xie, M. Lin, and G. Zhu, “Ion beam-induced bending of TiO_2 nanowires with bead-like and prismatic shapes,” *RSC Adv.*, vol. 12, no. 9, pp. 5577–5586, 2022, doi: 10.1039/D1RA09122K.

[60] B. Liu and E. S. Aydil, “Growth of oriented single-crystalline rutile TiO(2) nanorods on transparent conducting substrates for dye-sensitized solar cells,” *J. Am. Chem. Soc.*, vol. 131, no. 11, pp. 3985–3990, Mar. 2009, doi: 10.1021/ja8078972.

[61] L. Huang *et al.*, “Controlled growth of well-faceted zigzag tin oxide mesostructures,” *Appl. Phys. Lett.*, vol. 87, no. 16, p. 163124, Oct. 2005, doi: 10.1063/1.2112207.

[62] C. Yan, N. Singh, and P. S. Lee, “Kinking-Induced Structural Evolution of Metal Oxide Nanowires into Single-Crystalline Nanorings,” *ACS Nano*, vol. 4, no. 9, pp. 5350–5356, Sep. 2010, doi: 10.1021/nn101386c.

[63] Z. C. Tu, Q. X. Li, and X. Hu, “Theoretical determination of the necessary conditions for the formation of ZnO nanorings and nanohelices,” *Phys. Rev. B*, vol. 73, no. 11, p. 115402, Mar. 2006, doi: 10.1103/PhysRevB.73.115402.

[64] C.-H. Hsieh, L.-J. Chou, G.-R. Lin, Y. Bando, and D. Golberg, “Nanophotonic Switch: Gold-in-Ga2O3 Peapod Nanowires,” *Nano Lett.*, vol. 8, no. 10, pp. 3081–3085, Oct. 2008, doi: 10.1021/nl0731567.

[65] W. W. Zhou, L. Sun, T. Yu, J. X. Zhang, H. Gong, and H. J. Fan, “The morphology of Au@MgO nanopeapods,” *Nanotechnology*, vol. 20, no. 45, p. 455603, Nov. 2009, doi: 10.1088/0957-4484/20/45/455603.

[66] Y. Chen *et al.*, “Effects of Defects on the Mechanical Properties of Kinked Silicon Nanowires,” *Nanoscale Res. Lett.*, vol. 12, no. 1, p. 185, Mar. 2017, doi: 10.1186/s11671-017-1970-7.

[67] J.-W. Jiang, J.-H. Zhao, and T. Rabczuk, “Size-sensitive Young’s modulus of kinked silicon nanowires,” *Nanotechnology*, vol. 24, no. 18, p. 185702, May 2013, doi: 10.1088/0957-4484/24/18/185702.

[68] B. Tian, P. Xie, T. J. Kempa, D. C. Bell, and C. M. Lieber, “Single-crystalline kinked semiconductor nanowire superstructures,” *Nat. Nanotechnol.*, vol. 4, no. 12, pp. 824–829, Dec. 2009, doi: 10.1038/nnano.2009.304.

[69] G. Shen, B. Liang, X. Wang, P.-C. Chen, and C. Zhou, “Indium oxide nanospirals made of kinked nanowires,” *ACS Nano*, vol. 5, no. 3, pp. 2155–2161, Mar. 2011, doi: 10.1021/nn103358y.

[70] B. G. Cook and K. Varga, “Conductance of kinked nanowires,” *Appl. Phys. Lett.*, vol. 98, no. 5, p. 052104, Feb. 2011, doi: 10.1063/1.3551711.

[71] Z. Jiang, Q. Qing, P. Xie, R. Gao, and C. M. Lieber, “Kinked p–n Junction Nanowire Probes for High Spatial Resolution Sensing and Intracellular Recording,” *Nano Lett.*, vol. 12, no. 3, pp. 1711–1716, Mar. 2012, doi: 10.1021/nl300256r.

[72] B. Tian, T. Cohen-Karni, Q. Qing, X. Duan, P. Xie, and C. M. Lieber, “Three-dimensional, flexible nanoscale field-effect transistors as localized bioprobes,” *Science*, vol. 329, no. 5993, pp. 830–834, Aug. 2010, doi: 10.1126/science.1192033.

[73] L. Xu, Z. Jiang, Q. Qing, L. Mai, Q. Zhang, and C. M. Lieber, “Design and Synthesis of Diverse Functional Kinked Nanowire Structures for Nanoelectronic Bioprobes,” *Nano Lett.*, vol. 13, no. 2, pp. 746–751, Feb. 2013, doi: 10.1021/nl304435z.

[74] S. Li, X. Zhang, L. Zhang, and M. Gao, “Twinning-induced kinking of Sb-doped ZnO nanowires,” *Nanotechnology*, vol. 21, no. 43, p. 435602, Oct. 2010, doi: 10.1088/0957-4484/21/43/435602.

[75] J. Wang, X. W. Sun, S. Xie, W. Zhou, and Y. Yang, “Single-Crystal and Twinned Zn2SnO4 Nanowires with Axial Periodical Structures,” *Cryst. Growth Des.*, vol. 8, no. 2, pp. 707–710, Feb. 2008, doi: 10.1021/cg060779+.

[76] Y. Shen *et al.*, “Size-Induced Switching of Nanowire Growth Direction: a New Approach Toward Kinked Nanostructures,” *Adv. Funct. Mater.*, vol. 26, no. 21, pp. 3687–3695, 2016, doi: 10.1002/adfm.201600142.

[77] Y. H. Gao, Y. Bando, T. Sato, Y. F. Zhang, and X. Q. Gao, “Synthesis, Raman scattering and defects of β-Ga2O3 nanorods,” *Appl. Phys. Lett.*, vol. 81, no. 12, pp. 2267–2269, Sep. 2002, doi: 10.1063/1.1507835.

[78] J. X. Wang *et al.*, “Growth of SnO 2 nanowires with uniform branched structures,” *Solid State Commun.*, vol. 130, no. 1–2, pp. 89–94, Apr. 2004, doi: 10.1016/j.ssc.2004.01.003.

[79] L. Gan, M. Liao, H. Li, Y. Ma, and T. Zhai, “Geometry-induced high performance ultraviolet photodetectors in kinked SnO2 nanowires,” *J. Mater. Chem. C*, vol. 3, no. 32, pp. 8300–8306, Aug. 2015, doi: 10.1039/C5TC01178G.

[80] S. A. Maier, P. G. Kik, and H. A. Atwater, “Optical pulse propagation in metal nanoparticle chain waveguides,” *Phys. Rev. B*, vol. 67, no. 20, p. 205402, May 2003, doi: 10.1103/PhysRevB.67.205402.

[81] M. Quinten, A. Leitner, J. R. Krenn, and F. R. Aussenegg, “Electromagnetic energy transport via linear chains of silver nanoparticles,” *Opt. Lett.*, vol. 23, no. 17, pp. 1331–1333, Sep. 1998, doi: 10.1364/OL.23.001331.

[82] M.-S. Hu *et al.*, “Photosensitive gold-nanoparticle-embedded dielectric nanowires,” *Nat. Mater.*, vol. 5, no. 2, pp. 102–106, Feb. 2006, doi: 10.1038/nmat1564.

[83] H. Jiang, Y. Hu, S. Guo, C. Yan, P. S. Lee, and C. Li, “Rational Design of MnO/Carbon Nanopeapods with Internal Void Space for High-Rate and Long-Life Li-Ion Batteries,” *ACS Nano*, vol. 8, no. 6, pp. 6038–6046, Jun. 2014, doi: 10.1021/nn501310n.

[84] Y. Qin, L. Liu, R. Yang, U. Gösele, and M. Knez, “General Assembly Method for Linear Metal Nanoparticle Chains Embedded in Nanotubes,” *Nano Lett.*, vol. 8, no. 10, pp. 3221–3225, Oct. 2008, doi: 10.1021/nl801548h.

[85] Z. Sun, A. Tzaguy, O. Hazut, L. J. Lauhon, R. Yerushalmi, and D. N. Seidman, “1-D Metal Nanobead Arrays within Encapsulated Nanowires via a Red-Ox-Induced Dewetting: Mechanism Study by Atom-Probe Tomography,” *Nano Lett.*, vol. 17, no. 12, pp. 7478–7486, Dec. 2017, doi: 10.1021/acs.nanolett.7b03391.

[86] F. Wu, Y. Myung, and P. Banerjee, “Rayleigh Instability Driven Nodular Cu2O Nanowires via Carbothermal Reduction of CuO Nanowires,” *Cryst. Growth Des.*, vol. 15, no. 4, pp. 1588–1595, Apr. 2015, doi: 10.1021/cg500784y.

[87] J. A. Sioss and C. D. Keating, “Batch Preparation of Linear Au and Ag Nanoparticle Chains via Wet Chemistry,” *Nano Lett.*, vol. 5, no. 9, pp. 1779–1783, Sep. 2005, doi: 10.1021/nl051370u.

[88] F. M. Kolb, A. Berger, H. Hofmeister, E. Pippel, U. Gösele, and M. Zacharias, “Periodic chains of gold nanoparticles and the role of oxygen during the growth of silicon nanowires,” *Appl. Phys. Lett.*, vol. 89, no. 17, p. 173111, Oct. 2006, doi: 10.1063/1.2364835.

[89] J. s. Wu, S. Dhara, C. t. Wu, K. h. Chen, Y. f. Chen, and L. c. Chen, “Growth and Optical Properties of Self-Organized Au2Si Nanospheres Pea-Podded in a Silicon Oxide Nanowire,” *Adv. Mater.*, vol. 14, no. 24, pp. 1847–1850, 2002, doi: 10.1002/adma.200290017.

[90] N.-K. Lee and J.-H. Yoon, “Self-assembly and growth mechanism of au nanoparticle chains in silica nanowires,” *J. Korean Phys. Soc.*, vol. 66, no. 5, pp. 828–831, Mar. 2015, doi: 10.3938/jkps.66.828.

[91] Y. F. Lai, P. Chaudouët, F. Charlot, I. Matko, and C. Dubourdieu, “Magnesium oxide nanowires synthesized by pulsed liquid-injection metal organic chemical vapor deposition,” *Appl. Phys. Lett.*, vol. 94, no. 2, p. 022904, Jan. 2009, doi: 10.1063/1.3064134.

[92] L. Liu, W. Lee, R. Scholz, E. Pippel, and U. Gösele, “Tailor-Made Inorganic Nanopeapods: Structural Design of Linear Noble Metal Nanoparticle Chains,” *Angew. Chem. Int. Ed.*, vol. 47, no. 37, pp. 7004–7008, 2008, doi: 10.1002/anie.200801931.

[93] F. M. Kolb *et al.*, “Analysis of Silicon Nanowires Grown by Combining SiO Evaporation with the VLS Mechanism,” *J. Electrochem. Soc.*, vol. 151, no. 7, p. G472, May 2004, doi: 10.1149/1.1759365.

[94] F. Zhuge *et al.*, “Fundamental Strategy for Creating VLS Grown TiO2 Single Crystalline Nanowires,” *J. Phys. Chem. C*, vol. 116, no. 45, pp. 24367–24372, Nov. 2012, doi: 10.1021/jp308945b.

[95] D. Nason and W. A. Tiller, “Solid/liquid interfacial free energies in binary systems,” *Surf. Sci.*, vol. 40, no. 1, pp. 109–124, Oct. 1973, doi: 10.1016/0039-6028(73)90055-1.

[96] E. I. Givargizov, “Periodic instability in whisker growth,” *J. Cryst. Growth*, vol. 20, no. 3, pp. 217–226, Oct. 1973, doi: 10.1016/0022-0248(73)90008-0.

[97] H. Wang *et al.*, “A surface curvature oscillation model for vapour–liquid–solid growth of periodic one-dimensional nanostructures,” *Nat. Commun.*, vol. 6, no. 1, p. 6412, Mar. 2015, doi: 10.1038/ncomms7412.

[98] L. Dai, L. P. You, X. F. Duan, W. C. Lian, and G. G. Qin, “Synthesis of Ga2O3 chains with closely spaced knots connected by nanowires,” *J. Cryst. Growth*, vol. 267, no. 3, pp. 538–542, Jul. 2004, doi: 10.1016/j.jcrysgro.2004.04.013.

[99] F. Panciera *et al.*, “Synthesis of nanostructures in nanowires using sequential catalyst reactions,” *Nat. Mater.*, vol. 14, no. 8, pp. 820–825, Aug. 2015, doi: 10.1038/nmat4352.

[100] W. H. Baur and A. A. Khan, “Rutile-type compounds. IV. SiO2, GeO2 and a comparison with other rutile-type structures,” *Acta Crystallogr. Sect. B*, vol. 27, no. 11, pp. 2133–2139, 1971, doi: 10.1107/S0567740871005466.

[101] H. Perron, C. Domain, J. Roques, R. Drot, E. Simoni, and H. Catalette, “Optimisation of accurate rutile TiO2 (110), (100), (101) and (001) surface models from periodic DFT calculations,” *Theor. Chem. Acc.*, vol. 117, no. 4, pp. 565–574, Apr. 2007, doi: 10.1007/s00214-006-0189-y.

[102] A. Kiejna, T. Pabisiak, and S. W. Gao, “The energetics and structure of rutile TiO2(110),” *J. Phys. Condens. Matter*, vol. 18, no. 17, p. 4207, Apr. 2006, doi: 10.1088/0953-8984/18/17/009.

[103] S. H. Overbury, P. A. Bertrand, and G. A. Somorjai, “Surface composition of binary systems. Prediction of surface phase diagrams of solid solutions,” *Chem. Rev.*, vol. 75, no. 5, pp. 547–560, Oct. 1975, doi: 10.1021/cr60297a001.

[104] J. Zhang, E. Strelcov, and A. Kolmakov, “Visible Light Assisted Gas Sensing with TiO2 Nanowires,” Jan. 08, 2015, *arXiv*: arXiv:1501.01877. doi: 10.48550/arXiv.1501.01877.

[105] Z. Fu and H. Onishi, “Infrared and Near-Infrared Spectrometry of Anatase and Rutile Particles Bandgap Excited in Liquid,” *J. Phys. Chem. B*, vol. 127, no. 1, pp. 321–327, Jan. 2023, doi: 10.1021/acs.jpcb.2c07433.

[106] J.-Y. Liao, V. Chabot, M. Gu, C. Wang, X. Xiao, and Z. Chen, “Dual phase Li4Ti5O12–TiO2 nanowire arrays as integrated anodes for high-rate lithium-ion batteries,” *Nano Energy*, vol. 9, pp. 383–391, Oct. 2014, doi: 10.1016/j.nanoen.2014.06.032.

[107] T. Lan, H. Qiu, F. Xie, J. Yang, and M. Wei, “Rutile TiO2 Mesocrystals/Reduced Graphene Oxide with High-Rate and Long-Term Performance for Lithium-Ion Batteries,” *Sci. Rep.*, vol. 5, no. 1, p. 8498, Feb. 2015, doi: 10.1038/srep08498.

[108] B. Liu and E. S. Aydil, “Growth of Oriented Single-Crystalline Rutile TiO2 Nanorods on Transparent Conducting Substrates for Dye-Sensitized Solar Cells,” *J. Am. Chem. Soc.*, vol. 131, no. 11, pp. 3985–3990, Mar. 2009, doi: 10.1021/ja8078972.

[109] Z. Miao, D. Xu, J. Ouyang, G. Guo, X. Zhao, and Y. Tang, “Electrochemically Induced Sol−Gel Preparation of Single-Crystalline TiO2 Nanowires,” *Nano Lett.*, vol. 2, no. 7, pp. 717–720, Jul. 2002, doi: 10.1021/nl025541w.

[110] J. Jiu, S. Isoda, F. Wang, and M. Adachi, “Dye-Sensitized Solar Cells Based on a Single-Crystalline TiO2 Nanorod Film,” *J. Phys. Chem. B*, vol. 110, no. 5, pp. 2087–2092, Feb. 2006, doi: 10.1021/jp055824n.

[111] L. Yang, Z. Zhou, J. Song, and X. Chen, “Anisotropic nanomaterials for shape-dependent physicochemical and biomedical applications,” *Chem. Soc. Rev.*, vol. 48, no. 19, pp. 5140–5176, Sep. 2019, doi: 10.1039/C9CS00011A.

[112] H. Shen, Z. Wang, Y. Wu, and B. Yang, “One-dimensional photonic crystals: fabrication, responsiveness and emerging applications in 3D construction,” *RSC Adv.*, vol. 6, no. 6, pp. 4505–4520, 2016, doi: 10.1039/C5RA21373H.

[113] M. Law, L. E. Greene, A. Radenovic, T. Kuykendall, J. Liphardt, and P. Yang, “ZnO−Al_2 O_3 and ZnO−TiO_2 Core−Shell Nanowire Dye-Sensitized Solar Cells,” *J. Phys. Chem. B*, vol. 110, no. 45, pp. 22652–22663, Nov. 2006, doi: 10.1021/jp0648644.

[114] M. M. Orosco, C. Pacholski, and M. J. Sailor, “Real-time monitoring of enzyme activity in a mesoporous silicon double layer,” *Nat. Nanotechnol.*, vol. 4, no. 4, pp. 255–258, Apr. 2009, doi: 10.1038/nnano.2009.11.

[115] Y.-C. Chen, Y.-K. Hsu, R. Popescu, D. Gerthsen, Y.-G. Lin, and C. Feldmann, “Au@Nb@HxK1-xNbO3 nanopeapods with near-infrared active plasmonic hot-electron injection for water splitting,” *Nat. Commun.*, vol. 9, p. 232, Jan. 2018, doi: 10.1038/s41467-017-02676-w.

[116] D. Y. Xie, M. Lin, W. Zhou, J. Wang, and G. Zhu, “Kinetically Favorable Vapor–Adsorbate–Solid Growth of Rutile Nanowires,” *Small Methods*, vol. 3, no. 7, p. 1900111, Jul. 2019, doi: 10.1002/smtd.201900111.

[117] L. Karmazin, “Accurate measurement of lattice parameters of Ag-Au solid solutions,” *Czechoslov. J. Phys.*, vol. 19, no. 5, pp. 634–639, May 1969, doi: 10.1007/BF01691477.

[118] T. Ressler, "WinXAS: a Program for X-ray Absorption Spectroscopy Data Analysis under MS-Windows," *J. Synchrotron Radiat.*, vol. 5, no. 2, pp. 118–122, Mar. 1998, doi: 10.1107/S0909049597019298.

[119] M. Newville, "Larch: An Analysis Package for XAFS and Related Spectroscopies," *J. Phys. Conf. Ser.*, vol. 430, no. 1, p. 012007, Apr. 2013, doi: 10.1088/1742-6596/430/1/012007.

[120] E.-S. Jeong, J. Park, J.-G. Park, D. S. Adipranoto, T. Kamiyama, and S.-W. Han, "Local structural properties of CuI at low temperatures," *J. Phys. Condens. Matter*, vol. 23, no. 17, p. 175402, May 2011, doi: 10.1088/0953-8984/23/17/175402.

[121] C. E. Hendricks, A. N. Mansour, D. A. Fuentevilla, G. H. Waller, J. K. Ko, and M. G. Pecht, "Copper Dissolution in Overdischarged Lithium-ion Cells: X-ray Photoelectron Spectroscopy and X-ray Absorption Fine Structure Analysis," *J. Electrochem. Soc.*, vol. 167, no. 9, p. 090501, Jan. 2020, doi: 10.1149/1945-7111/ab697a.

[122] S. I. Zabinsky, J. J. Rehr, A. Ankudinov, R. C. Albers, and M. J. Eller, "Multiple-scattering calculations of x-ray-absorption spectra," *Phys. Rev. B*, vol. 52, no. 4, pp. 2995–3009, Jul. 1995, doi: 10.1103/PhysRevB.52.2995.

[123] D. C. Koningsberger, "Stereo Chemistry and Electronic Structure XAFS Spectroscopy: Data-Analysis and Applications," in *Neutron and Synchrotron Radiation for Condensed Matter Studies*, Springer, Berlin, Heidelberg, 1994, pp. 213–244. doi: 10.1007/978-3-662-22223-2_10.

[124] J. J. Rehr and R. C. Albers, "Theoretical approaches to x-ray absorption fine structure," *Rev. Mod. Phys.*, vol. 72, no. 3, pp. 621–654, Jul. 2000, doi: 10.1103/RevModPhys.72.621.

[125] B. Ravel and M. Newville, "ATHENA, ARTEMIS, HEPHAESTUS: data analysis for X-ray absorption spectroscopy using IFEFFIT," *J. Synchrotron Radiat.*, vol. 12, no. 4, pp. 537–541, Jul. 2005, doi: 10.1107/S0909049505012719.

[126] S. Yao, M. Wen, and G. Zhu, "Bimodal size distribution of dewetted gold nanoparticles with regrown oxide bases," *Appl. Surf. Sci.*, vol. 501, p. 144227, Jan. 2020, doi: 10.1016/j.apsusc.2019.144227.

[127] M. Lin, W. Zhou, X. Gu, and G. Zhu, "Gold-rutile interfaces with irrational crystallographic orientations," *Mater. Charact.*, vol. 176, p. 111116, Jun. 2021, doi: 10.1016/j.matchar.2021.111116.

[128] T. Majdi *et al.*, "Evidence for an equilibrium epitaxial complexion at the Au-MgAl $_2$ O $_4$ interface," *Appl. Phys. Lett.*, vol. 107, no. 24, p. 241601, Dec. 2015, doi: 10.1063/1.4937430.

[129] A. Yi, F. Liu, D. Y. Xie, M. Wen, and G. Zhu, "Gold-assisted growth of oxide bases underneath dewetted gold nanoparticles," *Mater. Charact.*, vol. 151, pp. 237–241, May 2019, doi: 10.1016/j.matchar.2019.03.012.

[130] P. W. Gilles, K. D. Carlson, H. F. Franzen, and P. G. Wahlbeck, "High-Temperature Vaporization and Thermodynamics of the Titanium Oxides. I. Vaporization Characteristics of the Crystalline Phases," *J. Chem. Phys.*, vol. 46, no. 7, pp. 2461–2465, Apr. 1967, doi: 10.1063/1.1841070.

[131] C. C. Chen, "Phase Equilibria at Ti–Al Interface Under Low Oxygen Pressure," *Atlas J. Mater. Sci.*, vol. 1, no. 1, pp. 1–11, 2014, doi: 10.5147/ajms.v1i1.116.

[132] F. Liu *et al.*, “Temperature-Induced Atomic Reconstruction At Au/MgAl2O4 Interfaces,” *Adv. Mater. Interfaces*, vol. 5, no. 12, p. 1701664, 2018, doi: 10.1002/admi.201701664.

[133] G. Zhu, T. Majdi, Y. Shao, M. Bugnet, J. S. Preston, and G. A. Botton, “Atomic structure and bonding of the interfacial bilayer between Au nanoparticles and epitaxially regrown MgAl2O4 substrates,” *Appl. Phys. Lett.*, vol. 105, no. 23, p. 231607, Dec. 2014, doi: 10.1063/1.4902939.

[134] F. Liu, D. Y. Xie, T. Majdi, and G. Zhu, “Twin-assisted growth of nominally stable substrates underneath dewetted Au nanoparticles,” *Mater. Charact.*, vol. 113, pp. 67–70, Mar. 2016, doi: 10.1016/j.matchar.2016.01.005.

[135] J. Sopoušek *et al.*, “Au-Ni nanoparticles: Phase diagram prediction, synthesis, characterization, and thermal stability,” *Calphad*, vol. 58, pp. 25–33, Sep. 2017, doi: 10.1016/j.calphad.2017.05.002.

[136] F. Cosandey, “Epitaxy, interfacial energy and atomic structure of Au/TiO2 interfaces,” *Philos. Mag.*, vol. 93, no. 10–12, pp. 1197–1218, Apr. 2013, doi: 10.1080/14786435.2013.770178.

[137] C. M. Wang, Y. Zhang, V. Shutthanandan, S. Thevuthasan, and G. Duscher, “Microstructure of precipitated Au nanoclusters in TiO2,” *J. Appl. Phys.*, vol. 95, no. 12, pp. 8185–8193, Jun. 2004, doi: 10.1063/1.1748859.

[138] S. A. Tenney *et al.*, “CO-Induced Diffusion of Ni Atoms to the Surface of Ni–Au Clusters on TiO2(110),” *J. Phys. Chem. C*, vol. 115, no. 22, pp. 11112–11123, Jun. 2011, doi: 10.1021/jp2014258.

[139] R. P. Galhenage *et al.*, “Understanding the Nucleation and Growth of Metals on TiO2: Co Compared to Au, Ni, and Pt,” *J. Phys. Chem. C*, vol. 117, no. 14, pp. 7191–7201, Apr. 2013, doi: 10.1021/jp401283k.

[140] S. Halpegamage, Z.-H. Wen, X.-Q. Gong, and M. Batzill, “Monolayer Intermixed Oxide Surfaces: Fe, Ni, Cr, and V Oxides on Rutile TiO2(011),” *J. Phys. Chem. C*, vol. 120, no. 27, pp. 14782–14794, Jul. 2016, doi: 10.1021/acs.jpcc.6b05186.

[141] T. Wang *et al.*, “Nature of metal-support interaction for metal catalysts on oxide supports,” *Science*, vol. 386, no. 6724, pp. 915–920, Nov. 2024, doi: 10.1126/science.adp6034.

[142] A. Mashreghi, “Determining the volume thermal expansion coefficient of TiO2 nanoparticle by molecular dynamics simulation,” *Comput. Mater. Sci.*, vol. 62, pp. 60–64, Sep. 2012, doi: 10.1016/j.commatsci.2012.05.018.

[143] M. S. Omar, “Models for mean bonding length, melting point and lattice thermal expansion of nanoparticle materials,” *Mater. Res. Bull.*, vol. 47, no. 11, pp. 3518–3522, Nov. 2012, doi: 10.1016/j.materresbull.2012.06.067.

[144] R. G. Haverkamp, P. Kappen, K. H. Sizeland, and K. S. Wallwork, “Niobium K-Edge X-ray Absorption Spectroscopy of Doped TiO2 Produced from Ilmenite Digested in Hydrochloric Acid,” *ACS Omega*, vol. 7, no. 32, pp. 28258–28264, Aug. 2022, doi: 10.1021/acsomega.2c02676.

[145] L. X. Chen, T. Rajh, Z. Wang, and M. C. Thurnauer, “XAFS Studies of Surface Structures of TiO2 Nanoparticles and Photocatalytic Reduction of Metal Ions,” *J. Phys. Chem. B*, vol. 101, no. 50, pp. 10688–10697, Dec. 1997, doi: 10.1021/jp971930g.

[146] N. Wada *et al.*, “Effect of adding Au nanoparticles to TiO2 films on crystallization, phase transformation, and photocatalysis,” *J. Mater. Res.*, vol. 33, no. 4, pp. 467–481, Feb. 2018, doi: 10.1557/jmr.2018.16.

[147] S. Liu *et al.*, “Ultrastable Au nanoparticles on titania through an encapsulation strategy under oxidative atmosphere,” *Nat. Commun.*, vol. 10, no. 1, p. 5790, Dec. 2019, doi: 10.1038/s41467-019-13755-5.

[148] H. Wang *et al.*, “Oxygen-Saturated Strong Metal-Support Interactions Triggered by Water on Titania Supported Catalysts,” *Adv. Funct. Mater.*, vol. 33, no. 42, p. 2304303, 2023, doi: 10.1002/adfm.202304303.

[149] S. Nishimura, A. T. N. Dao, D. Mott, K. Ebitani, and S. Maenosono, “X-ray Absorption Near-Edge Structure and X-ray Photoelectron Spectroscopy Studies of Interfacial Charge Transfer in Gold–Silver–Gold Double-Shell Nanoparticles,” *J. Phys. Chem. C*, vol. 116, no. 7, pp. 4511–4516, Feb. 2012, doi: 10.1021/jp212031h.

[150] I. J. Godfrey, A. J. Dent, I. P. Parkin, S. Maenosono, and G. Sankar, “Structure of Gold−Silver Nanoparticles,” *J Phys Chem C*, 2017.

[151] D. Morris, X. Du, R. Jin, and P. Zhang, “Single-atom alloy structure and unique bonding properties of Au_{104} Ag_{40} $(PET)_{60}$ nanoclusters,” *Nanoscale*, vol. 16, no. 34, pp. 16140–16147, 2024, doi: 10.1039/D4NR02688H.

[152] S. Hannemann, J.-D. Grunwaldt, F. Krumeich, P. Kappen, and A. Baiker, “Electron microscopy and EXAFS studies on oxide-supported gold–silver nanoparticles prepared by flame spray pyrolysis,” *Appl. Surf. Sci.*, vol. 252, no. 22, pp. 7862–7873, Sep. 2006, doi: 10.1016/j.apsusc.2005.09.065.

[153] J. D. Padmos *et al.*, “The surface structure of silver-coated gold nanocrystals and its influence on shape control,” *Nat. Commun.*, vol. 6, no. 1, p. 7664, Jul. 2015, doi: 10.1038/ncomms8664.

[154] O. R. Schade *et al.*, “Selective Aerobic Oxidation of 5-(Hydroxymethyl)furfural over Heterogeneous Silver-Gold Nanoparticle Catalysts,” *Adv. Synth. Catal.*, vol. 362, no. 24, pp. 5681–5696, 2020, doi: 10.1002/adsc.202001003.

[155] T. Shibata, B. A. Bunker, Z. Zhang, D. Meisel, C. F. Vardeman, and J. D. Gezelter, “Size-Dependent Spontaneous Alloying of Au−Ag Nanoparticles,” *J. Am. Chem. Soc.*, vol. 124, no. 40, pp. 11989–11996, Oct. 2002, doi: 10.1021/ja026764r.

[156] V. Schwartz, D. R. Mullins, W. Yan, B. Chen, S. Dai, and S. H. Overbury, “XAS Study of Au Supported on TiO2: Influence of Oxidation State and Particle Size on Catalytic Activity,” *J. Phys. Chem. B*, vol. 108, no. 40, pp. 15782–15790, Oct. 2004, doi: 10.1021/jp048076v.

[157] Y. Kotolevich *et al.*, “Effect of the Metal Deposition Order on Structural, Electronic and Catalytic Properties of TiO2-Supported Bimetallic Au-Ag Catalysts in 1-Octanol Selective Oxidation,” *Catalysts*, vol. 11, no. 7, Art. no. 7, Jul. 2021, doi: 10.3390/catal11070799.

[158] P. Verma, K. Yuan, Y. Kuwahara, K. Mori, and H. Yamashita, “Enhancement of plasmonic activity by Pt/Ag bimetallic nanocatalyst supported on mesoporous silica in the hydrogen production from hydrogen storage material,” *Appl. Catal. B Environ.*, vol. 223, pp. 10–15, Apr. 2018, doi: 10.1016/j.apcatb.2017.05.017.

[159] G. S. Henderson, F. M. F. de Groot, and B. J. A. Moulton, “X-ray Absorption Near-Edge Structure (XANES) Spectroscopy,” *Rev. Mineral. Geochem.*, vol. 78, no. 1, pp. 75–138, Jan. 2014, doi: 10.2138/rmg.2014.78.3.

[160] K.-S. Lin, Y.-J. Mai, S.-W. Chiu, J.-H. Yang, and S. L. I. Chan, “Synthesis and Characterization of Metal Hydride/Carbon Aerogel Composites for Hydrogen Storage,” *J. Nanomater.*, vol. 2012, no. 1, p. 201584, 2012, doi: 10.1155/2012/201584.

[161] A. Bzowski and T. K. Sham, “Electronic structure of Au–Ti intermetallics,” *J. Vac. Sci. Technol. A*, vol. 11, no. 4, pp. 2153–2157, Jul. 1993, doi: 10.1116/1.578384.

[162] O. Durmeyer, E. Beaurepaire, J.-P. Kappler, C. Brouder, and F. Baudelet, “Temperature dependence of the pre-edge structure in the Ti K-edge x-ray absorption spectrum of rutile,” *J. Phys. Condens. Matter*, vol. 22, no. 12, p. 125504, Mar. 2010, doi: 10.1088/0953-8984/22/12/125504.

[163] Y. Joly, D. Cabaret, H. Renevier, and C. R. Natoli, “Electron Population Analysis by Full-Potential X-Ray Absorption Simulations,” *Phys. Rev. Lett.*, vol. 82, no. 11, pp. 2398–2401, Mar. 1999, doi: 10.1103/PhysRevLett.82.2398.

[164] A. Smerigan *et al.*, “Advanced EXAFS analysis techniques applied to the L-edges of the lanthanide oxides,” *J. Appl. Crystallogr.*, vol. 57, no. 6, Art. no. 6, Dec. 2024, doi: 10.1107/S1600576724010240.

[165] M. Yu and D. R. Trinkle, “Au/TiO_2 (110) Interfacial Reconstruction Stability from ab Initio,” *J. Phys. Chem. C*, vol. 115, no. 36, pp. 17799–17805, Sep. 2011, doi: 10.1021/jp2017133.

[166] Z. Yang, R. Wu, and D. W. Goodman, “Structural and electronic properties of Au on TiO 2 (110),” *Phys. Rev. B*, vol. 61, no. 20, pp. 14066–14071, May 2000, doi: 10.1103/PhysRevB.61.14066.

[167] A. Locatelli *et al.*, “One-dimensional Au on TiO_2,” *J. Phys. Condens. Matter*, vol. 19, no. 8, p. 082202, Feb. 2007, doi: 10.1088/0953-8984/19/8/082202.

[168] M. Wang, L. Arnadottir, Z. Xu, and Z. Feng, “In Situ X-ray Absorption Spectroscopy Studies of Nanoscale Electrocatalysts,” *Nano-Micro Lett.*, vol. 11, Dec. 2019, doi: 10.1007/s40820-019-0277-x.

[169] J. Timoshenko and B. R. Cuenya, “In Situ/Operando Electrocatalyst Characterization by X-ray Absorption Spectroscopy,” *Chem. Rev.*, Sep. 2020, doi: 10.1021/acs.chemrev.0c00396.

[170] S. Calvin, *XAFS for Everyone*. Boca Raton: CRC Press, 2013. doi: 10.1201/b14843.